

DEVELOPMENT AND CHARACTERIZATION OF NEXT GENERATION BATTERIES

BY

MINJEONG SHIN

DISSERTATION

Submitted in partial fulfillment of the requirements
for the degree of Doctor of Philosophy in Chemistry
in the Graduate College of the
University of Illinois at Urbana-Champaign, 2019

Urbana, Illinois

Doctoral Committee:

Professor Andrew A. Gewirth, Chair
Professor Ralph G. Nuzzo
Professor Paul J. A. Kenis
Associate Professor Joaquín Rodríguez-López

ABSTRACT

Advances in electrochemical energy storage technology have the potential to revolutionize every aspect of society from transportation to the power grid. Despite significant advancements in Li-ion batteries over the last few decades, the current Li-ion battery has almost reached its limit in terms of energy density. Even when fully developed, the highest energy density the Li-ion battery can deliver is not enough to meet the market demand for the transportation sector. Thus, exploring new battery chemistries beyond Li-ion is crucial to electrify transportation and enable grid electricity storage.

The work in this dissertation describes approaches to develop and improve next generation battery systems by establishing structure-property relationships that govern battery performance. Chapter 1 provides the foundation to understand operating principles and related challenges of the rechargeable battery systems. Chapters 2 and 3 describe the redox chemistry of Li-S battery and strategies to mitigate the dissolution of sulfur species during electrochemical reaction. Chapter 4 describes the degradation mechanism of Ni-rich lithium nickel cobalt manganese oxide cathode materials for advanced Li-ion battery.

In Chapter 2, the use of highly concentrated solvate electrolyte and the effect of adding hydrofluoroether (HFE) cosolvent on the cycling performance of Li-S battery is discussed. In order to evaluate interactions that might change Li-S battery properties, four different HFEs with varying degrees of fluorination were examined as cosolvents in the $(\text{MeCN})_2\text{-LiTFSI}$ solvate electrolyte. The use of different HFEs enables fine tuning of Li^+ -solvent interactions which affect the cycling stability of the Li-S cell. Indeed, the cyclability of the Li-S cell varies depending on the HFE cosolvent, where the addition of highly fluorinated HFEs exhibits better

capacity retention relative to the cells with less fluorinated HFE cosolvents. The origin of this HFE effect is evaluated using various surface and bulk analytical techniques coupled with computational methods. Results show that the lower polysulfide solubility in certain solvate:HFE solutions results in stable cycling and higher capacity as limited crossover of polysulfides generates cleaner Li anodes. Using sparingly solvating electrolyte is efficient in decreasing polysulfide diffusion, however, the Li-S battery chemistry is still dictated by the very low but non-negligible polysulfide solubility in solvate electrolytes.

Another promising approach to afford Li-S battery chemistry without producing polysulfide intermediates is to utilize inorganic solid electrolytes (SE). The performance of all-solid-state Li-S battery using SE, however, is much worse than Li-S cells with liquid electrolytes in terms of active material utilization and rate capability. The major issue hindering the development of all-solid-state Li-S battery is the poor interfacial properties at the solid electrolyte/electrode interfaces.

In Chapter 3, the strategy of modifying the interface to develop high performance solid-state Li-S battery is discussed. The highly concentrated solvate solution was employed as an interlayer material at the solid electrolyte/electrode interfaces, in order to form a favorable ionic contact while maintaining the nonsolvating property of the solid electrolyte. The incorporation of the interlayer enhances the cyclability of the solid-state Li_2S cell compared to the bare counterpart. Electrochemical impedance spectroscopy of the interlayer-modified cell shows a gradual decrease in interfacial resistance as a function of cycle number, whereas the cell impedance of the bare cell remains constant. Another method to utilize the solvate electrolyte is to premix the solvate with SE to yield a solvate-solid electrolyte mixture (solvSEM) electrolyte. The hybrid Li_2S battery using solvSEM electrolyte further improves the battery performance in

terms of active material utilization, capacity retention, and active material loading. The solvSEM electrolyte combines the benefits of solid electrolyte and liquid electrolyte in that solid electrolyte acts as a blocking layer for polysulfide diffusion while solvate electrolyte forms the favorable ionic contact at battery interfaces.

In Chapter 4, the effect of water treatment on the structure of lithium nickel cobalt manganese oxide (NCM) cathode materials is investigated. Three different compositions of varying Ni, Co, and Mn content were evaluated systematically. Following water treatment, the recovered NCM materials and supernatant solutions were analyzed using various spectroscopic techniques. After water exposure, the surface impurities such as Li_2CO_3 and LiOH dissolve and leach out into solution where the concentration of dissolved Li^+ species is higher in Ni-rich NCMs. This result suggests that the thickness of the Li-rich surface layer is greater in high Ni-NCMs relative to the low Ni-NCMs and thus more susceptible to dissolution. Extensive exposure of NCM to water leads to chemical delithiation resulting in electronic and structural changes including Ni oxidation and an increase in the amount of near-surface lattice O^{2-} in high Ni content NCMs.

ACKNOWLEDGEMENTS

I would like to firstly thank my advisor Professor Andrew Gewirth for his support and guidance over the last five years. Andy has given me great scientific insights and helpful suggestions on my research projects. Thank you Andy for being an amazing mentor, guiding me to become a better scientist, and for creating a positive group environment that I greatly appreciated. Having an opportunity to work with Andy has made my graduate school experience invaluable. I feel very lucky to be part of the Gewirth group and I will always be grateful to you. I would like to thank the members of my thesis committee, Professor Ralph Nuzzo, Professor Paul Kenis, and Professor Joaquín Rodríguez-López. They have offered me valuable feedbacks and suggestions for my research. I would also like to thank my undergraduate research advisor Professor Hangil Lee at Sookmyung Women's University. He gave me opportunities to gain research experience as an undergraduate student and inspired me to pursue chemistry research in graduate school. I wouldn't be who I am today without his support and encouragement. I am truly grateful.

I would also like to thank all past and present Gewirth group members who have been great friends and co-workers throughout my time in graduate school. Special thanks to Heng-Liang Wu and Kim See who were my mentor and close collaborators in the early stages of graduate school. They brought me into the battery land and provided hands-on mentoring on battery experiments. Their encouragement helped me to move forward and become a better chemist. You are my scientific inspiration and will be. I also want to thank Lingzi Sang for teaching me how to make a solid-state battery pellet and helping me to figure out difficulties I faced along the way. The knowledge and experience you passed onto me are greatly appreciated.

and your positive attitude towards life always made me feel relaxed. I would like to thank senior Gewirth members who shared highs and lows of graduate school with me: Ryan Rooney, Kimberly Bassett, Kim Ta, Jason Varnell, Yeyoung Ha, and Yao-Min Lau. Thank you all for being supportive and being great friends. I feel very lucky to have met great colleagues who made my life in graduate school enjoyable including Danielle Henckel, Yeong-Hui Seo, Angie DiAscro, Ruixian Zhang, Stephanie Chen, Ken Madsen, Eric Thornburg, Annie Esposito, Chris Bandas, Maria Philip, Chengsi Pan, Teng Zhang, Thao Hoang, Bruno Nicolau, Kevin Schmitt, Jen Esbenshade, Chris Barile, Elizabeth Barile, Justin Oberst, and Adele Pacquette. The Gewirth group is truly enthusiastic, intelligent, and amazing group of people that I enjoyed working together with.

I would like to acknowledge several collaborators who have contributed to the work. I want to thank UIUC NMR spectroscopist Dr. Lingyang Zhu and Dr. Andre Sutrisno, who taught me and helped me a great deal on running NMR experiments. They were very knowledgeable and always willing to help setting aside a significant amount of time to work with me, which I very appreciate. I also worked closely with Dr. Rick Haasch who helped me to measure a number of XPS spectra and provided in-depth explanations. I was fortunate to have the change to collaborate with Dr. Badri Narayanan, Dr. Rajeev Assary, and Dr. Larry Curtiss at Argonne National Laboratory who performed AIMD and quantum chemical calculations of the solvate electrolyte structure. They have been great collaborators and it was a pleasure working with them. I also would like to thank Dr. Sanghyeon Kim for his help and suggestions on solid-state battery project. I am grateful for all the time and effort they spent on my research projects.

I am thankful to my closest group of friends. Special thanks to Eunkyung, Yoomin, and Woosuk for all the support, love, and encouragement they have given me over the years. All the

moments we shared have enriched my life in graduate school and I feel very lucky to have met my lifetime friends here at UIUC. I would never been able to finish this without you. I would also like to thank SohJung for maintaining over 20 years of friendship with me and taking time to visit me from Korea! I also thank my furry friend Gurumi for always being there for me and making me laugh!

Finally, I would like to thank my family who has supported me in every way possible throughout my life. I thank my parents for supporting my decision to pursue career options I desire. Special thanks to my mom who managed to teach me English from young ages which provided me a solid foundation to develop English communication skills. Thanks to my dad for everything you have done for me and your dedication to our family. Thanks to my siblings YunJeong and Hyungho for their love and support. Five years of time me being far away from home must have been difficult for them either. Nonetheless, they were always there lighting at the end of the tunnel. None of this would have been possible without their love and support.

~ Dedicated to my beloved family and friends ~

TABLE OF CONTENTS

CHAPTER 1: Introduction to Electrochemical Energy Storage Systems	1
CHAPTER 2: Effect of the Hydrofluoroether Cosolvent Structure in Acetonitrile- Based Solvate Electrolytes on the Li ⁺ Solvation Structure and Li-S Battery Performance	17
CHAPTER 3: Incorporating Solvate and Solid Electrolytes for All-Solid-State Li ₂ S Batteries with High Capacity and Long Cycle Life	68
CHAPTER 4: Investigating the Effect of Water Treatment on the Structure of Li-Ion Battery Cathode Materials.....	113

CHAPTER 1

Introduction to Electrochemical Energy Storage Systems

1.1 The Need for Electrochemical Energy Storage

With the global population growth and rapid urbanization, the global energy consumption has increased significantly over the last few decades and is projected to further increase by 50% between 2010 and 2050.¹⁻² Currently, the energy production relies heavily on fossil fuels which causes severe environmental damages due to CO₂ emissions.³ The increase in electricity production should be achieved in a way that reduces our reliance on limited fossil fuel to realize sustainable future energy landscape.⁴ Alternatively, renewable energy resources such as solar and wind energy have great potential to provide electricity without increasing CO₂ emissions.

Despite such advantages, the use of renewable energy is limited due to its intermittent nature. Since renewable energy sources cannot produce electricity on demand, efficient electrochemical energy storage devices that can store energy during periods of low demand and release energy during periods of high demand are essential (**Figure 1.1**).⁵⁻⁷ Rechargeable batteries are one of the common energy storage technologies, typically used for small and medium scale storage purposes.⁸ However, the state-of-the art Li-ion battery technology may not be a feasible option for future energy solution due to its limited charge storage capacity and high manufacturing cost. For the large-scale energy storage from renewable sources to be practical, a new battery technology that can store large amounts of energy at low cost should be essential.

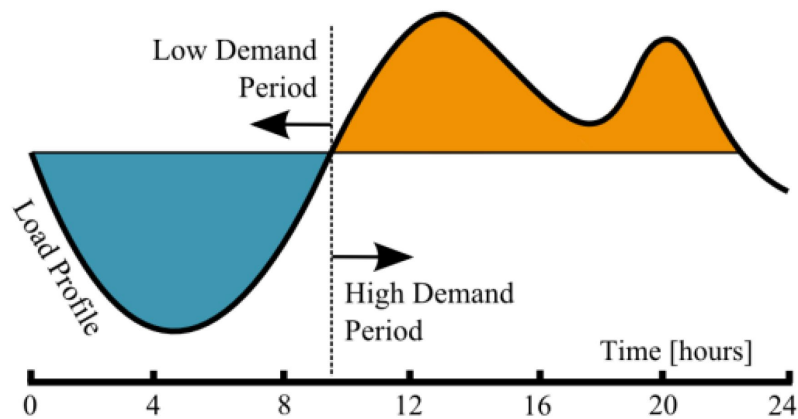


Figure 1.1 Electrochemical energy storage devices can store energy from renewable sources when supply exceeds demand and this can be later used when additional energy is necessary. Reprinted from ref (7). Published 2015 MDPI under license CC BY 4.0.

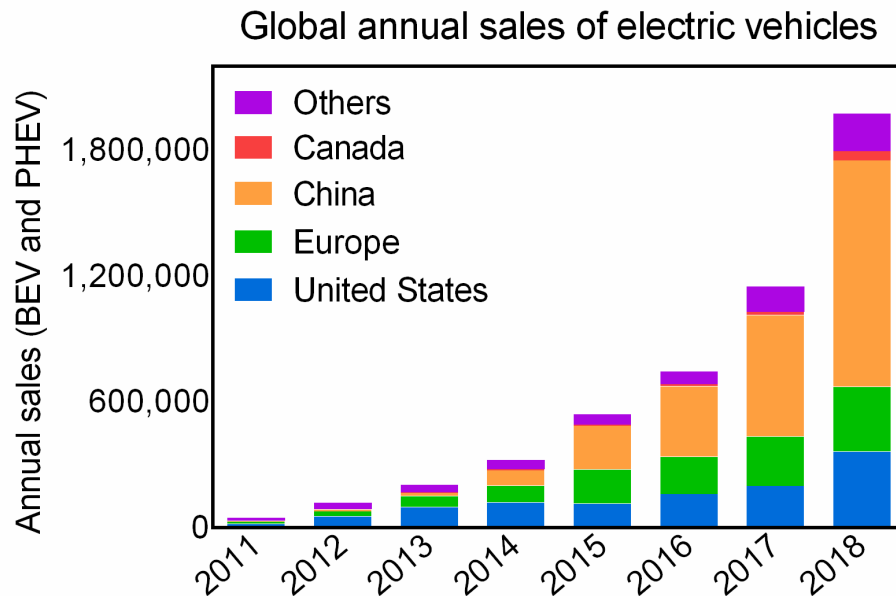


Figure 1.2 Global Annual sales of battery electric vehicle (BEV) and plug-in hybrid electric vehicle (PHEV) between 2011 and 2018. Data compiled from “Global EV Outlook 2019” – International Energy Agency.

The development of efficient energy storage technology will further accelerate the shift from conventional gasoline vehicles to electric vehicles in automotive transportation. With the transportation sector accounting for 29% of the total U.S. greenhouse gas emission in 2017, the electrification of the transport system has great potential toward green energy future.⁹ As shown in **Figure 1.2**, the annual sales of battery electric vehicle and plug-in hybrid electric vehicle have increased substantially over the last few years, and these numbers are expected to further increase as battery technology advances. Despite significant advancements in Li-ion batteries over the last few decades, the current Li-ion battery has almost reached its limit in terms of energy density.¹⁰ Even when fully developed, the highest energy density the Li-ion battery can deliver is not enough to meet the market demand for the transportation sector.¹⁰ Thus, exploring new battery chemistries beyond Li-ion is crucial to electrify transportation and enable grid electricity storage. Next generation battery systems such as Li-S or Li-O₂ are viable options as they offer significantly higher specific energy density compared to Li-ion.¹⁰

1.2 The Basics of Rechargeable Battery

Battery is a device that converts chemical energy into electrical energy by means of electrochemical reaction. The battery consists of three major components including the anode, the cathode, and the electrolyte. The electrode with a more negative reduction potential is called the negative electrode or anode, while the electrode with a more positive reduction potential is called the positive electrode or cathode. Due to the potential difference between two electrodes, electrochemical reactions are thermodynamically favorable and occur spontaneously when the cell is connected to an external load. The anode is the electrode at which oxidation reaction occurs during cell discharge and the cathode is the electrode where reduction happens

during discharge. Upon charging, the opposite electrochemical reaction happens at each electrode (i.e. reduction at the anode, and oxidation at the cathode). The two electrodes are separated by the electrolyte which allows ions to diffuse through but not electrons, therefore ensuring the flow of electrons through the external circuit connecting two electrodes.

When developing new battery chemistries, the two important metrics should be considered: cell voltage and capacity. From the perspective of battery performance, the cell voltage and capacity (either gravimetric or volumetric) should be maximized to achieve high theoretical energy density. The theoretical cell voltage and capacity are a function of the anode and cathode active material.

The theoretical cell voltage is determined by the difference between the standard electrode potential of the cathode and anode. The actual open circuit voltage deviates from the theoretical cell voltage considering other factors including temperature and active species concentration, given by the Nernst equation.¹¹⁻¹² The operating voltage is further varied by the IR drop and cell polarization (e.g. charge-transfer overpotential and mass-transfer overpotential).

The theoretical capacity is the amount of charge stored per unit mass or per unit volume. Capacity is typically expressed in units of mAh g⁻¹ for gravimetric capacity, and mAh L⁻¹ for volumetric capacity. The theoretical gravimetric capacity ($Q_{\text{theoretical}}$) of the material can be calculated if the involved electrochemical reaction and its stoichiometry is known, as shown below where Mw is the molecular weight and n is the number of electrons transferred.¹¹

$$Q_{\text{theoretical}} = \frac{26802 \text{ (mAh/mol)}}{Mw \text{ (g/mol)}} \times n$$

The actual capacity the cell delivers, however, usually deviates from the theoretical values due to a number of factors including incomplete active material utilization and

polarization in every process.¹³ The capacity is determined experimentally by performing galvanostatic cycling experiment (also called as chronopotentiometry) for each charge and discharge processes. During galvanostatic charge-discharge measurements, constant current is applied and resulting potential response is recorded. For half-cells, the applied current is determined by the mass of active material and the desired C-rate. The current loading of 1 C is defined as the current necessary to fully charge or discharge the material in one hour. The cyclability of battery is evaluated by repeating the charge/discharge cycle, in which case the plot of capacity (or capacity retention) vs. cycle number reports on the lifespan of rechargeable batteries. The Coulombic efficiency (CE) is another important metrics used to evaluate the reversibility of the system. For cathode materials, CE is the ratio of discharge capacity to charge capacity.¹³

1.3 Lithium-Ion (Li-ion) Battery

Since its first commercialization in 1991 by Sony, Li-ion battery has become an essential part of our daily life powering a variety of devices from personal electronics to electric vehicles. Li-ion battery outperforms other common secondary batteries such as lead-acid, nickel-cadmium, and nickel metal hydride in terms of voltage and energy density.⁸ In addition, Li-ion batteries offer long cycle life, low self-discharge rate, and broad range of operating temperature, making them attractive for many applications. The Nobel Prize of Chemistry in 2019 was awarded to John Goodenough, Stanley Whittingham, and Akira Yoshino for the development of the Li-ion battery.

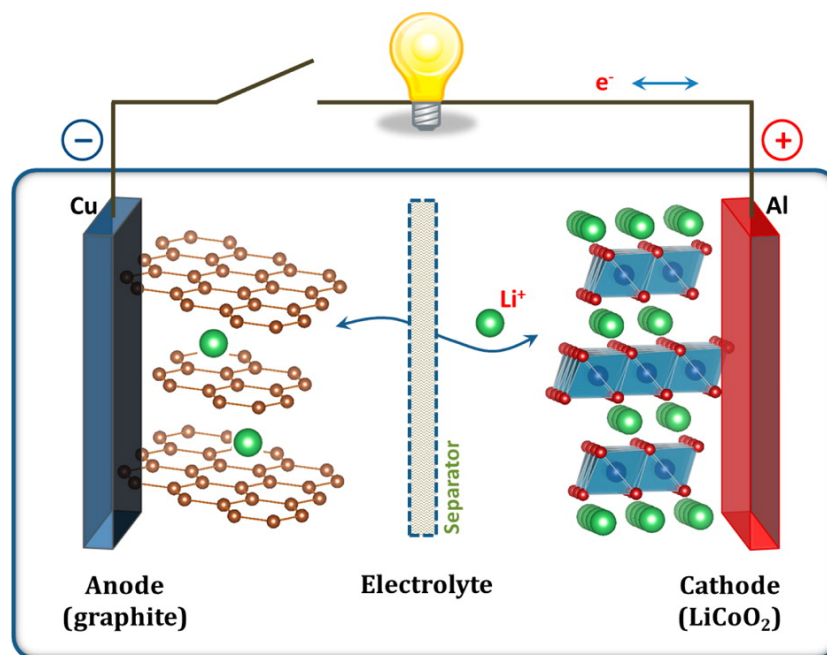
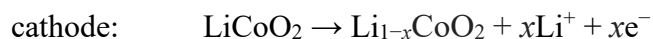
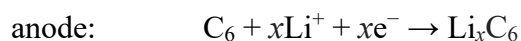


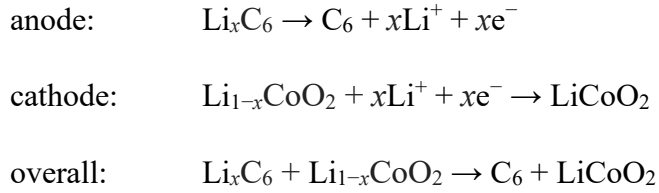
Figure 1.3 Schematic illustration of the Li-ion battery using graphite anode and LiCoO₂ cathode. Reprinted with permission from ref (14). Copyright 2013 American Chemical Society.

The current Li-ion technology is based on the intercalation anode and cathode materials. Li-ion battery operates by reversibly intercalating Li⁺ ions between graphite anode (Li_xC₆) and transition metal oxide cathode (Li_{1-x}T^MO₂, where T^M is usually cobalt, manganese, iron, and nickel).⁸ **Figure 1.3** shows the schematic of the Li-ion battery using graphite anode and LiCoO₂ cathode. The electrochemical reactions that occur at each electrode during charge and discharge are shown below:

Charge mechanism:



Discharge mechanism:



During the charge process, the removal of Li^+ from the cathode is accompanied by the oxidation of host lattice to maintain the charge neutrality. The removed Li^+ ions are intercalated into the graphite anode. The opposite reaction occurs during discharge, where cathode is lithiated and anode is delithiated. LiCoO_2 has been the most commonly used cathode material after the commercialization of Li-ion battery, due to its high reversibility and stable cycling characteristics.¹⁵⁻¹⁶ However, the high cost and low natural abundance of Co motivated the search for alternative cathode materials such as lithium iron phosphate (LFP), lithium manganese oxide (LMO), and lithium nickel cobalt manganese oxide (NCM). The characteristics of common cathode materials used in Li-ion battery is summarized in **Table 1.1**.

Table 1.1 Characteristics of representative intercalation cathode used in commercialized Li-ion battery. Values are taken from ref (17).

Crystal structure	Compound	Acronym	Gravimetric capacity (mAh g^{-1}) theoretical / experimental	Average voltage (V)
Layered	LiCoO_2	LCO	274 / 148	3.8
Layered	$\text{LiNi}_{0.33}\text{Co}_{0.33}\text{Mn}_{0.33}\text{O}_2$	NCM111	280 / 160	3.7
Layered	$\text{LiNi}_{0.8}\text{Co}_{0.15}\text{Al}_{0.05}\text{O}_2$	NCA	279 / 199	3.7
Spinel	LiMn_2O_4	LMO	148 / 120	4.1
Olivine	LiFePO_4	LFP	170 / 165	3.4

1.4 Lithium-Sulfur (Li-S) Battery

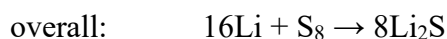
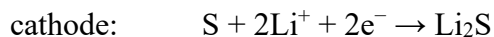
1.4.1 Basic Principles of Li-S Battery

The Li-S battery is receiving increasing attention as a promising next-generation battery technology due to the high theoretical capacity of S_8 (1672 mAh g^{-1}), which is more than five times greater than that of the intercalation-based Li-ion cathode materials.¹⁸ This capacity difference originates from fundamentally different reaction mechanism of the two systems. The Li-ion battery operates on intercalation-based chemistry where reaction only occurs at the transition metal sites and other atoms remain redox inactive. In contrast, the Li-S battery chemistry is conversion-based and thus all active material components are redox active contributing to the capacity. The high abundance and non-toxicity of sulfur provides additional benefits from the sustainability point of view.¹⁹

A typical Li-S cell consists of Li metal as the anode, sulfur as the cathode, and nonaqueous electrolyte in between. Upon discharging, S reacts with Li and is reduced by a two-electron process to form a final discharge product of Li_2S . In typical nonaqueous organic electrolytes, the electroreduction from S to Li_2S is not a direct solid-solid conversion. Instead the reaction is a solution mediated process where a series of lithium polysulfide intermediates (Li_2S_n , $n = 2-8$) are formed. As shown in **Figure 1.4a**, the multi-step reduction mechanism of Li-S cell is manifested in the voltage profile in which multiple plateaus are observed. The exact shape of the voltage profile could vary depending on the composition of electrolyte or the reaction temperature.²⁰⁻²¹ At early stages of discharge, sulfur is reduced to form high-order polysulfides (Li_2S_n , $n \geq 4$) and further battery discharging results in the formation of low-order polysulfides (Li_2S_n , $1 < n < 4$), and finally Li_2S .²²⁻²⁴ Upon charging, the opposite reaction happens at each electrode, oxidizing Li_2S to polysulfides and then back to S_8 . The nominal voltage of typical

Li-S cell (of 2.1 V vs. Li/Li⁺) is lower than that of the Li-ion, but this is offset by high specific capacity yielding a theoretical specific energy of 2567 Wh kg⁻¹.¹⁰

Discharge mechanism:



Charge mechanism:

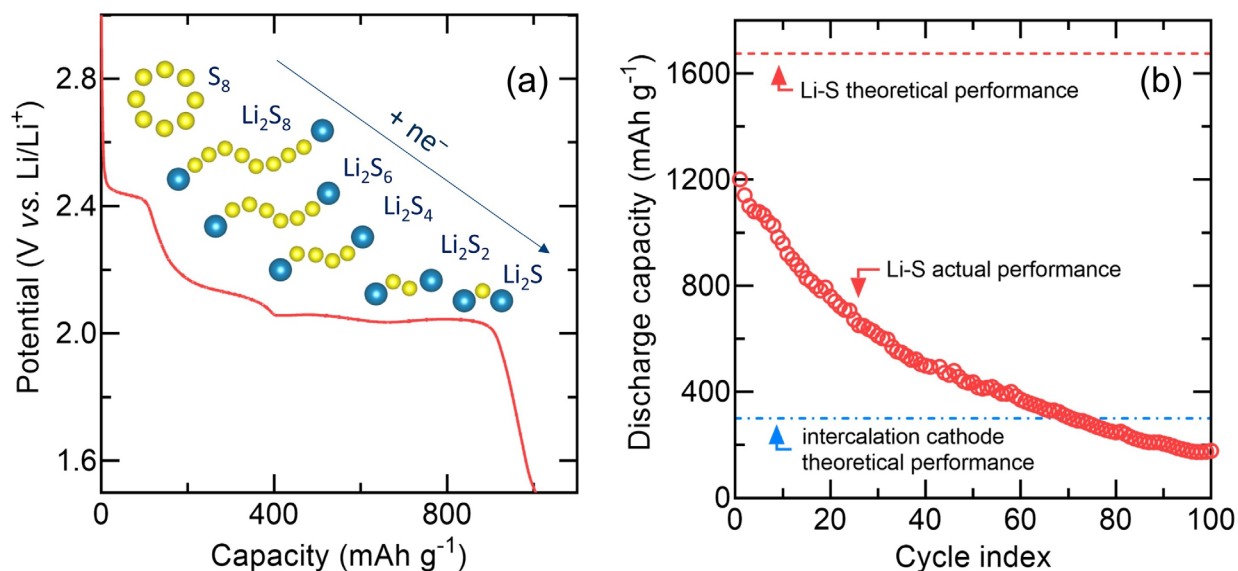
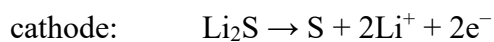


Figure 1.4 Galvanostatic cycling of a Li-S cell using Li metal anode, S/C cathode, and 1 M LiTFSI in 1,3-dioxolane (DOL) / 1,2-dimethoxyethane (DME). The cathode composition is 60 wt% S₈, 30 wt% conductive carbon, and 10 wt% of poly(vinylidene fluoride) (PVDF) binder. The cell was cycled between 1.5 and 3.2 V vs. Li/Li⁺ at C/10. (a) shows the typical voltage curve of the Li-S cell during discharge and (b) shows the long-term cycling stability of the cell.

1.4.2 Challenges in Li-S Battery

Despite many advantages of Li-S, only limited success in commercialization was achieved after few decades of research and development. As of 2019, the Li-S prototype cell developed by OXIS Energy delivers the specific energy of 400 Wh kg^{-1} , which is smaller by a factor of 6 compared to the theoretical value. In practice, the performance of the Li-S cell exhibits low capacity and poor cycling for a number of reasons (**Figure 1.4b**).

First, the insulating nature of S_8 and its discharge product Li_2S impedes the reaction kinetics, increasing the cell resistance/polarization and decreasing the active material utilization. To mitigate this issue, large amounts of high surface area carbon additives (ca. 30 wt%) are added into the electrode to provide necessary conductivity for electrochemical reaction, which inevitably decreases the energy density of the battery. Even with the incorporation of large amounts of conductive carbon, however, the discharge capacity obtained at cycle 1 is only 1200 mAh g^{-1} , corresponding to 72% of active material utilization (**Figure 1.4b**).

The second problem is associated with the large volume change the sulfur cathode experiences during battery operation. When sulfur is converted to Li_2S , the volume expands by 80% due to their large density difference.²⁰ The repeated volume expansion and contraction during cycling results in a crack formation and material pulverization leading to the physical contact loss.²⁵⁻²⁶ When the cathode active material is not in contact with the current collector or the surrounding conducting matrix, the material remains electrochemically inactive. The fraction of the inactive sulfur species likely increases with cycling resulting in a gradual capacity fade, as shown in **Figure 1.4b**. Various approaches such as polyethylene glycol (PEG)/graphene composite coating²⁷ and yolk-shell nanostructure with internal void²⁸⁻²⁹ were employed to

accommodate the volume expansion of sulfur during lithiation. However, these methods require complicated cathode engineering which limits their practical use in commercial batteries.

Another critical challenge in Li–S battery originates from the soluble nature of the sulfur intermediate species. The generated polysulfides readily dissolve and diffuse into most of the organic electrolytes. The formation of polysulfide intermediates is beneficial to some extent in that the reaction kinetics are more facile when the conversion from sulfur to Li_2S is a solution-mediated process instead of a solid-state conversion.³⁰⁻³³ However, the dissolution of lithium polysulfides in the electrolyte poses a number of negative impacts on battery performance. The direct consequence of the polysulfide dissolution is the loss of active material from the cathode leading to the irreversible capacity fade.³⁴⁻³⁵ The dissolved species can migrate to the Li anode giving rise to a well-known shuttle mechanism and passivating Li surface by forming insoluble layer of Li_2S and Li_2S_2 . The shuttle effect occurs during charge when high-order polysulfides generated from the cathode diffuse to the anode, where they are reduced to low-order polysulfides.³⁶ These low-order polysulfides then migrate back to cathode and become re-oxidized to high-order polysulfides. This parasitic cycle is repeated continuously during charge, causing a prolonged charge cycle and low Coulombic efficiency.³⁶

The issues resulting from the polysulfide dissolution is the primary degradation mechanism in Li–S battery. The formation kinetics of polysulfides and their concentration vary substantially depending on the solvating ability of the electrolyte. Therefore, a proper choice of electrolyte components such as Li salt, solvent, and electrolyte additive and their composition may enable high-performance Li–S battery.³⁷⁻³⁸ Ether solvents such as 1,3-dioxolane (DOL), 1,2-dimethoxyethane (DME), tetraethylene glycol dimethyl ether (TEGDME) along with lithium bis(trifluoromethanesulfonyl)imide (LiTFSI) salt combination have been extensively studied for

Li-S battery due to their chemical compatibility with polysulfides.^{33, 38} In a 1 M LiTFSI in TEGDME electrolyte, however, the solubility of Li_2S_8 (total atomic S concentration) can reach up to 6 M, exhibiting severe polysulfide shuttle and low Coulombic efficiency.³⁹

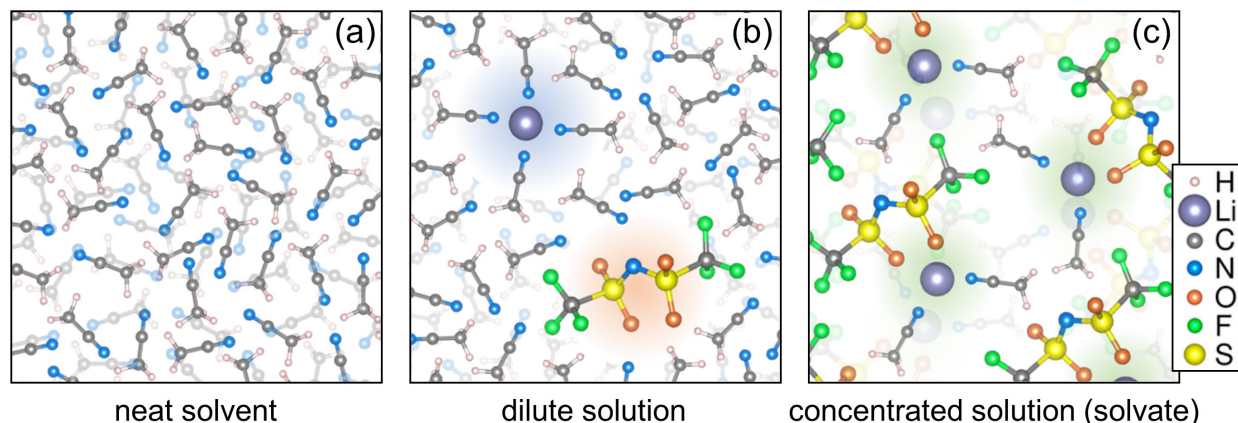


Figure 1.5 Schematics of solution structures with varying LiTFSI salt concentration in acetonitrile (MeCN) solvent: (a) neat solvent, (b) dilute solution with low salt concentration (e.g. 1 M LiTFSI in MeCN), and (c) concentrated solvate solution (e.g. 4 M LiTFSI in MeCN). As the Li salt concentration increases to form the solvate, the solvation favors the formation of contact ion pairs or aggregates instead of forming solvent-separated ion pairs.

A promising approach to address the issues related to polysulfides is to use the highly concentrated solvate electrolyte.^{32, 40-43} In a dilute electrolyte solution (e.g. 1 M Li salt in solvent), Li^+ is primarily coordinated by solvent molecules and the solution structure is dominated by solvent-separated ion pairs (see **Figure 1.5b**).⁴⁴⁻⁴⁵ In this solution, there are a lot of free/uncoordinated solvent molecules that can solvate other species in the battery. As shown in **Figure 1.5c**, once the Li salt concentration is increased to a level where all solvent molecules are coordinated to the Li^+ center to form the “solvate”, only minimal amount of free solvent is present to solubilize additional species. Due to the unique solution structure, the solvate electrolytes are sparingly solvating with respect to dissolving polysulfide intermediates.^{40, 42, 46-47} Another electrolyte class that inhibit polysulfide dissolution is inorganic solid electrolytes.⁴⁸ By

shifting from electrolyte that fully solvates polysulfides to sparingly solvating or nonsolvating electrolytes, the detrimental effect of polysulfides can be effectively eliminated. Chapters 2 and 3 demonstrate two different approaches to redirect the Li–S battery chemistry by using sparingly solvating and nonsolvating electrolyte (**Figure 1.6**).

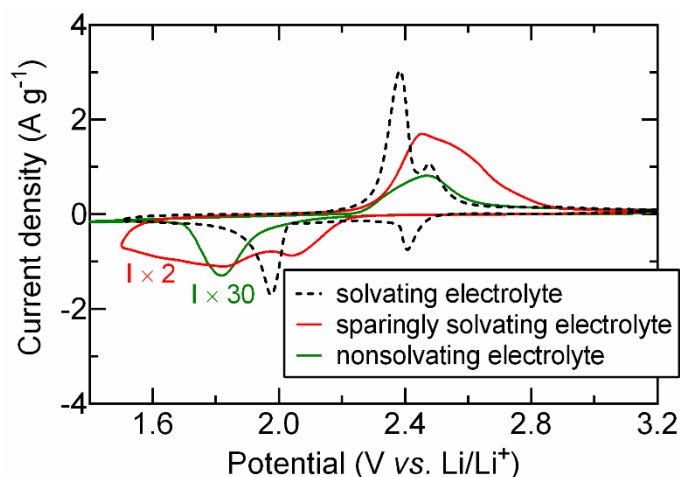


Figure 1.6 Cyclic voltammetry of Li–S cells with Li metal anode, S₈/C cathode, and the indicated electrolyte cycled at 0.1 mV s^{−1}. Solvating electrolyte is the conventional electrolyte, 1 M LiTFSI in DOL/TEGDME. Sparingly solvating electrolyte is the highly concentrated solvate electrolyte, (MeCN)₂–LiTFSI diluted with TTE. Nonsolvating electrolyte is the inorganic solid electrolyte, Li₇P₃S₁₁.

1.5 References

- (1) Lewis, N. S. *MRS Bull.* **2011**, 32, 808-820.
- (2) Larcher, D.; Tarascon, J. M. *Nat. Chem.* **2014**, 7, 19-29.
- (3) Davis, S. J.; Caldeira, K.; Matthews, H. D. *Science* **2010**, 329, 1330-1333.
- (4) Dincer, I. *Renewable Sustainable Energy Rev.* **2000**, 4, 157-175.
- (5) Hall, P. J.; Bain, E. J. *Energy Policy* **2008**, 36, 4352-4355.
- (6) Beaudin, M.; Zareipour, H.; Schellenberglobe, A.; Rosehart, W. *Energy Sustainable Dev.* **2010**, 14, 302-314.

- (7) Sabihuddin, S.; Kiprakis, A.; Mueller, M. *Energies* **2014**, *8*, 172-216.
- (8) Armand, M.; Tarascon, J. M. *Nature* **2008**, *451*, 652-657.
- (9) Inventory of U.S. Greenhouse Gas Emissions and Sinks: 1990 - 2017. United States Environmental Protection Agency.
- (10) Bruce, P. G.; Freunberger, S. A.; Hardwick, L. J.; Tarascon, J.-M. *Nat. Mater.* **2011**, *11*, 19-29.
- (11) Reddy, T., *Linden's Handbook of Batteries, 4th Edition*. McGraw-Hill Education: 2010.
- (12) Aifantis, K. E.; Hackney, S. A.; Kumar, R. V., *High energy density lithium batteries*. Wiley Online Library: 2010.
- (13) Yang, X.; Rogach, A. L. *Adv. Energy Mater.* **2019**, *9*, 1900747.
- (14) Goodenough, J. B.; Park, K.-S. *J. Am. Chem. Soc.* **2013**, *135*, 1167-1176.
- (15) Cho, J.; Kim, Y. J.; Kim, T.-J.; Park, B. *Angew. Chem., Int. Ed.* **2001**, *40*, 3367-3369.
- (16) Etacheri, V.; Marom, R.; Elazari, R.; Salitra, G.; Aurbach, D. *Energy Environ. Sci.* **2011**, *4*, 3243.
- (17) Nitta, N.; Wu, F.; Lee, J. T.; Yushin, G. *Mater. Today* **2015**, *18*, 252-264.
- (18) Tarascon, J. M.; Armand, M. *Nature* **2001**, *414*, 359-367.
- (19) Yin, Y.-X.; Xin, S.; Guo, Y.-G.; Wan, L.-J. *Angew. Chem., Int. Ed.* **2013**, *52*, 13186-13200.
- (20) Xu, R.; Lu, J.; Amine, K. *Adv. Energy Mater.* **2015**, *5*, 1500408.
- (21) Akridge, J. *Solid State Ionics* **2004**, *175*, 243-245.
- (22) Yamin, H.; Peled, E. *J. Power Sources* **1983**, *9*, 281-287.
- (23) Kumaresan, K.; Mikhaylik, Y.; White, R. E. *J. Electrochem. Soc.* **2008**, *155*, A576.

- (24) Barchasz, C.; Molton, F.; Duboc, C.; Leprêtre, J.-C.; Patoux, S.; Alloin, F. *Anal. Chem.* **2012**, *84*, 3973-3980.
- (25) Ji, X.; Evers, S.; Black, R.; Nazar, L. F. *Nat. Commun.* **2011**, *2*.
- (26) Zhang, S. S. *J. Power Sources* **2013**, *231*, 153-162.
- (27) Wang, H.; Yang, Y.; Liang, Y.; Robinson, J. T.; Li, Y.; Jackson, A.; Cui, Y.; Dai, H. *Nano Lett.* **2011**, *11*, 2644-2647.
- (28) Wei Seh, Z.; Li, W.; Cha, J. J.; Zheng, G.; Yang, Y.; McDowell, M. T.; Hsu, P.-C.; Cui, Y. *Nat. Commun.* **2013**, *4*.
- (29) Zhou, W.; Yu, Y.; Chen, H.; DiSalvo, F. J.; Abruña, H. D. *J. Am. Chem. Soc.* **2013**, *135*, 16736-16743.
- (30) Yu, X.; Manthiram, A. *Phys. Chem. Chem. Phys.* **2015**, *17*, 2127-2136.
- (31) Dibden, J. W.; Smith, J. W.; Zhou, N.; Garcia-Araez, N.; Owen, J. R. *Chem. Commun.* **2016**, *52*, 12885-12888.
- (32) Cuisinier, M.; Cabelguen, P. E.; Adams, B. D.; Garsuch, A.; Balasubramanian, M.; Nazar, L. F. *Energy Environ. Sci.* **2014**, *7*, 2697-2705.
- (33) Pang, Q.; Liang, X.; Kwok, C. Y.; Nazar, L. F. *Nat. Energy* **2016**, *1*.
- (34) Manthiram, A.; Fu, Y.; Chung, S.-H.; Zu, C.; Su, Y.-S. *Chem. Rev.* **2014**, *114*, 11751-11787.
- (35) Ryu, H. S.; Guo, Z.; Ahn, H. J.; Cho, G. B.; Liu, H. *J. Power Sources* **2009**, *189*, 1179-1183.
- (36) Mikhaylik, Y. V.; Akridge, J. R. *J. Electrochem. Soc.* **2004**, *151*, A1969.
- (37) Scheers, J.; Fantini, S.; Johansson, P. *J. Power Sources* **2014**, *255*, 204-218.

- (38) Wang, L.; Ye, Y.; Chen, N.; Huang, Y.; Li, L.; Wu, F.; Chen, R. *Adv. Funct. Mater.* **2018**, 28, 1800919.
- (39) Park, J.-W.; Yamauchi, K.; Takashima, E.; Tachikawa, N.; Ueno, K.; Dokko, K.; Watanabe, M. *J. Phys. Chem. C* **2013**, 117, 4431-4440.
- (40) Yamada, Y.; Wang, J.; Ko, S.; Watanabe, E.; Yamada, A. *Nat. Energy* **2019**.
- (41) Cheng, L.; Curtiss, L. A.; Zavadil, K. R.; Gewirth, A. A.; Shao, Y.; Gallagher, K. G. *ACS Energy Lett.* **2016**, 1, 503-509.
- (42) Yamada, Y.; Yamada, A. *J. Electrochem. Soc.* **2015**, 162, A2406-A2423.
- (43) Dokko, K.; Tachikawa, N.; Yamauchi, K.; Tsuchiya, M.; Yamazaki, A.; Takashima, E.; Park, J.-W.; Ueno, K.; Seki, S.; Serizawa, N.; Watanabe, M. *J. Electrochem. Soc.* **2013**, 160, A1304-A1310.
- (44) Seo, D. M.; Borodin, O.; Han, S.-D.; Boyle, P. D.; Henderson, W. A. *J. Electrochem. Soc.* **2012**, 159, A1489-A1500.
- (45) See, K. A.; Wu, H.-L.; Lau, K. C.; Shin, M.; Cheng, L.; Balasubramanian, M.; Gallagher, K. G.; Curtiss, L. A.; Gewirth, A. A. *ACS Appl. Mater. Interfaces* **2016**, 8, 34360-34371.
- (46) Suo, L.; Hu, Y.-S.; Li, H.; Armand, M.; Chen, L. *Nat. Commun.* **2013**, 4.
- (47) Shin, M.; Wu, H.-L.; Narayanan, B.; See, K. A.; Assary, R. S.; Zhu, L.; Haasch, R. T.; Zhang, S.; Zhang, Z.; Curtiss, L. A.; Gewirth, A. A. *ACS Appl. Mater. Interfaces* **2017**, 9, 39357-39370.
- (48) Shin, M.; Gewirth, A. A. *Adv. Energy Mater.* **2019**, 9, 1900938.

CHAPTER 2

Effect of the Hydrofluoroether Cosolvent Structure in Acetonitrile-Based Solvate Electrolytes on the Li^+ Solvation Structure and Li-S Battery Performance

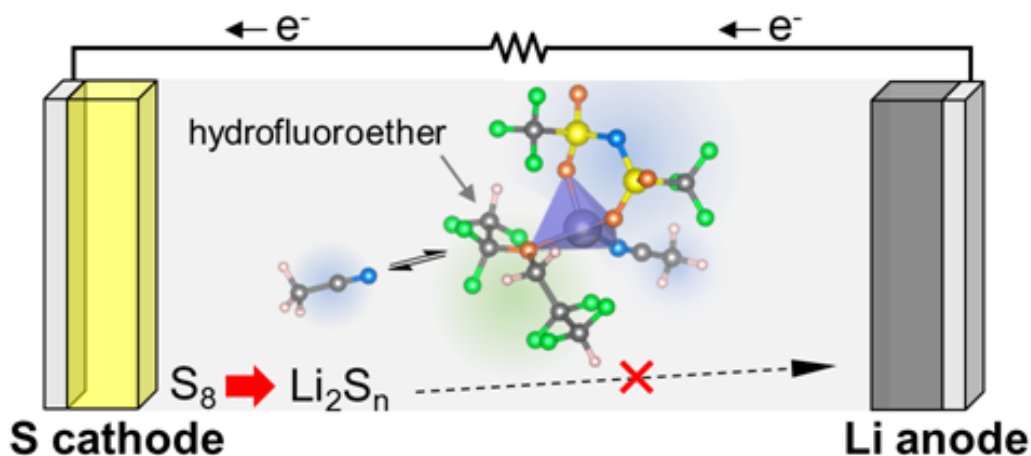


Figure 2.1 Cartoon depicting the role of hydrofluoroether cosolvent identified in this work.

2.1 Introduction

With the increasing demand for electric vehicles and portable electronics, Li-S batteries are receiving considerable attention as a promising next generation battery due to their high energy density and the low cost of sulfur.¹⁻² The S cathode delivers the theoretical capacity of 1672 mAh g^{-1} , compared to only 274 mAh g^{-1} for LiCoO_2 intercalation cathode used in Li-ion battery.³ A major problem hindering Li-S battery commercialization is the complicated reduction/oxidation pathway of the Li-S chemistry. The electrochemical conversion from S_8 to

This chapter was reproduced with permission from Shin, M.; Wu, H.-L.; Narayanan, B.; See, K. A.; Assary, R. S.; Zhu, L.; Haasch, R. T.; Zhang, S.; Zhang, Z.; Curtiss, L. A.; Gewirth, A. A., *ACS Appl. Mater. Interfaces* **2017**, 9, 39357-39370. Copyright © 2017, American Chemical Society.

Li₂S involves a phase change during which soluble lithium polysulfide intermediate species are generated.⁴⁻⁶ High-order lithium polysulfides (Li₂S_n, n ≥ 4) readily dissolve into the organic electrolyte, causing severe capacity fading and poor Coulombic efficiency.³ In addition, the migration of intermediate polysulfides to the Li metal anode causes the well-known polysulfide shuttle effect.⁷⁻⁸ Various strategies are employed to address the issue of polysulfide dissolution, including physical confinement of polysulfides within S cathode,⁹⁻¹¹ fabricating a protecting layer on Li anode,¹² electrolyte additives to modify reaction pathway and passivate Li anode,¹³⁻¹⁵ and tuning the electrolyte composition to reduce the solubility of polysulfides.¹⁶⁻¹⁷

Among the electrolyte modification approaches, the use of high Li salt concentration is effective in minimizing polysulfide dissolution, mitigating the polysulfide shuttle, and achieving stable battery cycling.¹⁸⁻²¹ The low polysulfide solubility in concentrated electrolytes can be explained by the common ion effect where the equilibrium between Li₂S_n and solvated Li⁺ is shifted to disfavor solvated Li⁺ as a result of the excess solvated Li⁺ in solution (Li₂S_n ⇌ Li⁺ + S_n²⁻).¹⁸ In addition to the common ion effect, the unique solution structure of the concentrated electrolyte may also dictate polysulfide solubility. The Li⁺ solvation structure of the concentrated solution is completely different from that of the dilute solution in which solvent-separated ion pairs dominate the salt speciation.²²⁻²³ As the Li salt concentration is increased, solvent-separated ion pairs are forced into contact ion pairs in which the Li coordination sphere is composed of both the salt anion and the solvent molecules.²²⁻²³ When the Li salt concentration is increased to a level in which all solvent molecules are coordinated to Li⁺ to form the “solvate” complex, only a small amount of free solvent is present to solubilize polysulfide species, significantly decreasing the polysulfide solubility.²⁰ This class of electrolyte is called the solvate or sparingly solvating electrolyte.

Watanabe and co-workers evaluated the polysulfide solubility and corresponding electrochemical performance of the Li-S cell in glyme-based solvate electrolytes, where higher salt concentration electrolytes exhibit longer cycle life and higher Coulombic efficiency.²⁰ Similarly, Nazar and co-workers studied solvate electrolytes for Li-S battery, based on high concentration of LiTFSI salt in acetonitrile (MeCN) to form the solvate (MeCN)₂-LiTFSI.²¹ The low polysulfide solubility is achieved by the unique solvation structure of the complex where the Li⁺ cation is chelated by solvent molecules thereby decreasing its donating ability towards polysulfides.^{20-21, 24} Despite these favorable effects, the solvate electrolytes exhibit high viscosity and low ionic conductivity compared to the conventional 1 M ethereal electrolytes.²⁰⁻²¹ Cosolvents such as hydrofluoroether (HFE) that solubilize the solvate complexes but maintain limited solubility of the lithium polysulfides have been used to lower the viscosity of the electrolytes while maintaining beneficial effects on the electrochemical behavior.²⁰⁻²¹

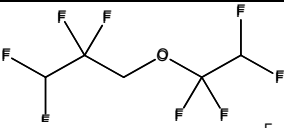
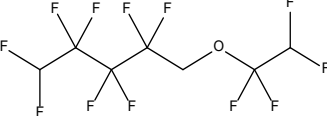
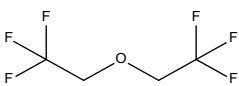
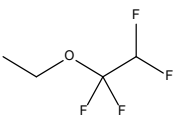
The (MeCN)₂-LiTFSI solvate electrolyte has been a special focus of recent studies, due to its intriguing solution structure and unique discharge profile compared to the curve obtained in conventional ether-based electrolytes.^{21-22, 25-27} The Li-S cell with (MeCN)₂-LiTFSI electrolyte exhibits a sloping voltage profile with two plateaus that are less clearly defined, suggesting a fundamentally different reaction mechanism.²¹ However, the Li-S cell with neat solvate experiences severe capacity fading and poor Coulombic efficiency.²¹ Stable cycling is achieved only when the HFE cosolvent, 1,1,2,2-tetrafluoroethyl 2,2,3,3-tetrafluoropropyl ether (TTE), is added to decrease the viscosity and increase ionic conductivity.²¹ Besides its role in improving the transport properties, the TTE has a significant effect on the local solvation structure of the electrolyte and the Li-S electrochemistry.²⁵ Previous work shows that adding TTE to the (MeCN)₂-LiTFSI electrolyte results in TTE coordination to Li⁺ at the expense of MeCN

coordination, releasing free or uncoordinated MeCN.²⁵ Increased free MeCN facilitates the S₈ reduction kinetics at the cathode by local solvation effects, which is likely the cause for the enhanced battery cycling behavior and high S₈ utilization efficiency.²⁵ Additionally, HFEs are known to affect the Li–S battery performance by suppressing the polysulfide shuttle effect, mitigating self-discharge, and affecting solid-electrolyte interphase (SEI) formation overall improving the cyclability and Coulombic efficiency.^{16, 28-34} Further studies by Balasubramanian and co-workers showed that a moderate rise in Li–S cell operating temperature again redirects the reaction pathway allowing for minimal overpotential and high sulfur utilization efficiency.²⁷ The fine tuning of polysulfide solubility by temperature control alters the conversion of S₈ to Li₂S to follow quasi-solid-state reaction where intermediate polysulfide species act as internal redox mediator and change the relative rate of competing reactions.²⁷

Due to the intriguing ability of the TTE to affect the local structure of Li⁺ and consequently the S₈ electrochemistry, we set out to understand the origin of these interactions and develop structure-property relationships by modifying the HFE structure. This approach has allowed us to determine if there is a specific molecular-scale interaction we can utilize to design an advanced HFE-containing electrolytes. In order to evaluate interactions that might change Li–S battery properties, herein we examine four different HFEs with varying degrees of fluorination as cosolvents in the (MeCN)₂–LiTFSI electrolyte. The use of different HFEs enables fine tuning of the Li⁺–solvent interaction that affects the cycling stability of the Li–S cell. Cycling of the Li–S battery shows that the addition of highly fluorinated HFEs yields higher discharge capacity relative to cells with less fluorinated HFE cosolvents. To understand this effect, we evaluate the physicochemical properties, solvation structure, polysulfide solubility, and SEI formation on the Li anode using Raman, NMR, ab initio molecular dynamics

simulations, UV-Vis, and XPS spectroscopy. Raman and NMR spectroscopy show that HFEs with higher degree of fluorination coordinate to Li^+ at the expense of MeCN coordination, producing relatively higher free MeCN content in solution. In addition, the solvate electrolytes diluted with highly fluorinated HFEs exhibit lower polysulfide solubility resulting in cleaner Li metal anodes with fewer polysulfide byproducts. This work provides design rules for developing an advanced solvate electrolyte which is sparingly solvating with respect to polysulfides while maintaining reactivity at the cathode.

Table 2.1 Hydrofluoroether cosolvents used for $(\text{MeCN})_2\text{-LiTFSI}$ electrolyte dilution.

abbreviation	full name	structure	molecular weight (g mol^{-1})	boiling point ($^{\circ}\text{C}$)
TTE	1,1,2,2-tetrafluoroethyl 2,2,3,3-tetrafluoropropyl ether		232.07	93.2
OTE	1H,1H,5H-octafluoropentyl 1,1,2,2-tetrafluoroethyl ether		332.09	133
BTFE	bis(2,2,2-trifluoroethyl)ether		182.06	62-63
ETE	ethyl 1,1,2,2-tetrafluoroethyl ether		146.08	57.5

2.2 Experimental Methods

Electrolyte preparation: Lithium bis(trifluoromethylsulfonyl imide) (LiTFSI) salt was purchased from Sigma Aldrich and dried at 130 °C under vacuum for 8 h. Anhydrous acetonitrile (MeCN, 99.8%, Sigma Aldrich), 1,1,2,2-tetrafluoroethyl 2,2,3,3-tetrafluoropropyl ether (TTE, 99%, Synquest Laboratories), 1H,1H,5H-octafluoropentyl 1,1,2,2-tetrafluoroethyl ether (OTE, 97%, Synquest Laboratories) bis(2,2,2-trifluoroethyl)ether (BTFE, 99%, Synquest Laboratories), and ethyl 1,1,2,2-tetrafluoroethyl ether (ETE, 99%, Synquest Laboratories) were dried over activated alumina for 7 days. Chemical structures of all HFEs are shown in **Table 2.1**. The solvate electrolyte, (MeCN)₂-LiTFSI, was prepared by stirring a stoichiometric ratio of 2 mol MeCN and 1 mol LiTFSI overnight in an argon-filled glovebox to yield a clear, colorless, viscous solution. The electrolytes with HFE cosolvents were prepared by diluting the (MeCN)₂-LiTFSI electrolyte with the corresponding HFE at volume ratios of 2:1, 1:1, and 1:2 (solvate:HFE). All electrolytes were prepared in an argon-filled glovebox. The water content of electrolytes measured with Karl Fisher (Photovolt Aquatest Karl-Fischer Coulometric Titrator) is less than 10 ppm in all cases.

Two-electrode Swagelok cell preparation: S₈ infiltrated mesoporous carbon (S@CMK-3) was prepared by melt diffusion of S₈ (99.98%, Sigma-Aldrich) in ordered mesoporous carbon, CMK-3 (BET-1000, ACS Material), at 150 °C as described previously.⁹ The S@CMK-3 composite material was prepared at 50 wt% of S₈. The cathode slurry consisting of 80 wt% S@CMK-3, 10 wt% carbon black (Super P Li, Timcal Inc.), and 10 wt% polyvinylidene fluoride (PVDF, Kynar 2801) binder was mixed with anhydrous N-methyl-2-pyrrolidone (NMP, Sigma-Aldrich). The slurry was cast onto an aluminum substrate and dried overnight at 55 °C. The electrodes were then punched into 0.5” diameter electrodes to yield cathodes with a S₈ loading of

0.24–0.4 mg cm⁻². Li–S cells were assembled in a modified Swagelok tube apparatus (nylon, 0.5” inner diameter, Chicago Fluid System Technologies). The two electrode Swagelok cell consisted of a Li metal anode (99.99%, Alfa Aesar), a 2400 Celgard separator, and the S@CMK–3 cathode. The electrolyte volume was controlled at 20 µL resulting in a S₈ mass to electrolyte volume ratio of ~20 g L⁻¹.

Electrochemical measurements: The Li–S batteries were cycled in the Swagelok cell at the rate of 0.05 C (calculated using the weight of S₈) for the first two cycles and 0.1 C for the following cycles using an Arbin Battery Tester (Model BT 2043, Arbin Instruments Corp., USA). In order to assure electrode wetting, the cells were allowed to rest at open circuit for at least 12 h before cycling. The Li–S cell cycling was performed at room temperature (~23 °C). Coulombic efficiency (CE) was determined by $CE = Q_{\text{discharge, (n+1)th cycle}} / Q_{\text{charge, (n)th cycle}} \times 100\%$. The potential window for battery cycling was controlled between 3.0 V and 1.5 V (vs. Li/Li⁺). All potentials are referenced to Li/Li⁺.

The cycling stability of the Li metal anodes was evaluated in Li–Li symmetric Swagelok cells fitted with 2400 Celgard separators. The electrolyte volume was 30 µL. Galvanostatic cycling was performed on an Arbin Battery Tester (Model BT 2043, Arbin Instruments Corp., USA) by applying a constant current of $\pm 0.5 \text{ mA cm}^{-2}$ for 1 h in each half cycle. The amount of Li plated/stripped was 0.5 mAh cm⁻². The Li metal plating/stripping experiments were performed at room temperature (~23 °C).

Physicochemical property measurement: The viscosity of electrolyte was measured with a VISCOLab 4000 (Cambridge Viscosity by PAC Corporate) at $25.0 \pm 0.02 \text{ °C}$, the temperature was equilibrated by CF41 Cryo-Compact Circulator (JULABO USA Inc.). The ionic conductivity was determined by AC impedance spectroscopy (BioLogic SP-150) in a symmetric

cell at room temperature (~ 23 °C). The density of electrolytes was measured in a 1.00 mL volumetric flask.

Raman spectroscopy measurement: Raman spectroscopy of the electrolytes was measured in 5 mm NMR tubes sealed under argon with an experimental setup reported previously.³⁵⁻³⁶ The measurement was carried out at room temperature (~ 23 °C). A 50 mW 632.8 nm He–Ne laser (Meredith Instruments) was used for sample excitation and laser power at sample was 10 mW. The spectral resolution was ~ 3 cm⁻¹ and a good S/N ratio was achieved from acquisition times of 240 s or 480 s per spectrum. Curve fitting was performed using a Gaussian function to determine the peak area.

NMR spectroscopy measurement: ⁷Li NMR measurements were performed on a 600 MHz Varian instrument in 5 mm screw cap NMR tubes with a 5 mm autox DB probe with Z-gradient capability at the University of Illinois at Urbana–Champaign School of Chemical Sciences NMR laboratory. External standards containing 10 M LiCl in D₂O were inserted in each sample in the form of coaxial sealed capillary. The 90° pulse-width was calibrated for each sample at every temperature. The T₁ longitudinal relaxation time was measured using the inversion-recovery pulse sequence. The T₁ values were calculated by fitting the intensity of the peak as a function of relaxation delay to an exponential function. The ⁷Li T₁ measurements were performed over a wide temperature range (from -35 °C to 70 °C) to observe the T₁ minimum. Between each temperature point, the samples were allowed to rest for 15 min to achieve thermal equilibrium. ¹⁵N NMR measurements were also performed on a 600 MHz Varian instrument in 5 mm screw cap at the UIUC SCS NMR laboratory. The ¹⁵N NMR spectra were obtained at room temperature (~ 23 °C). ¹⁵N chemical shifts were referenced to an external standard NH₄¹⁵NO₃ in D₂O (at -4 ppm) introduced to each sample via a coaxial sealed capillary.

Ab initio molecular dynamics simulation: We performed ab initio molecular dynamics (AIMD) simulations using a density functional theory (DFT) projector-augmented wave (PAW) formalism within the generalized gradient approximation (GGA) as implemented in Vienna Ab-initio Simulation Package (VASP).³⁷⁻³⁸ The bulk electrolytes were simulated using a computational supercell ($18 \text{ \AA} \times 18 \text{ \AA} \times 18 \text{ \AA}$) consisting of ~ 400 atoms, with periodic boundary conditions along all directions. Five different electrolyte systems were simulated, including the neat $(\text{MeCN})_2\text{-LiTFSI}$ solvate as well as the $(\text{MeCN})_2\text{-LiTFSI:HFE}$ diluted with four different HFEs (i.e., TTE, OTE, BTFE, and ETE) at 1:1 volume ratio. In the simulations, the density of the electrolyte was fixed close to experimentally measured values (See **Table 2.2** for the measured density values). We employed the PAW pseudopotentials supplied by VASP while the exchange correlation was described by the Perdew-Burke-Ernzerhof functional.³⁹ Long-range van der Waals dispersion interactions were treated using DFT-D2 method of Grimme.⁴⁰ The plane wave energy cut-off was set at 520 eV, while the Brillouin zone is sampled at Γ -point only. For each of the bulk electrolyte systems, the initial configuration was made up of LiTFSI, MeCN, and HFE molecules placed at random locations with arbitrary orientations. Each system was equilibrated at 300 K in the canonical ensemble (NVT)⁴¹ for 6 ps with a time step of 0.5 fs. A constant temperature condition was maintained using Nose-Hoover thermostat. The solvation structure around the Li^+ ions (made up of all molecules that contain at least one atom within 2.7 \AA of the Li^+ ion) was averaged over the last 1 ps of the AIMD runs.

Quantum chemical cluster calculations: The thermodynamic properties of the Li^+ solvation structure obtained from AIMD simulations were further investigated using DFT quantum chemical (QC) cluster calculations as implemented in the Gaussian 09 code.⁴² The solvation cluster in the first coordination layer around Li^+ in the neat $(\text{MeCN})_2\text{-LiTFSI}$ is

considered first for the structure and energy evaluations. From these species, the thermodynamic feasibility of replacing one MeCN molecule in the solvate structure with different HFEs was computed. To accomplish this, we optimized several geometries containing one TFSI⁻ anion, one MeCN, and one molecule of a particular HFE around Li⁺, including those sampled from our AIMD trajectories. In each of these cases, the long range corrected hybrid functional, ω B97x-D,⁴³ with 6-31+G(d,p) basis set was used to optimize the geometry and to evaluate the electronic energy (E), enthalpy (H), and Gibbs free energy (G) in the gas phase. For all species, a single point energy calculation (E_{solvent}) using a ‘Conductor-like Polarizable Continuum Model’ (CPCM)⁴⁴ was performed using acetonitrile medium ($\epsilon = 36.6$) at the ω B97x-D/6-31+G(d,p) level of theory to approximate the solvation energy ($\Delta E = E_{\text{solvent}} - E_{\text{gas}}$). The enthalpy of binding Li salt with solvent molecules in solution (H_{soln}) was approximated by taking the sum of the gas phase enthalpy of binding (ΔH_{gas}) and the change in solvation energy upon binding ($\Delta E_{\text{solvent}}$).

Polysulfide solubility measurement: A solid form of “Li₂S₈” was prepared by dissolving a stoichiometric ratio of S₈ and Li₂S in MeCN with stirring at 70 °C overnight. The MeCN solvent was removed by placing the polysulfide solution under active vacuum for ~8 h. The solvate:HFE solutions saturated with “Li₂S₈” were prepared by adding 50 mM of “Li₂S₈” in solvate:HFE mixtures and stirring at 70 °C for 24 h followed by a rest period at room temperature for at least 72 h prior to measurements. After the rest period, a precipitate of undissolved solid was observed. Therefore, the solvate:HFE solutions were assumed to be saturated with lithium polysulfide.²⁰ The supernatant solutions were then interrogated by a UV-Vis spectroscopy (Cary 5000 UV-Vis-NIR Spectrophotometer). A baseline correction was performed to avoid any absorbance from the neat solvate:HFE solutions.

Surface characterization: X-ray photoelectron spectroscopy (XPS) was performed by using a Kratos AXIS Ultra spectrometer equipped with an Al K α (1486.6 eV) X-ray source. All binding energies were referenced to the C 1s peak at 284.8 eV. The XPS spectra were analyzed by subtracting the background using the Shirley method and fitting with a Voigt function (70% Gaussian-30% Lorentzian). Li metal samples were prepared by disassembling the Li-S cell after the 100th cycle while the cell was in the fully charged state, followed by rinsing thoroughly with 1,3-dioxalane (DOL) solvent, and drying under vacuum overnight before characterization. The samples were exposed briefly to air when transferring into the vacuum chamber for the XPS measurement.

Table 2.2 Physicochemical properties of the (MeCN)₂-LiTFSI solvate electrolyte diluted with HFE at a 1:1 volume ratio.

electrolyte	mole ratio of MeCN:LiTFSI:HFE	density (g mL ⁻¹)	LiTFSI concentration (M)	viscosity (cP)
solvate:TTE (1:1)	2 : 1 : 1.636	1.476	1.971	9.837
solvate:OTE (1:1)	2 : 1 : 1.212	1.546	2.003	15.62
solvate:BTFE (1:1)	2 : 1 : 1.893	1.420	1.989	5.734
solvate:ETE (1:1)	2 : 1 : 2.010	1.334	2.013	4.739

Table 2.3 Physicochemical properties of the (MeCN)₂-LiTFSI solvate electrolyte and its HFE diluents at a 2:1 volume ratio. ^aThis value is taken from ref 21.

electrolyte	mole ratio of MeCN:LiTFSI:HFE	density (g mL ⁻¹)	LiTFSI concentration (M)	ionic conductivity (mS cm ⁻¹)	viscosity (cP)
neat solvate	2 : 1 : (no HFE)	1.459	3.952	1.35 ^a	140.2
solvate:TTE (2:1)	2 : 1 : 0.818	1.465	2.620	1.54	24.99
solvate:OTE (2:1)	2 : 1 : 0.606	1.503	2.635	1.16	37.77
solvate:BTFE (2:1)	2 : 1 : 0.946	1.436	2.651	2.13	17.34
solvate:ETE (2:1)	2 : 1 : 1.005	1.376	2.667	1.88	16.34

2.3 Results and Discussion

2.3.1 Electrochemical Performance of Li-S cells with the HFE-Diluted (MeCN)₂-LiTFSI Solvate Electrolytes

HFE cosolvents with varying degrees of fluorination and symmetry about the ether were evaluated as cosolvents in the (MeCN)₂-LiTFSI solvate electrolyte to determine the effect of the HFE structure on the electrochemical performance of the Li-S battery. The structures, molecular weights, and boiling points of each HFE are shown in **Table 2.1**, including the previously studied TTE,^{20-21, 25, 27} BTFE,³⁰⁻³¹ and ETE.³³ The HFEs were chosen due to their commercial availability and diverse functionality. For example, the degree of fluorination is highest in the OTE (75%), followed by TTE (66.6%), BTFE (60%), and finally ETE (40%). ETE is the only HFE containing a terminal -CH₃ and BTFE is the only HFE with a terminal -CF₃ moiety. BTFE is also the only symmetric HFE.

The electrochemical performance of the Li-S cells with HFE-diluted solvate electrolytes was evaluated by galvanostatic cycling experiments. **Figure 2.2** shows the discharge capacity and Coulombic efficiency (CE) as a function of cycle number along with representative discharge and charge curves using a S₈ infiltrated mesoporous carbon cathode (S@CMK-3). The capacity fade as a function of cycle number is alleviated upon addition any of the four HFEs relative to the HFE-free solvate electrolyte, consistent with prior results using TTE as a cosolvent.²¹ The degree of capacity retention, however, differs between each HFE with the TTE and OTE yielding higher discharge capacities at 100 cycles relative to cells in which BTFE and ETE were added to the solvate electrolyte. At cycle number 100, TTE and OTE-diluted electrolytes exhibited discharge capacities of 686 mAh g⁻¹ and 546 mAh g⁻¹ whereas the BTFE and ETE cosolvents resulted capacities of only 195 mAh g⁻¹ and 148 mAh g⁻¹, respectively.

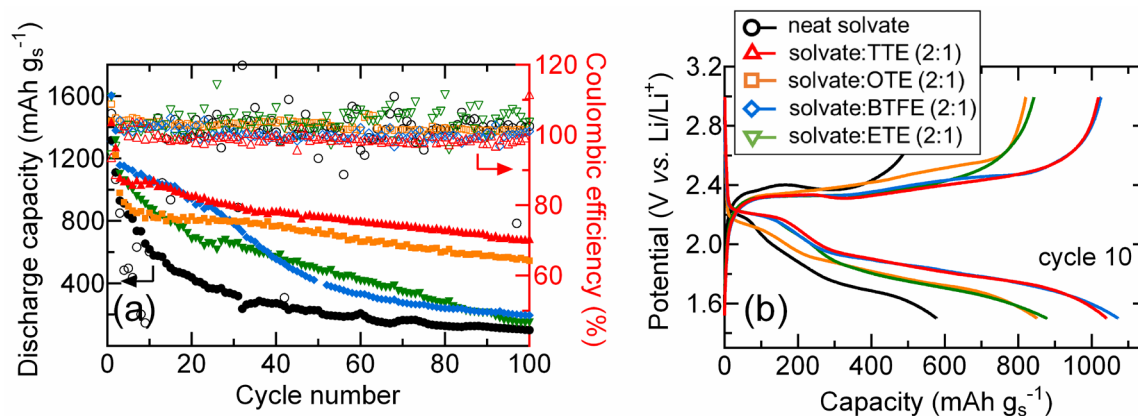


Figure 2.2 (a) Electrochemical performance of Li–S cells prepared with Li metal anode, S@CMK–3 cathode, and neat (MeCN)₂–LiTFSI solvate electrolyte diluted with HFEs at a volume ratio of 2:1 (solvate:HFE). The neat (MeCN)₂–LiTFSI solvate electrolyte is also shown for comparison. The cells are cycled between 1.5 V and 3.0 V at 0.05 C for the first two cycles and 0.1 C for the following cycles. The Coulombic efficiency (CE) shown here is the discharge efficiency and was determined by $CE = Q_{\text{discharge}}/Q_{\text{charge}} \times 100\%$. (b) The corresponding charge and discharge curves for cycle 10. The Li–S cell cycling was performed at room temperature.

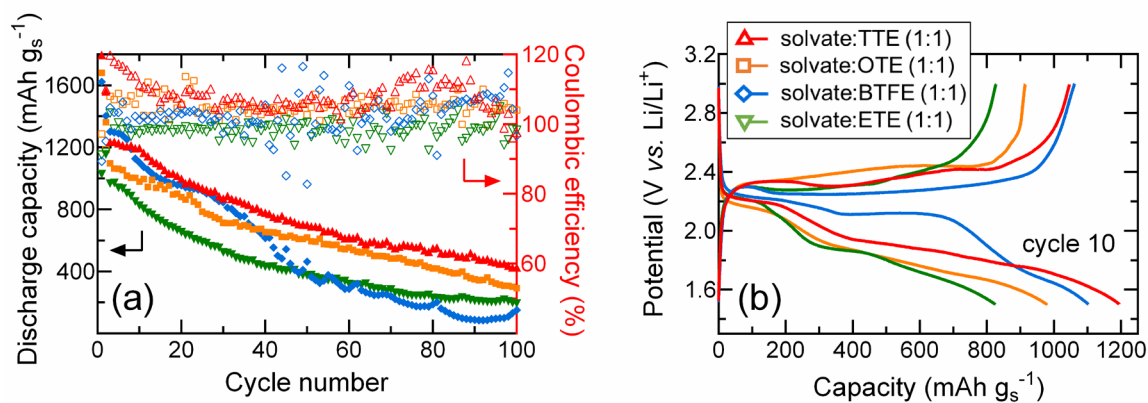


Figure 2.3 (a) Electrochemical performance of Li-S cells prepared with a Li metal anode, S@CMK-3 cathode, and a (MeCN)₂-LiTFSI solvate electrolyte diluted with HFEs at a volume ratio of 1:1 (solvate:HFE). The cells are cycled between 1.5 and 3.0 V at 0.05 C for the first two cycles and 0.1 C for the following cycles. The Coulombic efficiency (CE) shown here is the discharge efficiency and was determined by $CE = Q_{\text{discharge}}/Q_{\text{charge}} \times 100$. (b) Corresponding charge and discharge curves for cycle 10. The Li-S cell cycling was performed at room temperature.

The corresponding Coulombic efficiencies for electrolytes with HFE cosolvents were all ca. 100%, whereas the (MeCN)₂-LiTFSI electrolyte itself exhibits poor Coulombic efficiency with larger deviations from 100%.

The 2:1 solvate:HFE volume ratio shown in **Figure 2.2** produced better cycling behavior compared to a 1:1 ratio and was thus determined to be the optimal composition. The cycling performance of Li-S cells with electrolytes at solvate:HFE ratio of 1:1 is shown in **Figure 2.3**. For the 1:1 system in which the relative amount of HFE is increased compared to the 2:1 system, the beneficial effect of TTE and OTE addition is less pronounced and the Coulombic efficiency becomes unstable exhibiting greater deviations from 100%. Additionally, the capacity fade is more severe and the measured discharge capacities are lower compared to the 2:1 systems. Thus, the HFE content also has a significant effect on the Coulombic efficiency and the discharge capacity of the battery.

Figure 2.2b shows the discharge and charge profiles for the Li-S cells at cycle 10. The features in the discharge and charge profiles measured in electrolytes with HFE are similar to those measured in the neat (MeCN)₂-LiTFSI electrolyte in that two discharge plateaus are observed. The cell with the OTE solvate has a slightly lower first discharge plateau and slightly higher charge plateau compared to other HFE solvates suggesting higher overpotentials for both reduction and oxidation. The larger cell polarization in OTE is likely due to the relatively high viscosity of solvate:OTE (2:1) electrolyte compared to the other HFEs which causes sluggish kinetics (**Table 2.3**).

2.3.2 Origin of HFE Effect

We next evaluate the origin of the improved cycling behavior of the Li-S cell with the addition of TTE and OTE to the (MeCN)₂-LiTFSI solvate electrolyte relative to the other two HFE additives. We consider several possible causes for the improvement, including: viscosity/conductivity effects, solution structure, polysulfide solubility, and SEI on Li metal anode.

2.3.2.1 Physicochemical Properties

Table 2.3 reports the ionic conductivity and viscosity of the (MeCN)₂-LiTFSI solvate electrolyte and the solvate diluted with the four HFEs. The BTFE and ETE diluted electrolytes exhibit significantly higher ionic conductivities and lower viscosities relative to TTE and OTE-containing electrolytes. The cells cycled with the BTFE and ETE diluted electrolytes, however, exhibit the most severe capacity fade compared to the cells cycled with the TTE and OTE diluted electrolytes. Thus, the transport properties of the HFE-containing electrolytes are not the cause for enhanced battery cycling performance between the four HFEs.

2.3.2.2 Solution Structure of the HFE-Diluted MeCN Solvate Electrolytes

Evaluating the local structure of the electrolyte is important to understand the unique behavior of the HFE diluted solvate electrolyte in the Li-S battery. Previous work has shown that the Li⁺ in the (MeCN)₂-LiTFSI electrolyte is highly coordinated by TFSI⁻ anion and MeCN solvent molecules to form a unique solvation structure that differs from the dilute solutions.^{25, 45} Addition of the HFE to the solvate electrolyte was suggested to be inert toward the Li⁺ solvation structure,²¹ however, we have shown that addition of TTE to the (MeCN)₂-LiTFSI changes the

Li⁺ coordination structure.²⁵ A fraction of the TTE coordinates to the Li⁺ at the expense of the MeCN coordination in the solvate complex thereby releasing uncoordinated, or “free” MeCN in solution.²⁵ Because the TTE cosolvent has a significant effect on the local solvation structure of the electrolyte solution, here we determine how different HFEs modify the solution structure of the solvate electrolyte using Raman and NMR spectroscopy along with ab initio molecular dynamics simulations.

Raman Spectroscopy

To interrogate the Li⁺ coordination environment in the HFE-added solvate electrolytes, Raman spectra of (MeCN)₂–LiTFSI with the addition of HFEs at volume ratios of 2:1, 1:1, and 1:2 were obtained. **Figure 2.4a–d** shows the overlaid Raman spectra in two wavenumber regions of each electrolyte normalized to the largest peak intensity. The spectra without normalization is also shown in the **Figure 2.5**. Assignments of Raman modes are shown in **Table 2.4**. The lower wavenumber region shows vibrational modes related to the TFSI[−] anion, modes a and a', and the higher wavenumber region shows vibrational modes related to MeCN, modes b–c. In the case of TFSI[−], mode a corresponds to the expansion and contraction of the entire anion and is particularly sensitive to ionic interactions.^{46–49} It is well-known that the TFSI[−] anion has two low energy conformers: a cisoid and transoid.^{45, 48–50} Due to the structural flexibility of TFSI[−], each conformer could coordinate to Li⁺ in various ways resulting in multiple overlapping bands around 740–750 cm^{−1}.⁴⁵ The frequency difference between each anionic coordination structure is only 1–2 cm^{−1} making it difficult to deconvolute the spectra with high accuracy.⁴⁵ Therefore, the Raman spectra around 740–750 cm^{−1} were fit with two components a (uncoordinated TFSI[−]) and a' (coordinated TFSI[−]) as an approximation. Mode a is located at ~742 cm^{−1} when TFSI[−] is

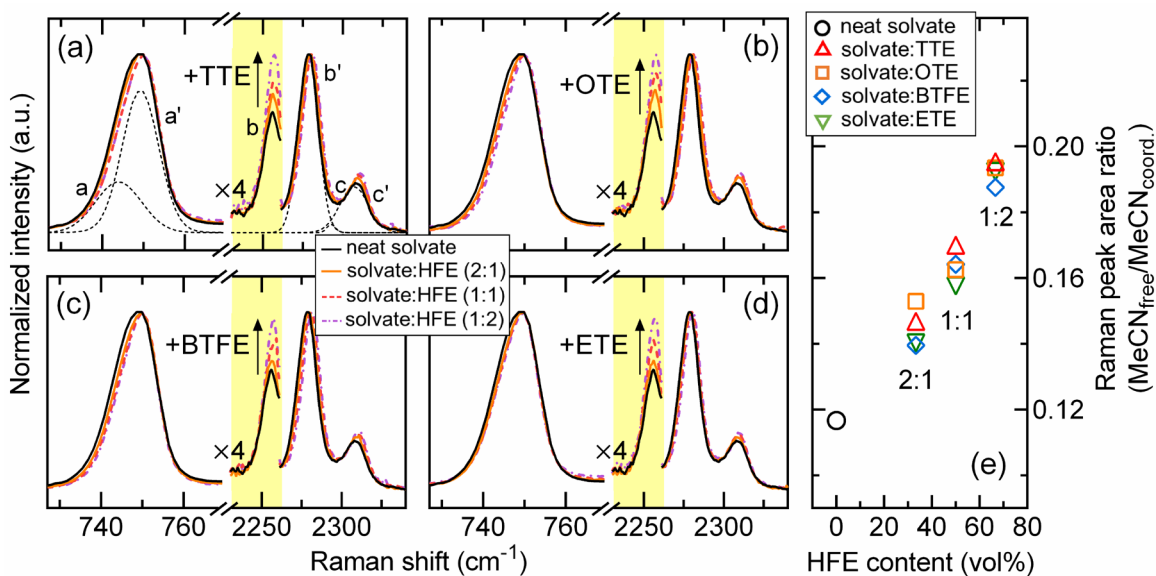


Figure 2.4 Raman spectra of neat (MeCN)₂-LiTFSI solvate electrolyte diluted with (a) TTE, (b) OTE, (c) BTFE, and (d) ETE with volume ratios of 2:1, 1:1, and 1:2 (solvate:HFE). The black dashed line shown in (a) represents the curve fitting results for the neat solvate. The lower wavenumber region shows the TFSI⁻-related modes a and a' and the high wavenumber region shows bands associated with MeCN, modes b, b', c, and c'. The spectra are normalized and overlaid for comparison. The intensity around mode b (2230–2260 cm⁻¹, highlighted with yellow) is multiplied by a factor of four. (e) HFE addition to the (MeCN)₂-LiTFSI solution releases free MeCN, as determined by the peak area ratios of the free MeCN mode to coordinated MeCN (mode b vs. mode b'). The Raman spectra of the solvate:TTE solutions have been published previously²⁵ and are reproduced here. The Raman spectra shown here were obtained at room temperature.

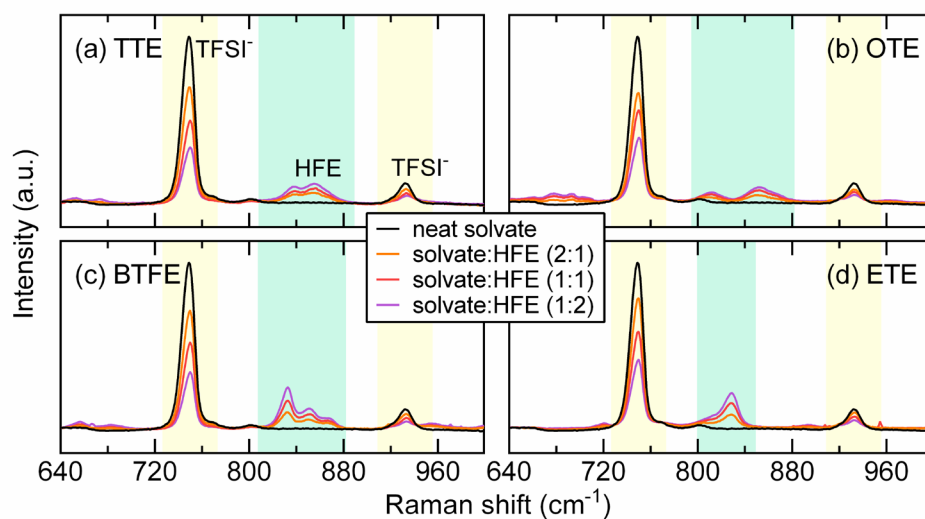


Figure 2.5 Low wavenumber region Raman spectra of neat $(\text{MeCN})_2\text{-LiTFSI}$ solvate electrolyte diluted with (a) TTE, (b) OTE, (c) BTFE, and (d) ETE with volume ratios of 2:1, 1:1, and 1:2 (solvate:HFE). The region highlighted with yellow shows TFSI^- bands and the region highlighted with green shows HFE bands.

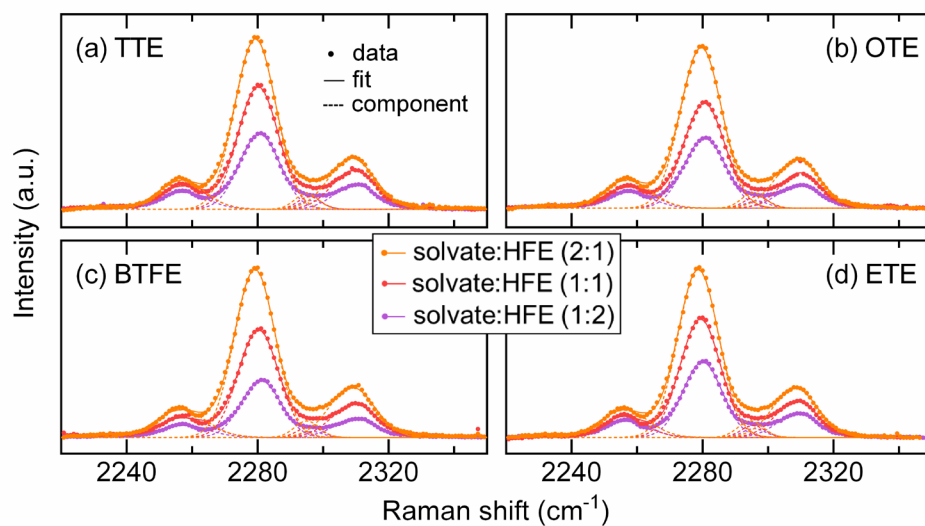


Figure 2.6 High wavenumber region Raman spectra of neat (MeCN)₂-LiTFSI solvate electrolyte diluted with (a) TTE, (b) OTE, (c) BTFE, and (d) ETE with volume ratios of 2:1, 1:1, and 1:2 (solvate:HFE). The spectra are fit with four component using Gaussian profiles.

Table 2.4 Vibrational frequencies and assignments of Raman modes in neat (MeCN)₂-LiTFSI solvate electrolyte.

	peak label	a	a'	b	b'	c	c'	
assignment	species	TFSI ⁻	TFSI ⁻	MeCN	MeCN	MeCN	MeCN	
	modes	$\nu_s(\text{S-N-S}), \delta(\text{SO}_2), \delta(\text{CF}_3)$	mode a, coordinated to Li ⁺	$\nu_s(\text{C}\equiv\text{N})$	mode b, coordinated to Li ⁺	$\nu_s(\text{C-H})$	mode c, coordinated to Li ⁺	
	ref	46-49	25, 45, 47	51-52	25, 45-46, 53	51-52	25	
Raman shift (cm ⁻¹)	(MeCN) ₂ -LiTFSI (solvate)	742	749	2256	2278	2294	2308	
	solvate:TTE vol. ratio	2:1	742	749	2257	2279	2295	2309
		1:1	742	750	2257	2280	2296	2309
		1:2	742	750	2257	2280	2296	2309
	solvate:OTE vol. ratio	2:1	742	749	2257	2280	2296	2309
		1:1	742	749	2257	2280	2296	2310
		1:2	742	750	2257	2281	2296	2310
	solvate:BTFE vol. ratio	2:1	742	749	2257	2279	2295	2309
		1:1	742	750	2257	2280	2296	2310
		1:2	742	750	2257	2281	2296	2310

uncoordinated and is shifted to $\sim 749\text{ cm}^{-1}$ as a result of coordination to Li^+ .^{25, 45-49} The coordinated TFSI^- mode is labeled mode a' in **Figure 2.4**. As reported previously, the TFSI^- mode in the $(\text{MeCN})_2\text{-LiTFSI}$ solvate contains contributions from both mode a and a', with larger contribution from mode a', coordinated TFSI^- .^{25, 45} Upon addition of the four HFEs to the $(\text{MeCN})_2\text{-LiTFSI}$ solvate, the ratio of bands a to a' remains fairly constant and thus the coordination environment around TFSI^- is unchanged as a result of HFE addition. The same trend is observed for all HFEs tested and agrees well with the previously reported result using TTE as a diluent.²⁵

The coordination of MeCN in the Li^+ was studied by interrogating the $\text{C}\equiv\text{N}$ stretching of MeCN molecule. The high wavenumber region in **Figure 2.4a-d** shows the $\text{C}\equiv\text{N}$ stretching vibration, labeled mode b in addition to the C-H stretching band,⁵¹⁻⁵² labeled mode c. MeCN coordination to Li^+ shifts mode b to higher wavenumbers resulting in a new mode labeled b'.^{25, 45-46, 53} Coordination to Li^+ also causes a shift in the C-H stretching mode to mode c', however, this mode is less sensitive to coordination effects and therefore will not be discussed further. The $\text{C}\equiv\text{N}$ stretching mode is a better proxy to investigate the change in coordination environment since the coordination to Li^+ occurs through the lone pair of N.⁴⁵ **Figure 2.4** shows the $(\text{MeCN})_2\text{-LiTFSI}$ solvate complex is mainly composed of coordinated MeCN, mode b', with a small contribution from free MeCN, mode b. The presence of free MeCN implies that coordination number of MeCN in first coordination shell of Li^+ is less than two or that multimers are formed in solution. We have previously shown that as TTE is titrated into $(\text{MeCN})_2\text{-LiTFSI}$, TTE displaces coordinated MeCN increasing the relative amount of free MeCN.²⁵ The same trend is observed with other HFEs including OTE, BTFE, and ETE. As HFE content is increased, from 33% in 2:1 ratio and 50% in 1:1 ratio to 67% in 1:2 ratio, the peak area of mode

b increases relative to that of mode b', indicating that addition of HFE releases free MeCN into solution (**Figure 2.4a–d**). For quantitative analysis, curve fitting was performed to determine the relative peak area ratios of free MeCN and coordinated MeCN (**Figure 2.6**). The fraction of free MeCN relative to coordinated MeCN versus HFE content is shown in **Figure 2.4e**, where the Raman peak area ratio of free MeCN (mode b) to coordinated MeCN (mode b') increases linearly as a function of HFE content. The linear relationship is observed with all HFEs tested with minimal differences between each HFE. We note, however, that the resolution of the Raman measurement is relatively low making it difficult to quantitatively determine small changes in the free MeCN content between the HFEs at the same volume ratios. We can, however, observe measurable differences as the volume of HFE is increased with the free MeCN content increasing as the HFE content increases.

Variable Temperature ^7Li NMR Spectroscopy

To directly probe the coordination environment around the Li^+ cation, ^7Li NMR measurements of the $(\text{MeCN})_2\text{-LiTFSI}$ and its HFE diluents were performed. **Figure 2.7** shows the ^7Li longitudinal relaxation time, T_1 , measured as a function of HFE dilution at different temperatures. NMR relaxation measurements are a powerful method to examine the local environment and dynamics of the nucleus at a local level and evaluate the local symmetry around the ^7Li nucleus. T_1 is the decay constant related to the nuclear spin relaxing back to its equilibrium state in an external magnetic field. ^7Li is a quadrupolar nuclei where the charge distribution within the nucleus is non-uniform, therefore relaxation is affected by the changes in the symmetry of the electron density around Li. Quadrupolar nuclei distribute energy through quadrupolar relaxation mechanism and this mechanism is assumed to be the dominating

relaxation mechanism.⁵⁴⁻⁵⁵ Therefore, for ^7Li , changes in T_1 can be regarded as arising from changes in the local bonding environment of Li. T_1 , however, is sensitive not only to changes in the local symmetry but also changes in the mobility of the complex. As HFE is added to the solvate, the viscosity of the solution decreases significantly causing a change in T_1 . Variable temperature ^7Li T_1 experiments were performed to decouple these two effects. A shift of the T_1 minimum to lower temperature ranges reflects an increase in mobility and a shift in the T_1 minimum to faster time scales (i.e., T_1 values become shorter) indicates a change in the local environment of the nucleus.⁵⁴⁻⁵⁵

Figure 2.7 shows the variable temperature T_1 curves for the $(\text{MeCN})_2\text{-LiTFSI}$ solvate electrolyte and $(\text{MeCN})_2\text{-LiTFSI}$ diluted with HFE cosolvents at volume ratios of 2:1, 1:1, and 1:2. Overall, the T_1 minimum of the curve shifts to the lower temperature range with increasing HFE content for all HFEs, indicating enhanced mobility of the complex due to the lower viscosity of the HFE diluted solutions. Qualitatively, the magnitude of the temperature shift at which the T_1 minimum is observed relative to the T_1 minimum in the solvate (i.e., shift of the T_1 curve along the x-axis) as a result of HFE addition follows the order of $\text{BTFE} \approx \text{ETE} > \text{TTE} > \text{OTE}$. This implies that the order of viscosity of the HFE added solvates is $\text{OTE} > \text{TTE} > \text{BTFE} \approx \text{ETE}$, consistent with the measured viscosity value shown in **Table 2.3**.

The addition of HFEs to the $(\text{MeCN})_2\text{-LiTFSI}$ also results in a shift of T_1 minimum to faster time scales along the y-axis, suggesting a change in local coordination environment around Li^+ . HFE addition to the solvate modifies the Li^+ local environment so that the local symmetry around Li becomes more asymmetric, as evidenced by the shift of T_1 minimum to shorter times with increased HFE content. Such a shift could be caused by the replacement of coordinated MeCN by HFE molecules which have high electron density around O and F atoms, resulting in

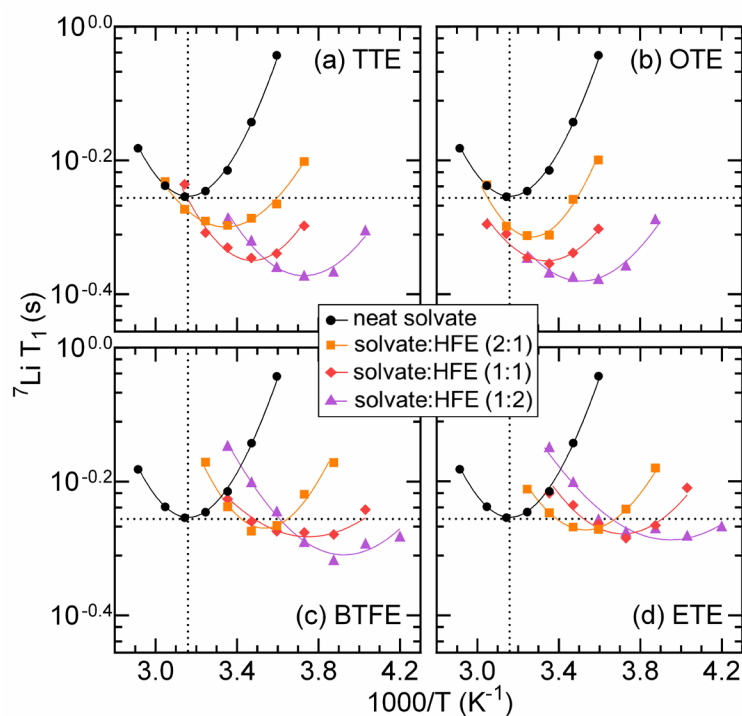


Figure 2.7 Variable temperature ^7Li T_1 curves for the neat $(\text{MeCN})_2\text{-LiTFSI}$ solvate, and the solvate diluted with (a) TTE, (b) OTE, (c) BTFE, and (d) ETE at volume ratios of 2:1, 1:1, and 1:2. The T_1 minimum is observed in each sample within the temperature range of $-35\text{ }^\circ\text{C}$ and $70\text{ }^\circ\text{C}$. Lines represent the fit of the data to the BPP equation.⁵⁴

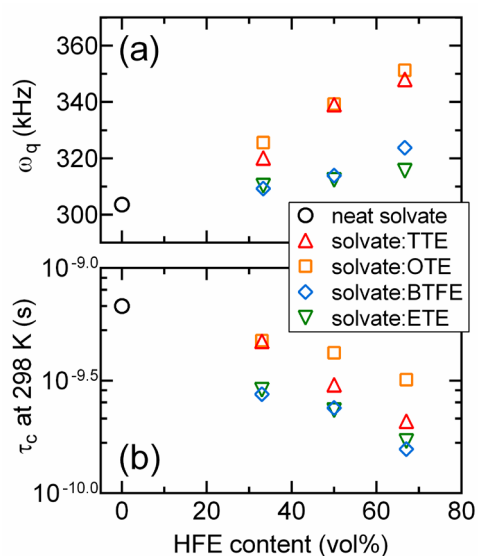


Figure 2.8 Fit parameters of BPP equation to ^7Li variable temperature T_1 measurements. (a) quadrupolar coupling constant, ω_q , and (b) correlation time, τ_c , at 298 K of the ^7Li nuclei in neat $(\text{MeCN})_2\text{-LiTFSI}$ solvate, and the solvate diluted with TTE, OTE, BTFE, and ETE are shown as a function of HFE content.

the asymmetry of electron density around Li^+ . The shift of T_1 minimum along the time axis is observed for all HFEs used, but the shift is more pronounced in the case of TTE and OTE-added solvates while relatively small shifts were induced by BTFE and ETE addition as shown in **Figure 2.7**. Thus, it is likely that a fraction of HFE coordinates to Li^+ likely at the expense of MeCN coordination and that TTE and OTE exhibit a higher tendency to coordinate to Li^+ relative to the other two HFEs.

For quadrupolar ^7Li nuclei experiencing isotropic reorientational diffusion, the T_1 can be modeled by Bloembergen, Purcell, and Pound (BPP) theory, given in Equation (1),⁵⁴⁻⁵⁵

$$\frac{1}{T_1} = \frac{\omega_q^2}{50} \left(\frac{\tau_c}{1 + \omega_0^2 \tau_c^2} + \frac{4\tau_c}{1 + 4\omega_0^2 \tau_c^2} \right) \quad (1)$$

where ω_q is the quadrupolar coupling constant, τ_c is the correlation time, and ω_0 is the Larmor frequency. The quadrupolar coupling constant, ω_q , is a measure of the energy of interaction between the nuclear quadrupolar moment, which is an intrinsic property of the nucleus, and the electric field gradients (EFGs) generated by its surroundings.⁵⁵ The correlation time, τ_c , for molecular reorientation is defined in Equation (2),⁵⁵

$$\tau_c = \tau_0 \exp \left(E_a / RT \right) \quad (2)$$

where τ_0 is the correlation time constant, E_a is the activation energy for molecular reorientation, and R is the gas constant. According to Equation (1), T_1 exhibits a minimum at $\omega_0 \tau_c = 0.616$, which means the correlation time where the minimum occurs is constant.⁵⁶ The T_1 minimum obtained from fitting the data in **Figure 2.7** was used to calculate ω_q for all of the electrolytes. τ_c was calculated at each temperature from the experimental T_1 value. The fit parameters give more detailed information about the system. We note that more accurate values can be obtained by fitting data obtained over a broader temperature window.

Figure 2.8 shows the fit parameters of BPP equation to experimental T_1 curves shown in **Figure 2.7**. **Figure 2.8a** shows the quadrupolar coupling constant in units of frequency as a function of HFE content. In general, for all HFEs examined, the ω_q increases as more HFE is titrated into the solvate solution (**Figure 2.8a**). An increase in ω_q suggests larger oscillating electric field gradients (EFGs) around Li^+ and therefore efficient exchange of energy between Li^+ with its surroundings. We note here that the slope is larger with TTE and OTE-added solvate solutions than electrolytes with BTFE and ETE cosolvents. The larger ω_q in TTE and OTE system was also confirmed by shorter T_1 values, as large EFGs result in fast relaxation and short T_1 processes. These data taken together suggests addition of TTE and OTE induces more asymmetry of electron density around Li^+ relative to the $(\text{MeCN})_2\text{-LiTFSI}$ solvate complex by replacing either coordinated MeCN or TFSI⁻ anion. Raman spectroscopy suggests that the coordination of the TFSI⁻ anion is relatively unchanged after HFE addition whereas higher free MeCN was released as HFE is added to the solvate. Therefore, we hypothesize that the change in local symmetry around Li^+ is the result of HFE coordination and the release of free MeCN.

Figure 2.8b shows the correlation time of $(\text{MeCN})_2\text{-LiTFSI}$ solvate and its HFE-added solutions at 298 K. The ^7Li correlation time for TTE and OTE is again higher relative to the other two HFEs. The higher correlation time is associated with worse Li^+ ion mobility in the solvate electrolyte in which TTE and OTE were added relative to those in which ETE and BTFE were added, consistent with the higher viscosity of TTE and OTE solutions reported in **Table 2.3**.

¹⁵N NMR Spectroscopy

¹⁵N NMR was used to further verify the effect of HFE addition on the coordination environment of MeCN in the solvate electrolyte. Although the low natural abundance of ¹⁵N (0.365%) poses a challenge to collecting high signal-to-ratio spectra, the ¹⁵N spin-1/2 nucleus yields sharp NMR lines and its wide chemical shift range and cation affinity make it a good probe for ionic coordination.⁵⁷ Raman spectroscopy and variable temperature T₁ measurements suggest that both quantity and types of HFE cosolvent affect the equilibrium between free and coordinated MeCN in solvate electrolyte. Therefore, it is worthwhile to examine Li⁺–MeCN interaction directly by monitoring changes in chemical shift of ¹⁵N nucleus in MeCN as a function of LiTFSI addition and HFE dilution. The ¹⁵N chemical shifts of MeCN solvate and its HFE diluents were used as a proxy to probe the coordination of MeCN to the Li⁺ with high sensitivity (**Figure 2.9**).

Figure 2.9a–d show the ¹⁵N NMR spectra of the solvate:HFE electrolyte solutions with the corresponding MeCN:HFE solutions without LiTFSI salt as a reference in each case. **Figure 2.9a** shows the case in which the resonance of the ¹⁵N nucleus shifts upfield by 20.535 ppm as a result of LiTFSI addition to the MeCN:TTE solution. The shift is due to the shielding effect of Li⁺ on the N lone pair as a result of MeCN coordination to Li⁺.⁵⁷ The displacement relative to the solution without any salt, in this case the neat MeCN:TTE, is given by Δδ which can be used as a proxy to indicate the extent of Li⁺–MeCN coordination.⁵⁷ We note the large viscosity difference between the neat MeCN and (MeCN)₂–LiTFSI solution could also affect the ¹⁵N chemical shift (**Figure 2.10**), and this system is not discussed here. Instead, the viscosity difference between the MeCN:HFE and solvate:HFE is negligible, therefore any chemical shift displacement is the result of changes in the local bonding environment of N atoms in MeCN.

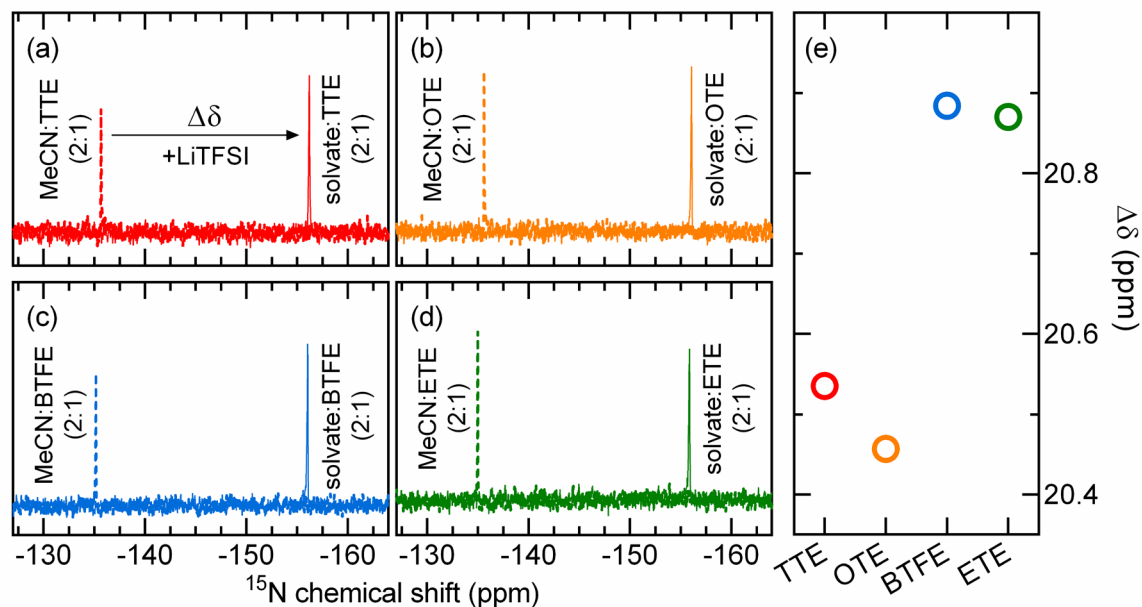


Figure 2.9 (a–d) ^{15}N NMR spectra of 2:1 mixture (by volume) of MeCN:HFE and solvate:HFE, as indicated. ^{15}N chemical shifts were referenced to $\text{NH}_4^{15}\text{NO}_3$ in D_2O at -4 ppm. (e) The displacements in ^{15}N chemical shifts ($\Delta\delta$) induced by an addition of Li^+ salt with respect to the MeCN:HFE mixtures are shown. The NMR spectra shown here were acquired at room temperature.

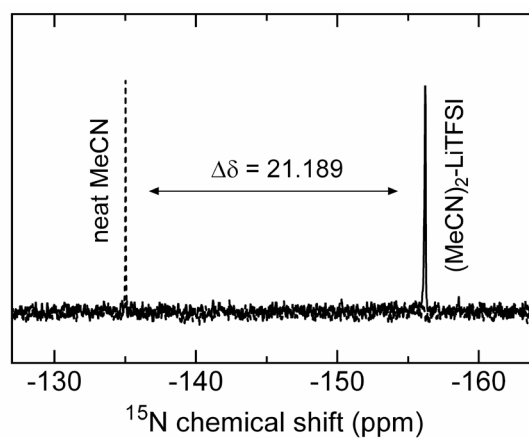


Figure 2.10 ^{15}N NMR spectra of neat MeCN and $(\text{MeCN})_2\text{-LiTFSI}$ as indicated. The resonance of the ^{15}N nucleus shifts upfield by 21.189 ppm as a result of LiTFSI addition to the MeCN. ^{15}N chemical shifts were referenced to $\text{NH}_4\text{NO}_3\text{-}^{15}\text{N}_2$ in D_2O .

Figure 2.9e shows that the displacements relative to the neat MeCN:HFE solutions ($\Delta\delta$) are smaller in TTE and OTE than those observed in BTFE and ETE, which indicates that the degree of Li^+ –MeCN coordination is less in TTE and OTE-added solutions. This is the consequence of stronger interaction between Li^+ and TTE/OTE than other HFEs, resulting in a displacement of coordinated MeCN from the solvate structure and a release of free MeCN in solution. In other words, the smaller the $\Delta\delta$ the higher the free MeCN content and is in the order of $\text{OTE} > \text{TTE} \gg \text{ETE} \approx \text{BTFE}$. This suggests that the TTE and OTE-added solvates have more free MeCN than the solvates with BTFE and ETE. We note that the exchange between MeCN and HFE is fast on the timescale of NMR experiments resulting in a single ^{15}N resonance which is the concentration-weighted average of free MeCN and coordinated MeCN. TTE and OTE exchanges with coordinated MeCN more readily resulting in higher free MeCN in solution.

Ab Initio Molecular Dynamics Simulations and Quantum Chemical Calculations

To further investigate the effect of addition of HFE on the coordination environment of Li^+ in $(\text{MeCN})_2\text{--LiTFSI}$ solvate electrolytes, we performed ab initio molecular dynamics (AIMD) simulations and quantum chemical (QC) cluster calculations. AIMD simulations in the neat $(\text{MeCN})_2\text{--LiTFSI}$ solvate indicate that the first solvation shell around almost every Li^+ is composed of one TFSI^- anion and two MeCN molecules (**Figure 2.11a**), consistent with previous spectroscopic and theoretical studies.^{25, 45} In this solvation complex, the Li^+ ions coordinate with MeCN through the N atom (Li–N distance $\sim 2.1\text{--}2.3$ Å), while they coordinate with the TFSI^- anion through the O atoms of the sulfonyl group (Li–O separation $\sim 1.98\text{--}2.1$ Å). A minor fraction of TFSI^- anions bind with more than one Li^+ center that results in small amount of uncoordinated MeCN in good agreement with previous investigations.^{25, 45} Consequently, a

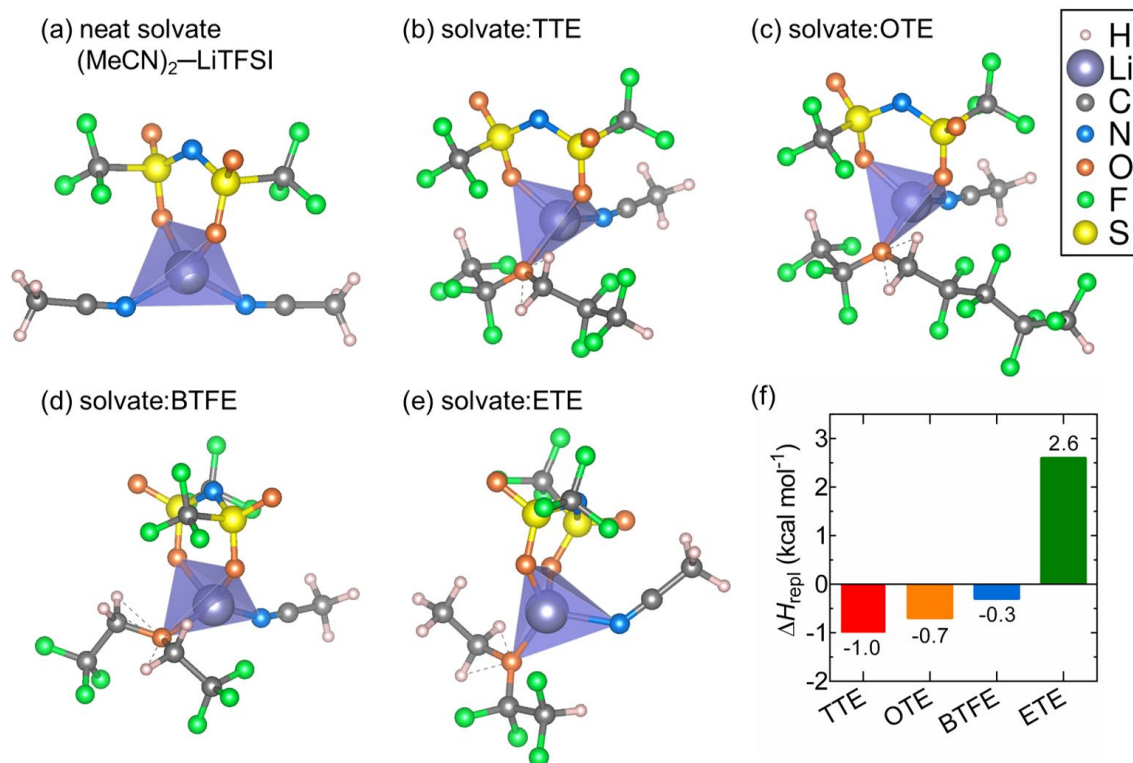


Figure 2.11 Quantum chemical calculations to understand effect of HFE addition on coordination environment around Li⁺ in (MeCN)₂-LiTFSI solvate electrolytes. (a) Atomic configuration of solvation shell around Li⁺ in neat (MeCN)₂-LiTFSI solvate obtained from AIMD simulations. (b–e) The most stable atomic configuration upon replacing one MeCN shown in (a) with TTE, OTE, BTFE, and ETE molecule respectively obtained from QC calculations. (f) Enthalpy change associated with replacing one MeCN in the Li⁺ solvation shell of (MeCN)₂-LiTFSI solvate with different HFE molecules (ΔH_{repl}) in a dielectric medium at 298 K. The calculations were carried out by Dr. Badri Narayanan and Dr. Rajeev S. Assary at Argonne National Laboratory.

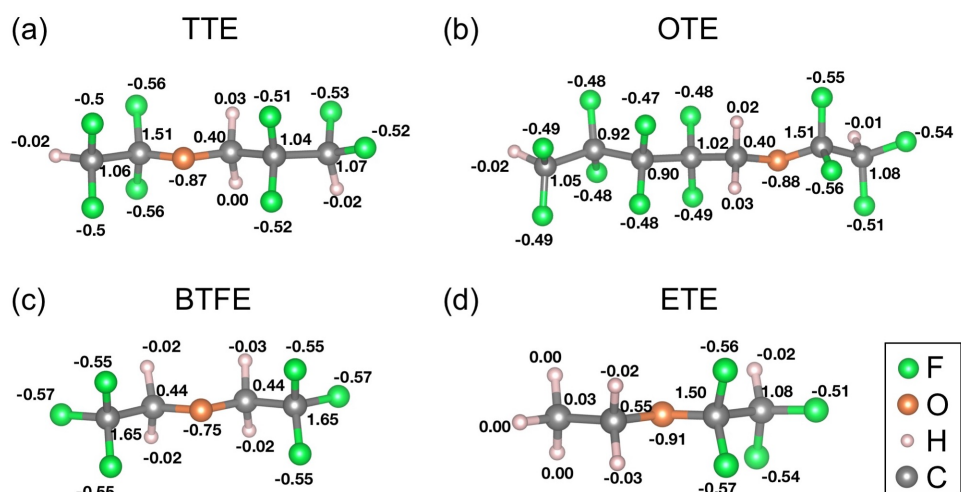


Figure 2.12 Atomic partial charges of (a) TTE, (b) OTE, (c) BTFE, and (d) ETE derived from quantum chemical calculations. The calculations were carried out by Dr. Badri Narayanan and Dr. Rajeev S. Assary at Argonne National Laboratory.

small fraction of MeCN molecules ($\sim 8\%$) are found to be uncoordinated in neat $(\text{MeCN})_2\text{-LiTFSI}$ solvate from the AIMD simulations at 300 K. Upon addition of HFE to $(\text{MeCN})_2\text{-LiTFSI}$, we observe that the HFE molecules replace the MeCN in the solvation shell around Li^+ without affecting the TFSI coordination around Li^+ and, in turn, release free MeCN. This is consistent with the Raman spectroscopy results reported in this work (**Figure 2.4**), as well as our recent work on TTE-diluted $(\text{MeCN})_2\text{-LiTFSI}$ solvate system.²⁵ The nature of the HFE diluent, however, significantly affects the amount of MeCN released (in this paper “released” MeCN is obtained by counting the MeCN molecules whose N atoms are at least 2.7 Å away from each Li^+ in the system). AIMD simulations on $(\text{MeCN})_2\text{-LiTFSI}$ solvate diluted with HFEs at 1:1 volume ratio show that BTFE and ETE release $\sim 43\%$ and $\sim 28\%$ of free MeCN, respectively. On the other hand, higher fractions of free MeCN are released in electrolytes diluted with TTE ($\sim 57\%$) and OTE ($\sim 50\%$). This is qualitatively in good agreement with the ^{15}N NMR studies (**Figure 2.9**).

Next, we identify the thermodynamic origin for the higher tendency of TTE and OTE (as compared to BTFE and ETE) to release free MeCN in $(\text{MeCN})_2\text{-LiTFSI}$ solvate using QC calculations. **Figure 2.11b–e** shows the most stable configuration of the Li^+ solvation complex upon replacing one MeCN molecule in the $(\text{MeCN})_2\text{-LiTFSI}$ solvate structure (obtained from AIMD simulation shown in **Figure 2.11a**) with different HFEs. In each configuration, the HFE molecule coordinates with Li^+ through the ethereal O atom (with Li–O separation distance $\sim 2.1\text{--}2.3$ Å). This preferential association of Li^+ with ethereal O is a manifestation of the relative partial charge distribution in the HFE molecules. For all four HFEs, our QC calculations show that the ethereal O atoms possess the highest (negative) partial charge in the molecule with values -0.75 to -0.91 (in comparison, F atoms have an average charge of ~ -0.54). The atomic

partial charge in each HFE is shown in **Figure 2.12**. This negative partial charge on O atom makes it the most electronegative atom in the HFE, and consequently, the preferred site for Li^+ binding. In addition, formation of these MeCN-LiTFSI-HFE complexes is reasonable since their computed solvation free energies ΔG_{solv} (TTE: $-14.76 \text{ kcal mol}^{-1}$; OTE: $-15.22 \text{ kcal mol}^{-1}$; BTFE: $-14.76 \text{ kcal mol}^{-1}$; ETE: $-9.45 \text{ kcal mol}^{-1}$) are comparable to that of $(\text{MeCN})_2\text{-LiTFSI}$ solvate ($\Delta G_{\text{solv}} \approx -16.37 \text{ kcal mol}^{-1}$).

Figure 2.11f provides the enthalpy change associated with replacing a MeCN molecule in $(\text{MeCN})_2\text{-LiTFSI}$ solvate structure with each HFE. Evidently, replacing a MeCN molecule with BTFE or ETE is more endothermic as compared to TTE and OTE. This makes replacement of MeCN with TTE/OTE more energetically favorable (i.e., more likely) as compared to BTFE or ETE. Therefore, diluting $(\text{MeCN})_2\text{-LiTFSI}$ solvate with TTE or OTE results in a higher amount of free MeCN as compared to that with BTFE or ETE, consistent with the ^{15}N NMR experiments shown in **Figure 2.9**.

The formation of free MeCN in solvate electrolytes could affect the battery cycling performance in different ways. In the presence of free MeCN, kinetics of the S_8 reduction/oxidation processes are improved by the capability of free MeCN to solubilize polysulfide intermediates.²⁵ Instead of forcing the S_8 reduction/oxidation pathway to follow a putative solid-state conversion reaction, the presence of a polysulfide solvating molecule, MeCN, facilitates the S_8 reaction kinetics.²⁵ The improved kinetics at the electrolyte/electrode interface is likely to result in good battery cyclability. However, the presence of free MeCN could also affect other cell functionalities. For example, MeCN can affect the stability of the Li metal anode through the spontaneous reaction of Li metal with MeCN to form an unstable SEI during long term battery cycling.⁵⁸ Additionally, free MeCN in the solvate, while improving S_8

reduction/oxidation kinetics, could also affect polysulfide dissolution and diffusion. Therefore, it is important to examine the effect of free MeCN on the Li metal anode and on polysulfide solubility to deconvolute the beneficial effect of TTE and OTE cosolvents.

2.3.2.3 Li Metal Anode Stability and Lithium Polysulfide Solubility in the HFE-Diluted MeCN Solvate Electrolytes

Li-Li symmetric cells with solvate and solvate:HFE mixtures were tested by galvanostatic cycling to investigate the cycling stability of the Li metal anodes (**Figure 2.13**). The voltage profile of the Li-Li symmetric cell with HFE-free neat solvate exhibits unstable plating/stripping behavior resulting in cell death after few cycles, possibly due to the high viscosity of the electrolyte (**Table 2.3**). High viscosity of the electrolyte hinders facile Li^+ ion transport causing irreversible Li plating/stripping.⁵⁹⁻⁶⁰ Likely, the quick capacity fading of the Li-S cell with $(\text{MeCN})_2\text{-LiTFSI}$ (**Figure 2.2**) can be attributed to the unfavorable Li plating/stripping at the anode. **Figure 2.13** show that the HFE-added solvate electrolytes also exhibit unstable voltage hysteresis for the first few cycles but the Li-Li plating/stripping behavior becomes more stable upon extended cycling. The TTE and BTFE cells, however, exhibit similar Li-Li plating/stripping behavior, but very different Li-S cycling behavior. **Figure 2.2** shows that the discharge capacity of the Li-S cell incorporating BTFE faded much more quickly than that incorporating TTE. Therefore, the effect of the electrolyte on the cycling performance must be more complicated than the effect of the electrolyte on the stability of the anode. The presence of higher free MeCN in TTE and OTE-diluted solvate solutions might imply poor stability of the Li anode affecting the Li plating/stripping efficiency. The Li plating/stripping behavior in TTE and OTE solvents, however, was similar or slightly better than that observed in other two cosolvents.

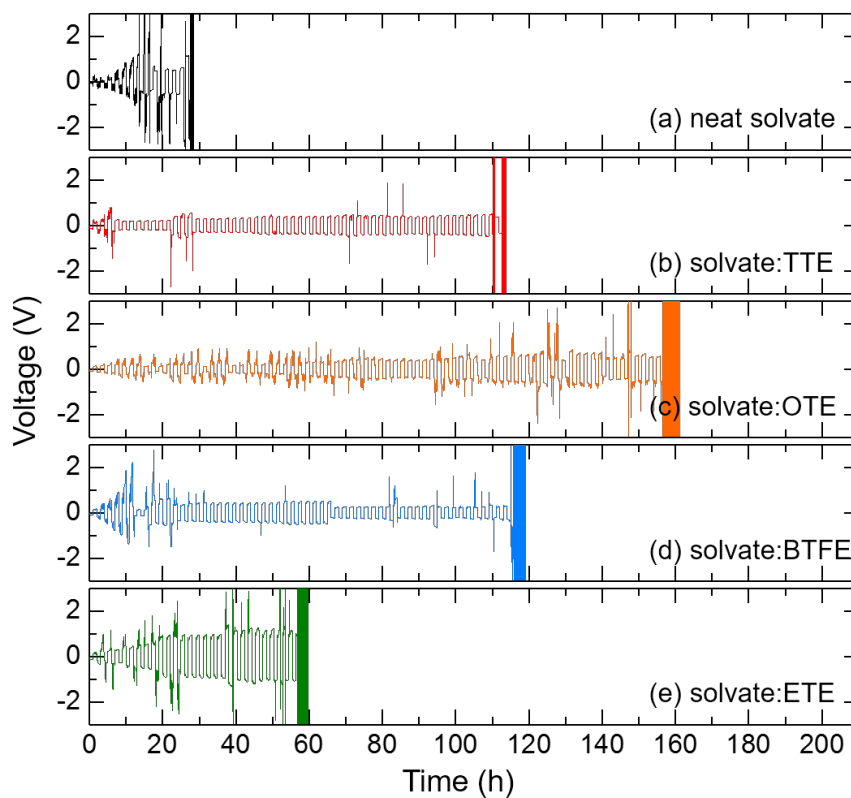


Figure 2.13 Voltage profiles showing galvanostatic cycling of Li metal plating/stripping at 0.5 mA cm^{-2} in symmetric Li-Li cells with (a) neat $(\text{MeCN})_2\text{-LiTFSI}$ solvate, (b) solvate:TTE (2:1), (c) solvate:OTE (2:1), (d) solvate:BTFE (2:1), and (e) solvate:ETE (2:1) electrolytes. The amount of Li cycled was 0.5 mAh cm^{-2} per cycle.

In fact, HFE competes with MeCN for Li^+ coordination and the exchange between HFE and MeCN is in dynamic equilibrium.²⁵ Consequently, this “free” MeCN may not react with Li metal directly. In addition, as suggested in previous work, TFSI⁻ anions are preferentially decomposed on Li metal to form a TFSI-derived SEI layer.^{22, 61} This SEI is believed to inhibit the decomposition of free MeCN.^{22, 61} Therefore, the amount of “free” MeCN alone doesn’t determine anode stability.

Another possible origin of variations in the Li-S cell cycling data as different HFEs are added to the electrolyte are changes in lithium polysulfide solubility. Previous work using (MeCN)₂-LiTFSI:TTE electrolyte showed that delicate control of the polysulfide solubility by temperature affects the redox kinetics and therefore changes the S₈ reaction pathway.²⁷ The use of different HFEs could also dictate the polysulfide solubility resulting in different cycling capability. Therefore, evaluating the polysulfide solubility in different HFE systems is important as a major function of the solvate electrolyte with HFE cosolvent is to control this solubility in the Li-S battery.

As reported previously, the solubility of lithium polysulfides in the TTE solvent is low making it difficult to measure using titration.²¹ Alternatively, the electrolyte solutions saturated with solid “Li₂S₈” prepared by evaporating the solvent from a solution of Li₂S and S₈ at the corresponding ratio may be analyzed qualitatively using UV-Vis spectroscopy. In addition, the room temperature solubility of polysulfides is too low to probe with UV-Vis spectrometer.²⁷ Therefore, the “Li₂S₈”-saturated solution was prepared at 70 °C to promote the dissolution. **Figure 2.14a** shows a photograph of solvate:HFE (2:1) solutions saturated with “Li₂S₈” and **Figure 2.14b** shows the corresponding the UV-Vis spectra of each solution. In **Figure 2.14b**, the absorbance at ~420 nm is due to the presence of S₄²⁻ in the solution.^{14, 62-63} Additional absorbance

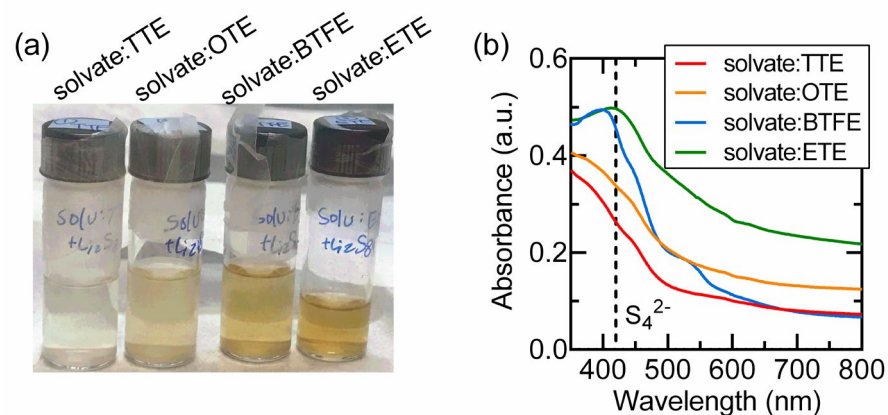


Figure 2.14 (a) Photograph showing solvate:HFE (2:1) solutions saturated with “Li₂S₈” and (b) the corresponding UV-Vis spectra.

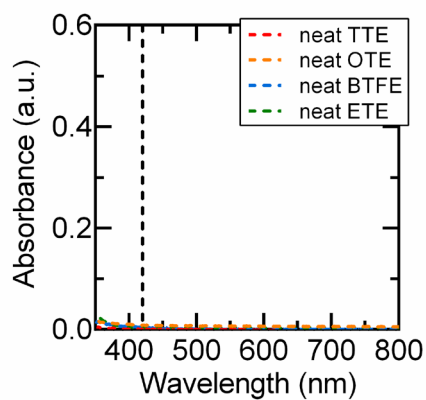


Figure 2.15 UV-vis spectra of HFE-only solutions saturated with “Li₂S₈”.

over a relatively wide wavelength range is also observed and can be attributed to the presence of various polysulfide species that are expected due to disproportionation reactions and complex equilibria of several polysulfide species in solution.²⁰ The intensity of the absorption band at 420 nm is larger in BTFE and ETE added solvates, suggesting higher polysulfide solubility in these solutions. The absorbance is negligible in neat HFE solutions saturated with “Li₂S₈” (**Figure 2.15**), suggesting the solution structure of the solvate electrolyte and its equilibrium with lithium polysulfides affects polysulfide solubility. Interestingly, the higher free or uncoordinated MeCN in TTE and OTE added solutions does not necessarily translate into higher solubility of polysulfides, as the addition of lithium polysulfides to the (MeCN)₂-LiTFSI likely changes the equilibrium between Li⁺, TFSI⁻ anion, and solvent molecules. The change in Li⁺ solvation structure as a result of lithium polysulfide addition will not be discussed here.

To understand the effect of polysulfide solubility in (MeCN)₂-LiTFSI:HFE electrolytes on electrochemical performance of the Li-S cells, the chemical composition of the SEI layer on Li metal anodes was analyzed by XPS spectroscopy. **Figure 2.16** shows S 2p XPS spectra obtained from Li metal anodes cycled in solvate:HFE (2:1) electrolyte. S 2p XPS exhibits a 2p_{3/2} and 2p_{1/2} doublet. The spectra in **Figure 2.16** are fit with this doublet maintaining the 2:1 area ratio, the 1.18 eV energy difference, and equal FWHM between the doublet pairs. Only the binding energy of the high intensity 2p_{3/2} component will be described hereafter. In **Figure 2.16b–d**, the S 2p region is best fit with four different S binding energies, while in **Figure 2.16a**, three different binding energies are found. The two S 2p_{3/2} peaks at 169.0 eV and 167.1 eV represent products of LiTFSI salt decomposition, corresponding to the sulfone group (R-SO₂-R') of the TFSI⁻ anion and sulfite (SO₃²⁻), respectively.⁶⁴⁻⁶⁶ These R-SO₂-R' and SO₃²⁻ species are present in all HFEs tested. The additional peak at 165.8 eV representing S₂O₆²⁻ is

observed in Li anodes cycled in solvate:TTE electrolyte.⁶⁷⁻⁶⁸ The additional S 2p_{3/2} peaks in the lower binding energy regime (<165 eV) are associated with bridging sulfur (S_B^0) and terminal sulfur (S_T^{-1}) of lithium polysulfides.^{34, 64, 69}

Figure 2.16 shows the intensity of the polysulfide related peaks (S_B^0 and S_T^{-1}) in the lower binding energy region (more reduced S) is larger in Li-S cells incorporating BTFE and ETE electrolytes relative to that found with TTE and OTE. The origin of this behavior likely relates to the relatively higher polysulfide solubility in BTFE and ETE solutions. This greater solubility likely enhances the crossover of polysulfide species generated at the S cathode to the Li anode side. The enhanced crossover results in a loss of sulfur active materials and increased interfacial resistance to Li^+ ion diffusion.⁸ The BTFE and ETE-added solutions exhibit higher polysulfide concentration and increased crossover, however, we note that the Coulombic efficiency in these electrolytes are close to 100% indicating that the polysulfide shuttle is effectively suppressed. Although shuttle effect is suppressed, even trace amount of polysulfides in BTFE and ETE solutions can migrate to Li anode causing side reactions and degrading the Li anode. The increased presence of polysulfides on the Li anode, especially with BTFE and ETE additives, is consistent with the decreased performance of the Li-S battery in the presence of these additives, relative to what is found with TTE and OTE.

While the two low binding energy S 2p XPS peaks are apparently diagnostic for the presence of side products on the anode, the high energy peaks can arise as a consequence of electrolyte decomposition following emersion and appear less diagnostic of anode behavior.

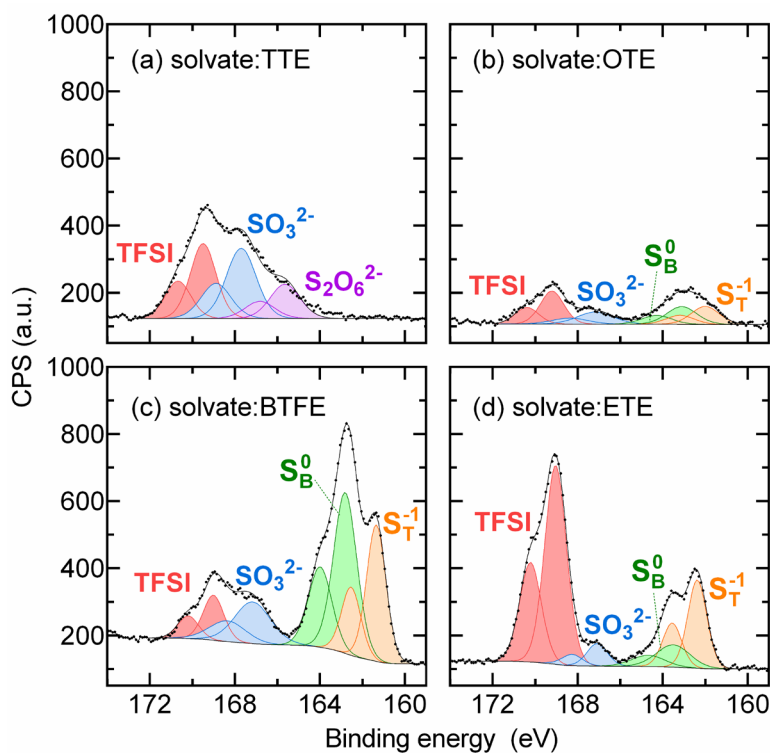


Figure 2.16 XPS analysis of SEI layer on Li metal anodes formed after 100 cycle Li–S galvanostatic cycling experiment in (a) solvate:TTE (2:1), (b) solvate:OTE (2:1), (c) solvate:BTFE (2:1), and (d) solvate:ETE (2:1) electrolytes. The S 2p XPS spectra are shown including peak fitting and assignments: TFSI ($\text{R-SO}_2\text{-R}'$) (red), SO_3^{2-} (blue), $\text{S}_2\text{O}_6^{2-}$ (purple), bridging sulfur S_B^0 (green), and terminal sulfur S_T^{-1} (orange).

2.4 Conclusion

The results reported above show that adding TTE and OTE cosolvents to the (MeCN)₂-LiTFSI solvate electrolyte results in better cell cyclability relative to the case where either BTFE or ETE is added. Raman, NMR, AIMD/QC calculation, polysulfide solubility, and XPS measurements provide insight into the origins of the performance difference from both the perspective of the local solvation structure of the Li⁺ in the electrolyte and the interfacial effects at the electrodes.

The two cosolvents that exhibit better cycling behavior, TTE and OTE, are also shown to more significantly affect the local solvation structure of the Li⁺ in the (MeCN)₂-LiTFSI solvate electrolyte. Raman and NMR spectroscopy coupled with AIMD simulations show that the addition of TTE and OTE to the (MeCN)₂-LiTFSI solvate modifies the Li⁺ solvation shell resulting in free MeCN in solution. By way of contrast, these spectroscopies show that less free MeCN is present in the (MeCN)₂-LiTFSI electrolyte diluted with BTFE or ETE. The type of HFE cosolvent allow us to tune the interaction of the HFE with the Li⁺ resulting in various degrees of MeCN removal from the first solvation sphere. This interaction is related to the degree of fluorination with the more fluorinated HFEs interacting more strongly and creating a higher free MeCN content. Previous work suggests the formation of free MeCN facilitates S₈ reduction/oxidation kinetics by enhancing the rate of polysulfide intermediate formation at the electrolyte/S₈ interface.²⁵ With a more limited presence of MeCN, S₈ redox reaction would have to proceed via a solid-state reaction, the rates of which are known to be substantially slower. The enhanced redox kinetics at the cathode likely results in improved cyclic capability of the Li-S battery with TTE and OTE cosolvents.

Importantly, we note that the electrolytes with higher free MeCN contents resulting from TTE and OTE addition do not show increased lithium polysulfide solubility in the bulk electrolyte. Thus, the properties of the bulk electrolyte are still controlled by the majority phase, i.e., the HFE with high degrees of fluorination decreasing the solubility of polysulfides. This low solubility likely limits the diffusion of polysulfides away from the cathode resulting in better cycling performance.²⁵ Indeed, XPS shows the presence of fewer polysulfide byproducts on Li anodes cycled from TTE and OTE-containing electrolytes relative to those with BTFE and ETE.

In summary, the origin of the enhanced cyclability of TTE and OTE-containing solvate electrolytes results from the interplay of many aspects in Li-S battery chemistry. Addition of TTE and OTE to the solvate electrolyte leads to simultaneously more free MeCN and reduced polysulfide solubility suggesting that we can decouple interfacial effects at the cathode with the properties of the bulk electrolyte. The free MeCN enhances reactivity at the cathode, while the reduced polysulfide solubility leads to a cleaner anode, diminished loss of active sulfur materials, and ultimately enhanced cycling performance.

2.5 References

- (1) Bruce, P. G.; Freunberger, S. A.; Hardwick, L. J.; Tarascon, J. M. *Nat. Mater.* **2012**, *11*, 19-29.
- (2) Armand, M.; Tarascon, J. M. *Nature* **2008**, *451*, 652-657.
- (3) Su, Y. S.; Fu, Y. Z.; Cochell, T.; Manthiram, A. *Nat. Commun.* **2013**, *4*, 2985.
- (4) Lowe, M. A.; Gao, J.; Abruña, H. D. *RSC Adv.* **2014**, *4*, 18347-18353.
- (5) Patel, M. U. M.; Demir-Cakan, R.; Morcrette, M.; Tarascon, J.-M.; Gaberscek, M.; Dominko, R. *ChemSusChem* **2013**, *6*, 1177-1181.

- (6) See, K. A.; Leskes, M.; Griffin, J. M.; Britto, S.; Matthews, P. D.; Emly, A.; Van der Ven, A.; Wright, D. S.; Morris, A. J.; Grey, C. P.; Seshadri, R. *J. Am. Chem. Soc.* **2014**, *136*, 16368-16377.
- (7) Busche, M. R.; Adelhelm, P.; Sommer, H.; Schneider, H.; Leitner, K.; Janek, J. *J. Power Sources* **2014**, *259*, 289-299.
- (8) Mikhaylik, Y. V.; Akridge, J. R. *J. Electrochem. Soc.* **2004**, *151*, A1969-A1976.
- (9) Ji, X. L.; Lee, K. T.; Nazar, L. F. *Nat. Mater.* **2009**, *8*, 500-506.
- (10) Ji, L. W.; Rao, M. M.; Zheng, H. M.; Zhang, L.; Li, Y. C.; Duan, W. H.; Guo, J. H.; Cairns, E. J.; Zhang, Y. G. *J. Am. Chem. Soc.* **2011**, *133*, 18522-18525.
- (11) Zheng, G. Y.; Yang, Y.; Cha, J. J.; Hong, S. S.; Cui, Y. *Nano Lett.* **2011**, *11*, 4462-4467.
- (12) Ma, G. Q.; Wen, Z. Y.; Wu, M. F.; Shen, C.; Wang, Q. S.; Jin, J.; Wu, X. W. *Chem. Commun.* **2014**, *50*, 14209-14212.
- (13) Zhang, S. S. *Electrochim. Acta* **2012**, *70*, 344-348.
- (14) Wu, H.-L.; Shin, M.; Liu, Y.-M.; See, K. A.; Gewirth, A. A. *Nano Energy* **2017**, *32*, 50-58.
- (15) Lin, Z.; Liu, Z. C.; Fu, W. J.; Dudney, N. J.; Liang, C. D. *Adv. Funct. Mater.* **2013**, *23*, 1064-1069.
- (16) Azimi, N.; Xue, Z.; Bloom, I.; Gordin, M. L.; Wang, D. H.; Daniel, T.; Takoudis, C.; Zhang, Z. C. *ACS Appl. Mater. Interfaces* **2015**, *7*, 9169-9177.
- (17) Park, J.-W.; Ueno, K.; Tachikawa, N.; Dokko, K.; Watanabe, M. *J. Phys. Chem. C* **2013**, *117*, 20531-20541.
- (18) Shin, E. S.; Kim, K.; Oh, S. H.; Cho, W. I. *Chem. Commun.* **2013**, *49*, 2004-2006.
- (19) Suo, L.; Hu, Y. S.; Li, H.; Armand, M.; Chen, L. *Nat. Commun.* **2013**, *4*, 1481.

- (20) Dokko, K.; Tachikawa, N.; Yamauchi, K.; Tsuchiya, M.; Yamazaki, A.; Takashima, E.; Park, J. W.; Ueno, K.; Seki, S.; Serizawa, N.; Watanabe, M. *J. Electrochem. Soc.* **2013**, *160*, A1304-A1310.
- (21) Cuisinier, M.; Cabelguen, P. E.; Adams, B. D.; Garsuch, A.; Balasubramanian, M.; Nazar, L. F. *Energy Environ. Sci.* **2014**, *7*, 2697-2705.
- (22) Yamada, Y.; Furukawa, K.; Sodeyama, K.; Kikuchi, K.; Yaegashi, M.; Tateyama, Y.; Yamada, A. *J. Am. Chem. Soc.* **2014**, *136*, 5039-5046.
- (23) Yamada, Y.; Yamada, A. *J. Electrochem. Soc.* **2015**, *162*, A2406-A2423.
- (24) Ueno, K.; Yoshida, K.; Tsuchiya, M.; Tachikawa, N.; Dokko, K.; Watanabe, M. *J. Phys. Chem. B* **2012**, *116*, 11323-11331.
- (25) See, K. A.; Wu, H. L.; Lau, K. C.; Shin, M.; Cheng, L.; Balasubramanian, M.; Gallagher, K. G.; Curtiss, L. A.; Gewirth, A. A. *ACS Appl. Mater. Interfaces* **2016**, *8*, 34360-34371.
- (26) Cheng, L.; Curtiss, L. A.; Zavadil, K. R.; Gewirth, A. A.; Shao, Y.; Gallagher, K. G. *ACS Energy Lett.* **2016**, *1*, 503-509.
- (27) Lee, C.-W.; Pang, Q.; Ha, S.; Cheng, L.; Han, S.-D.; Zavadil, K. R.; Gallagher, K. G.; Nazar, L. F.; Balasubramanian, M. *ACS Cent. Sci.* **2017**, *3*, 605-613.
- (28) Azimi, N.; Weng, W.; Takoudis, C.; Zhang, Z. *Electrochem. Commun.* **2013**, *37*, 96-99.
- (29) Azimi, N.; Xue, Z.; Rago, N. D.; Takoudis, C.; Gordin, M. L.; Song, J.; Wang, D.; Zhang, Z. *J. Electrochem. Soc.* **2014**, *162*, A64-A68.
- (30) Gordin, M. L.; Dai, F.; Chen, S. R.; Xu, T.; Song, J. X.; Tang, D. H.; Azimi, N.; Zhang, Z. C.; Wang, D. H. *ACS Appl. Mater. Interfaces* **2014**, *6*, 8006-8010.
- (31) Chen, S.; Yu, Z.; Gordin, M. L.; Yi, R.; Song, J.; Wang, D. *ACS Appl. Mater. Interfaces* **2017**, *9*, 6959-6966.

- (32) Gu, S.; Qian, R.; Jin, J.; Wang, Q.; Guo, J.; Zhang, S.; Zhuo, S.; Wen, Z. *Phys. Chem. Chem. Phys.* **2016**, *18*, 29293-29299.
- (33) Lu, H.; Zhang, K.; Yuan, Y.; Qin, F.; Zhang, Z.; Lai, Y.; Liu, Y. *Electrochim. Acta* **2015**, *161*, 55-62.
- (34) Zu, C.; Azimi, N.; Zhang, Z.; Manthiram, A. *J. Mater. Chem. A* **2015**, *3*, 14864-14870.
- (35) Sang, L.; Haasch, R. T.; Gewirth, A. A.; Nuzzo, R. G. *Chem. Mater.* **2017**, *29*, 3029-3037.
- (36) Wu, H.-L.; Huff, L. A.; Gewirth, A. A. *ACS Appl. Mater. Interfaces* **2015**, *7*, 1709-1719.
- (37) Kresse, G.; Furthmüller, J. *Phys. Rev. B* **1996**, *54*, 11169-11186.
- (38) Kresse, G.; Joubert, D. *Phys. Rev. B* **1999**, *59*, 1758-1775.
- (39) Perdew, J. P.; Burke, K.; Ernzerhof, M. *Phys. Rev. Lett.* **1996**, *77*, 3865-3868.
- (40) Harl, J.; Schimka, L.; Kresse, G. *Phys. Rev. B* **2010**, *81*, 115126.
- (41) Hoover, W. G. *Phys. Rev. A* **1985**, *31*, 1695-1697.
- (42) Frisch, M. J.; Trucks, G. W.; Schlegel, H. B.; Scuseria, G. E.; Robb, M. A.; Cheeseman, J. R.; Scalmani, G.; Barone, V.; Mennucci, B.; Petersson, G. A.; Nakatsuji, H.; Caricato, M.; Li, X.; Hratchian, H. P.; Izmaylov, A. F.; Bloino, J.; Zheng, G.; Sonnenberg, J. L.; Hada, M.; Ehara, M.; Toyota, K.; Fukuda, R.; Hasegawa, J.; Ishida, M.; Nakajima, T.; Honda, Y.; Kitao, O.; Nakai, H.; Vreven, T.; Montgomery, J. A., Jr.; Peralta, J. E.; Ogliaro, F.; Bearpark, M.; Heyd, J. J.; Brothers, E.; Kudin, K. N.; Staroverov, V. N.; Kobayashi, R.; Normand, J.; Raghavachari, K.; Rendell, A.; Burant, J. C.; Iyengar, S. S.; Tomasi, J.; Cossi, M.; Rega, N.; Millam, J. M.; Klene, M.; Knox, J. E.; Cross, J. B.; Bakken, V.; Adamo, C.; Jaramillo, J.; Gomperts, R.; Stratmann, R. E.; Yazyev, O.; Austin, A. J.; Cammi, R.; Pomelli, C.; Ochterski, J. W.; Martin, R. L.; Morokuma, K.;

- Zakrzewski, V. G.; Voth, G. A.; Salvador, P.; Dannenberg, J. J.; Dapprich, S.; Daniels, A. D.; Farkas, O.; Foresman, J. B.; Ortiz, J. V.; Cioslowski, J.; Fox, D. J., *Gaussian 09, Revision E.01*. Gaussian, Inc.: Wallingford, CT, 2009.
- (43) Chai, J.-D.; Head-Gordon, M. *Phys. Chem. Chem. Phys.* **2008**, *10*, 6615-6620.
- (44) Barone, V.; Cossi, M. *J. Phys. Chem. A* **1998**, *102*, 1995-2001.
- (45) Seo, D. M.; Borodin, O.; Han, S. D.; Boyle, P. D.; Henderson, W. A. *J. Electrochem. Soc.* **2012**, *159*, A1489-A1500.
- (46) Brouillette, D.; Irish, D. E.; Taylor, N. J.; Perron, G. r.; Odziemkowski, M.; Desnoyers, J. E. *Phys. Chem. Chem. Phys.* **2002**, *4*, 6063-6071.
- (47) Seo, D. M.; Boyle, P. D.; Sommer, R. D.; Daubert, J. S.; Borodin, O.; Henderson, W. A. *J. Phys. Chem. B* **2014**, *118*, 13601-13608.
- (48) Fujii, K.; Fujimori, T.; Takamuku, T.; Kanzaki, R.; Umebayashi, Y.; Ishiguro, S. I. *J. Phys. Chem. B* **2006**, *110*, 8179-8183.
- (49) Rey, I.; Johansson, P.; Lindgren, J.; Lassegues, J. C.; Grondin, J.; Servant, L. *J. Phys. Chem. A* **1998**, *102*, 3249-3258.
- (50) Saito, S.; Watanabe, H.; Ueno, K.; Mandai, T.; Seki, S.; Tsuzuki, S.; Kameda, Y.; Dokko, K.; Watanabe, M.; Umebayashi, Y. *J. Phys. Chem. B* **2016**, *120*, 3378-3387.
- (51) Reimers, J. R.; Hall, L. E. *J. Am. Chem. Soc.* **1999**, *121*, 3730-3744.
- (52) Pace, E. L.; Noe, L. J. *J. Chem. Phys.* **1968**, *49*, 5317-5325.
- (53) Barthel, J.; Buchner, R.; Wismeth, E. *J. Solution Chem.* **2000**, *29*, 937-954.
- (54) Bloembergen, N.; Purcell, E. M.; Pound, R. V. *Phys. Rev.* **1948**, *73*, 679-712.
- (55) Bayley, P. M.; Best, A. S.; MacFarlane, D. R.; Forsyth, M. *Phys. Chem. Chem. Phys.* **2011**, *13*, 4632-4640.

- (56) Hayamizu, K.; Tsuzuki, S.; Seki, S.; Ohno, Y.; Miyashiro, H.; Kobayashi, Y. *J. Phys. Chem. B* **2008**, *112*, 1189-1197.
- (57) Bogle, X.; Vazquez, R.; Greenbaum, S.; Cresce, A.; Xu, K. *J. Phys. Chem. Lett.* **2013**, *4*, 1664-1668.
- (58) Rupich, M. W.; Pitts, L.; Abraham, K. M. *J. Electrochem. Soc.* **1982**, *129*, 1857-1861.
- (59) Xu, K. *Chem. Rev.* **2004**, *104*, 4303-4418.
- (60) Li, N. W.; Yin, Y. X.; Li, J. Y.; Zhang, C. H.; Guo, Y. G. *Adv. Sci.* **2017**, *4*, 1600400.
- (61) Sodeyama, K.; Yamada, Y.; Aikawa, K.; Yamada, A.; Tateyama, Y. *J. Phys. Chem. C* **2014**, *118*, 14091-14097.
- (62) Barchasz, C.; Molton, F.; Duboc, C.; Lepretre, J. C.; Patoux, S.; Alloin, F. *Anal. Chem.* **2012**, *84*, 3973-3980.
- (63) Canas, N. A.; Fronczek, D. N.; Wagner, N.; Latz, A.; Friedrich, K. A. *J. Phys. Chem. C* **2014**, *118*, 12106-12114.
- (64) Nandasiri, M. I.; Camacho-Forero, L. E.; Schwarz, A. M.; Shutthanandan, V.; Thevuthasan, S.; Balbuena, P. B.; Mueller, K. T.; Murugesan, V. *Chem. Mater.* **2017**, *29*, 4728-4737.
- (65) Busche, M. R.; Drossel, T.; Leichtweiss, T.; Weber, D. A.; Falk, M.; Schneider, M.; Reich, M. L.; Sommer, H.; Adelhelm, P.; Janek, J. *Nat. Chem.* **2016**, *8*, 426-434.
- (66) Li, W.; Yao, H.; Yan, K.; Zheng, G.; Liang, Z.; Chiang, Y.-M.; Cui, Y. *Nat. Commun.* **2015**, *6*, 7436.
- (67) Aurbach, D.; Pollak, E.; Elazari, R.; Salitra, G.; Kelley, C. S.; Affinito, J. *J. Electrochem. Soc.* **2009**, *156*, A694-A702.
- (68) Wang, L.; Liu, J.; Yuan, S.; Wang, Y.; Xia, Y. *Energy Environ. Sci.* **2016**, *9*, 224-231.

- (69) Fantauzzi, M.; Elsener, B.; Atzei, D.; Rigoldi, A.; Rossi, A. *RSC Adv.* **2015**, *5*, 75953-75963.

CHAPTER 3

Incorporating Solvate and Solid Electrolytes for All-Solid-State Li_2S Batteries with High Capacity and Long Cycle Life

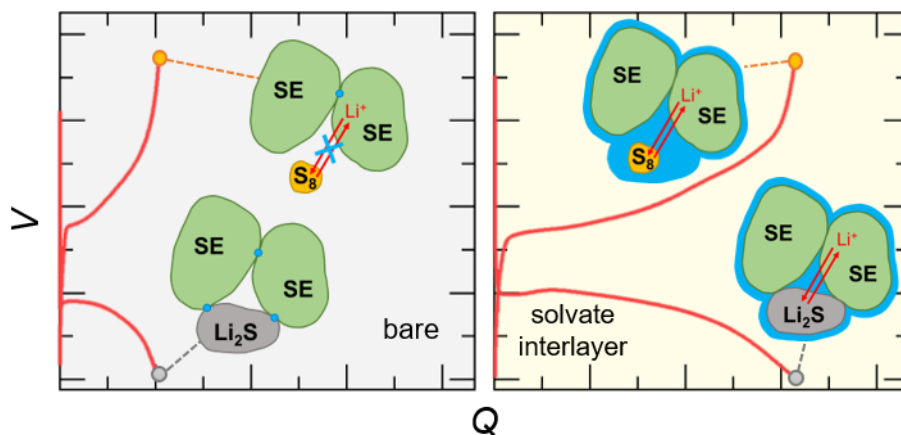


Figure 3.1 Cartoon depicting the role of solvate electrolyte in achieving high performance all-solid-state Li_2S batteries.

3.1 Introduction

All-solid-state lithium metal batteries are considered a promising technology for next-generation batteries, due to their enhanced safety and higher energy density compared to the conventional Li ion battery.¹⁻² Using S_8 or Li_2S as an active cathode material to achieve all-solid-state lithium-sulfur battery (ASSLSB) provides additional benefits when combined with inorganic solid electrolytes. S_8 and Li_2S deliver a theoretical capacity of 1672 mAh g^{-1} and 1167 mAh g^{-1} respectively, both of which are much greater than the capacity of intercalation materials ($\sim 300 \text{ mAh g}^{-1}$) used in the Li ion battery.³⁻⁴ More importantly, the energy efficiency of

ASSLSB system is improved by eliminating the well-known polysulfide shuttle, since the dissolution of polysulfide intermediates is limited.⁵

Despite these advantages, development of ASSLSB is hindered by two major issues. First, the low ionic and electronic conductivity of S₈ and Li₂S results in poor battery performance in terms of active material utilization and rate capability.⁶ Unlike the case with liquid electrolyte where Li⁺ ion conduction within the cathode is enabled by electrolyte wetting, achieving favorable Li⁺ conduction in solid-state battery cathodes is difficult since solid electrolytes are not infiltrative. In order to address this issue, ASSLSBs typically utilize a composite cathode with uniform distribution of active material, carbon, and solid electrolyte (SE) to form a nanoscale ionic/electronic conducting matrix. Considerable research focuses on building a triple-phase conducting network between all three components by mechanical ball-milling⁷⁻¹⁰, gas phase mixing¹¹⁻¹², and bottom-up synthesis of nanocomposites¹³⁻¹⁵. These cathode composites, however, necessitate incorporation of significant amounts of solid electrolytes (ca. 50 wt%) to ensure Li⁺ ion conductivity, which compromises the active material loading.

Another challenge to development of ASSLSBs originates from the large volume change (79%) the cathode experiences during battery cycling.¹⁶ The repeated lithiation and delithiation lead to crack formation within the cathode, which can potentially disrupt Li⁺ ion diffusion into the cathode.¹⁷ In the case of liquid electrolyte-based Li–S cells, the Li⁺ conduction pathway may be maintained as liquid electrolyte permeates into cracks and void spaces of the cathode. The detrimental effect from cathode volume change is more pronounced in ASSLSBs, since the rigid solid electrolyte layer cannot act as a buffer layer to accommodate the volume change. Significant volume contraction after Li₂S delithiation leads to a physical contact loss of active material and ionically insulated S₈. Additionally, repeated volume contraction and expansion of

the cathode inevitably induces huge stress/strain at the cathode interface decreasing the long-term mechanical stability of the battery.

Modification of the electrolyte/electrode interface with a Li^+ -conducting interfacial layer may enable high-performance ASSLSBs. From the cathode standpoint, a Li^+ -conducting layer may improve the physical contact between cathode components while accommodating the volume change (**Figure 3.2**). From the anode side, the interlayer may promote intimate contact with the Li anode while suppressing the side reactions that degrade SE materials. Prior reports employed the strategy of adding small amounts of liquid electrolyte¹⁸⁻¹⁹ or ionic liquids²⁰⁻²³ to form a solid–liquid hybrid system. These studies show that with the addition of liquid component at the electrolyte/electrode interfaces, the interfacial contact is enhanced, resulting in a stable cycling of the battery. However, stability of these liquids against Li is unclear.

The desired properties of the liquid electrolyte for solid–liquid hybrid batteries include high ionic conductivity, high thermal stability, and chemical stability towards other cell components. Despite superior ionic conductivity and wettability of the conventional 1 M ethereal or carbonate electrolytes, fundamental stability and compatibility issues arise.²⁴ In dilute solutions, most of the solvent molecules are not coordinated to the cationic center and thus the chemical stability of the solution is dictated by the reactivity of this free/uncoordinated solvent.²⁴⁻²⁵ Additionally, previous study shows that sulfide solid electrolytes decompose to form additional impurity phases in contact with the pure triglyme, suggesting poor stability of the neat solvent with respect to the solid electrolyte.²⁶ Additionally, the dilute solution exhibits poor reductive stability against Li metal due to the decomposition of free solvent.²⁵

The stability of the liquid electrolyte towards solid–liquid hybrid system can be improved by increasing the Li salt concentration to form the “solvate” electrolyte (also denoted as

superconcentrated electrolyte²⁵, sparingly solvating electrolyte²⁷, solvate ionic liquid²⁸⁻²⁹, or solvent-in-salt electrolyte³⁰⁻³¹). As the ratio between salt to solvent increases to a level where most solvent molecules are coordinated to the Li^+ center to achieve the solvate complex, only minimal amount of free solvent is present in solution. Due to the unique solution structure, the solvate electrolyte exhibits various unusual physicochemical properties such as high chemical stability, high thermal stability, and low volatility, all of which are advantageous for solid–liquid hybrid batteries.²⁴ Indeed, Oh et al. demonstrated the improved stability of Li_3PS_4 and $\text{Li}_{10}\text{GeP}_2\text{S}_{12}$ against the glyme-based solvate with lithium bis(trifluoromethane sulfonyl)imide (LiTFSI) compared to the dilute solution, which was attributed to the decreased nucleophilicity of the ethereal oxygen as a result of solvent–salt complexation.²⁶ The authors reported improved cycling performance of $\text{LiFePO}_4/\text{Li-In}$ solid-state cells with the inclusion of LiTFSI–glyme solvate in the cathode composite.²⁶ Another study using 7 M LiTFSI in 1,3-dioxolane (DOL)/1,2-dimethoxyethane (DME) with hydrofluoroether (HFE) cosolvent, 1,1,2,2-tetrafluoroethyl 2,2,3,3-tetrafluoropropyl ether (TTE), showed that Li–Li symmetric cells with solvate exhibits longer cycle life without forming dendrites whereas the bare cell without solvate shorted after few cycles.³²

The limited polysulfide solvating ability of the liquid electrolyte is another important criterion to achieve stable cycling of Li–S cells.^{29, 31, 33-34} In this context, combining solvate electrolyte and inorganic solid electrolyte to prepare the hybrid Li–S batteries will impose a synergistic effect on the battery performance in every aspects as discussed above. So far, the effect of using solvate on the operation of all-solid-state Li–S batteries has not been reported.

Herein, we propose a simple approach to enhance the interfacial contact by using the highly concentrated solvate electrolyte based on LiTFSI salt in acetonitrile (MeCN) with TTE

cosolvent, denoted as $(\text{MeCN})_2\text{-LiTFSI:TTE}$, as an interlayer material for solid-state Li-S batteries. The $(\text{MeCN})_2\text{-LiTFSI:TTE}$ was previously reported to be compatible with Li-S cells showing stable cycling performance.³³⁻³⁴ We used pre-lithiated Li_2S instead of S_8 as an active material, since the pre-expanded form (Li_2S) could provide a buffer space for volume change where ionic contact between active material and SE could be maintained even after volume contraction by virtue of the solvate interlayer (**Figure 3.2b**). We report two different methods to utilize solvate electrolyte in solid-state Li_2S batteries. First, the solvate was integrated into the solid-state cells as an interlayer between electrodes and the SE as shown in **Figure 3.2b**. Second, the solvate was premixed with SE to yield a solvate–solid electrolyte mixture (solvSEM) electrolyte. The substantial improvement in the interfacial properties with the addition of solvate enabled the excellent electrochemical performance of the solid-state and hybrid Li_2S batteries.

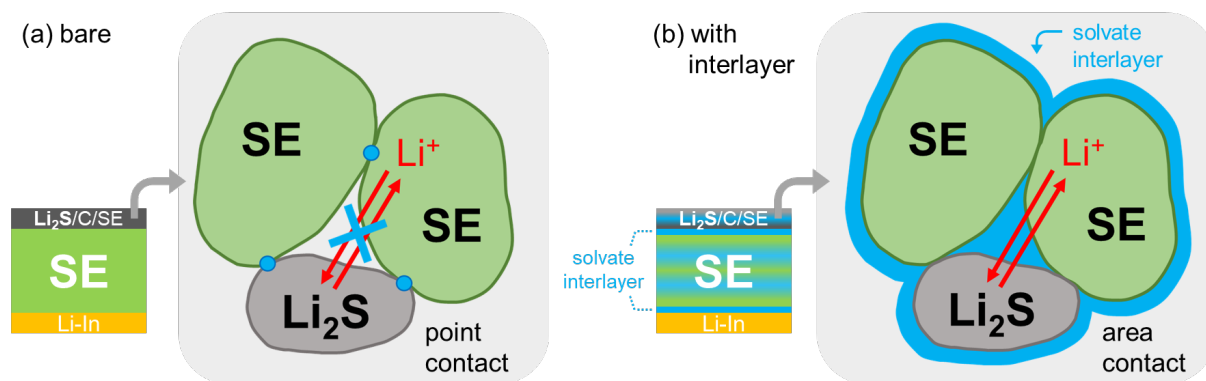


Figure 3.2 Schematic representation of the solid-state Li_2S batteries with Li-In alloy anode, LPS solid electrolyte, and Li_2S composite cathode. The composite cathode is prepared by ball-milling Li_2S , conductive carbon, and LPS. (a) shows the bare Li_2S -based cell and (b) shows the cell with the solvate interlayer.

3.2 Experimental Methods

Material Preparation: Reagent-grade Li_2S (99.98%) was purchased from Sigma Aldrich. $\text{Li}_7\text{P}_3\text{S}_{11}$ (LPS; 99.99%, MSE Supplies LLC) was used as received. The composite cathode for the solid-state Li_2S battery consisted of Li_2S , Ketjenblack, and LPS. Li_2S was prepared by ball-milling the as received Li_2S at 370 rpm for 20 h to decrease the particle size and the crystallite size (**Figure 3.3**). The material was placed in an agate mill jar (50 mL) with agate balls (3 mm and 5 mm) and sealed in an Ar-filled glovebox. Ball-milling was performed using a high energy planetary ball-mill apparatus (MSE Supplies LLC, MSE-PMV1-0.4L). The $\text{Li}_2\text{S}/\text{C}$ composite was prepared by mixing the ball-milled Li_2S and Ketjenblack (EC-600JD, AkzoNobel) at a 1:1 weight ratio at 370 rpm for 10 h in the ball-mill. The $\text{Li}_2\text{S}/\text{C}$ composite was further mixed with LPS solid electrolyte in the ball-mill at a rotation speed of 370 rpm for 4 h to form a $\text{Li}_2\text{S}/\text{C}/\text{SE}$ composite (1:1:2 wt%). The solvate electrolyte, $(\text{MeCN})_2\text{-LiTFSI}$, and its diluent were prepared as described previously.³³ A stoichiometric ratio of 2 mol MeCN (99.8%, Sigma Aldrich) and 1 mol LiTFSI (99.95%, Sigma Aldrich) were stirred overnight to yield a clear, viscous solution. The cosolvent, 1,1,2,2-tetrafluoroethyl 2,2,3,3-tetrafluoropropyl ether (TTE; 99%, Synquest Laboratories), was used to decrease the viscosity of the $(\text{MeCN})_2\text{-LiTFSI}$ solvate. The electrolyte with TTE added, denoted as $(\text{MeCN})_2\text{-LiTFSI:TTE}$, was prepared by diluting $(\text{MeCN})_2\text{-LiTFSI}$ with TTE at volume ratio of 2:1. The water content of MeCN and TTE was measured by Karl Fisher titration (Photovolt Aquatest Karl-Fischer Coulometric Titrator) and was less than 5 ppm.

Material Characterization: Scanning electron microscopy (SEM) images were collected on a Hitachi S4700 at an accelerating voltage of 15 kV. The energy dispersive X-ray spectroscopy (EDS) was performed with an Oxford Instruments ISIS elemental analysis system.

Powder X-ray diffraction (XRD) was performed on a Siemens/Bruker D-5000 equipped with Cu K α radiation. To minimize sample exposure to air during XRD measurement, the sample was placed in an airtight hermetic holder inside an Ar-filled glovebox. The Rietveld refinement was performed using Jade 9.0 software.

Solid-State and Hybrid Li₂S Cell Assembly: Solid-state Li₂S batteries were assembled using LPS, a Li-In alloy anode³⁵, and a composite cathode. LPS glass-ceramic solid electrolyte was used in the cathode composite and in the assembly of solid-state battery due to its high ionic conductivity. LPS is known to decompose in direct contact with Li metal to form side products such as Li₂S and Li₃P, impeding the Li⁺ ion transport across the interface. Li-In alloy was used as an anode in order to improve chemical and electrochemical stability at the anode/solid electrolyte interface, despite the decrease in cell voltage.³⁵ The cathode was either the Li₂S/C composite (1:1 wt%) or the Li₂S/C/SE composite (1:1:2 wt%) depending on the cell configuration. Electrochemical tests were performed on three different cell configurations (schematics shown in **Figure 3.4**). The *bare* solid-state Li₂S pellet was prepared by sequentially placing LPS powder (170 mg) and Li₂S/C/SE composite (3–4 mg) in a 13 mm die, resulting in a Li₂S loading of 0.57–0.75 mg cm⁻². The powders were pressed at 370 MPa for 5 min to produce a bilayer pellet. Subsequently, the Li-In alloy anode (Lithium; 99.9%, Sigma Aldrich, Indium; 99.99% ESPI Metals) was placed on the other side of the bilayer pellet and pressed at 120 MPa for 3 min. The Li-In anode was formed by using a thin layer of In foil (11.1 mm diameter) inserted between LPS and Li foil (7.94 mm diameter). The as-prepared three-layer pellet was sandwiched between two stainless-steel current collectors and assembled in a modified Swagelok tube apparatus (Chicago Fluid System Technologies) for electrochemical evaluation. The solid-state Li₂S pellet *with interlayer* was prepared similarly but with the addition of

(MeCN)₂-LiTFSI:TTE solvate (20 μ L) as an interlayer at both SE|cathode and SE|anode interfaces. The electrolyte/sulfur (E/S) ratio of the cell with the solvate interlayer was determined by the volume of solvate electrolyte and the mass loading of Li₂S and was calculated to be 20–26.7 μ L mg⁻¹. The relatively high E/S ratio was used to ensure proper wetting of the cathode (~4 mg) and the SE layer (170 mg).

The hybrid Li₂S cell was assembled in a CR2032 coin cell (MTI Corporation) and consisted of solvate–solid electrolyte mixture (*solvSEM*) electrolyte, Li-In alloy anode, and Li₂S/C composite cathode. First, the solvSEM electrolyte was prepared by mixing 40 wt% of (MeCN)₂-LiTFSI:TTE solvate with 60 wt% of LPS using mortar and pestle. The coin cell was assembled by first placing Li-In anode on the stainless-steel disk (15.5 mm diameter). Then solvSEM (300 mg) was spread onto the Li-In anode, followed by spreading Li₂S/C composite (5–6 mg) resulting in a Li₂S loading of 1.32–1.58 mg cm⁻². The cell was closed with a hydraulic crimping machine (MTI Corporation).

The liquid-based Li₂S battery was prepared using the Li₂S/C composite (1:1 wt%) cathode. A slurry cathode consisting of 90 wt% Li₂S/C composite and 10 wt % poly(vinylidene fluoride) (PVDF; Sigma-Aldrich) binder was mixed in anhydrous N-methyl-2-pyrrolidone (NMP; Sigma-Aldrich), resulting in a composition of Li₂S/C/PVDF (45:45:10 wt%). The slurry was drop cast onto carbon-coated Al foil (MTI Corporation) and dried overnight, yielding a Li₂S loading of 0.50 mg cm⁻². The liquid cell was assembled in a CR2032 coin cell with Li₂S/C/PVDF cathode, Li-In alloy anode, (MeCN)₂-LiTFSI:TTE solvate electrolyte (70 μ L), and a 2400 Celgard separator.

Electrochemical Measurements: Galvanostatic cycling experiments were performed on an Arbin Battery Tester (Model BT 2043, Arbin Instruments Corp.) Li₂S battery cycling was

performed with a voltage cutoff of 0.38 V and 3.38 V vs. Li-In (1 V and 4 V vs. Li/Li⁺). C rates and capacities were calculated based on the mass of Li₂S active material in the composite cathode. The rate capability test was performed after pre-cycling the cell at C/20 for 10 cycles. In order to stabilize the open circuit potential, the cells were allowed to rest for at least 12 h prior to measurements. Electrochemical impedance spectroscopy (EIS) was performed using a BioLogic SP-150 potentiostat. Impedance spectra were measured before and after cell cycling at frequencies from 1 MHz to 5 mHz with an amplitude of 30 mV. All electrochemical measurements were performed at room temperature.

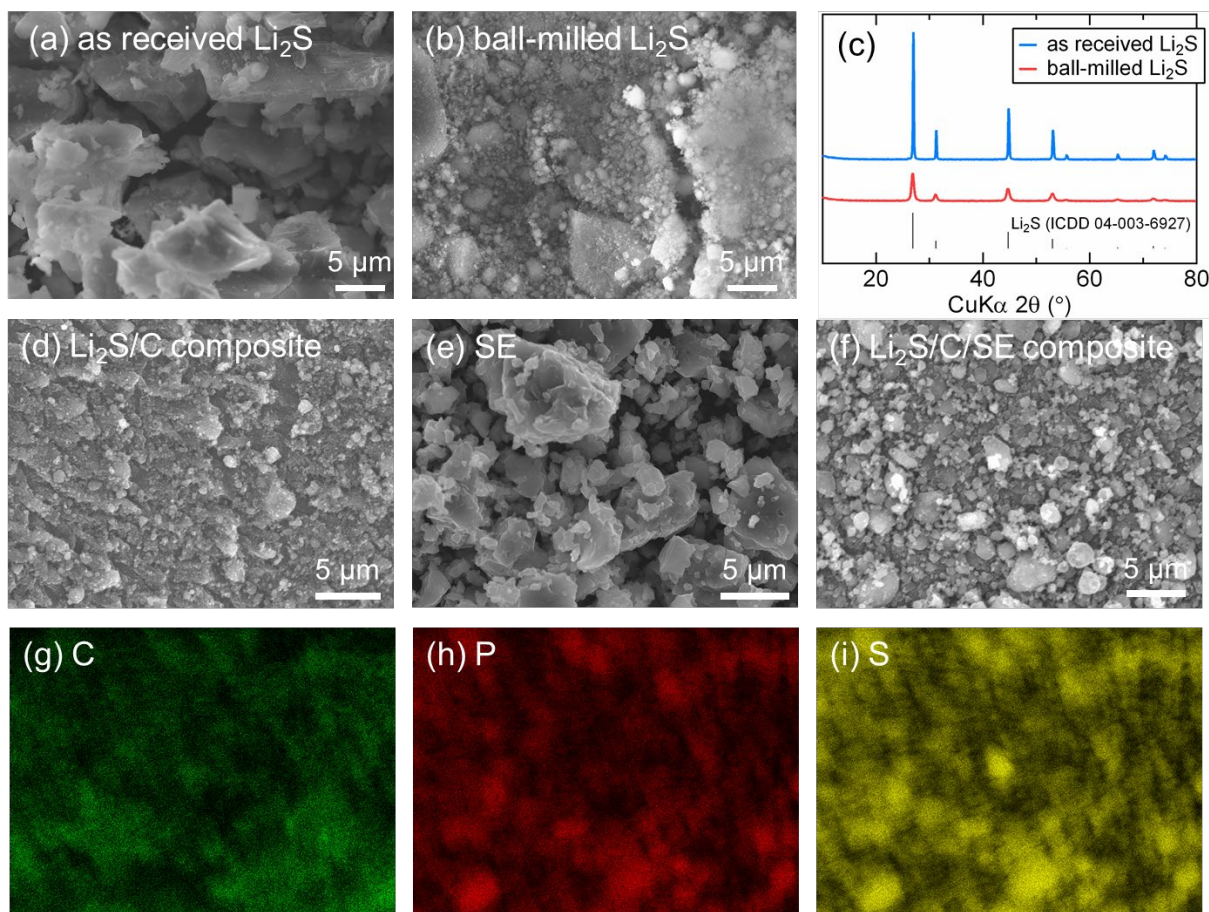


Figure 3.3 SEM image of (a) as received Li_2S and (b) ball-milled Li_2S . The decrease in particle size and significant morphological changes were observed after the ball-milling process. (c) XRD pattern of as received Li_2S and ball-milled Li_2S . The average crystallite sizes of pristine Li_2S and ball-milled Li_2S were obtained from Rietveld refinement and are 95 nm and 15 nm respectively. (d) SEM of the $\text{Li}_2\text{S}/\text{C}$ composite prepared by mixing ball-milled Li_2S with Ketjenblack. (e) SEM of the LPS solid electrolyte. (f) SEM image of the $\text{Li}_2\text{S}/\text{C}/\text{SE}$ composite and corresponding EDS mapping of (g) C, (h) P, and (i) S. The particle size and distribution pattern of LPS solid electrolyte in the composite is confirmed by P mapping, since LPS is the only source of the P signal within the composite material. The particle size of the LPS ranges from ca. 1–4 μm and LPS is embedded in the composite inhomogeneously even after extensive ball-milling.

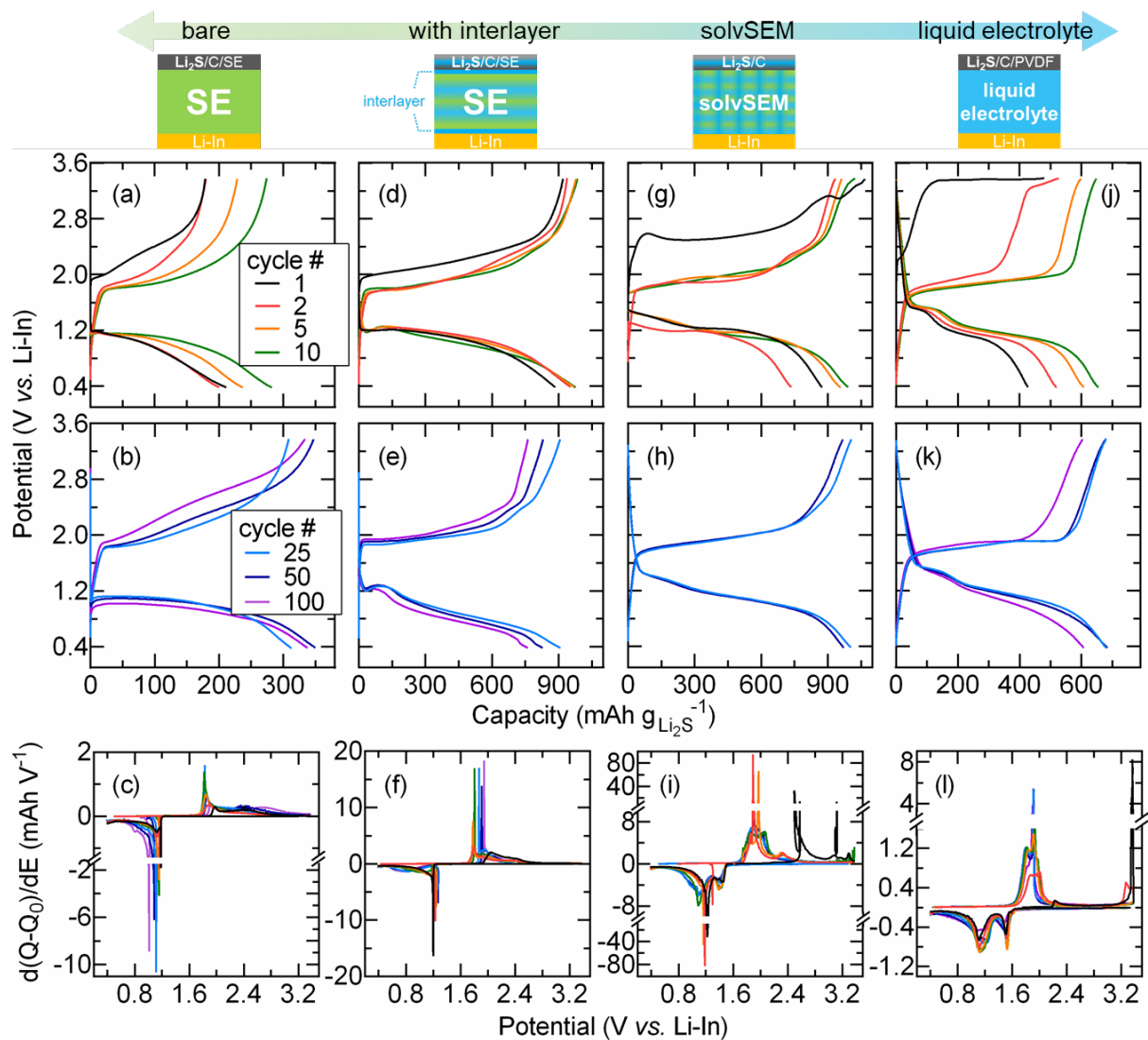


Figure 3.4 Voltage profile of the Li_2S -based battery with various electrolyte compositions and cell configurations. (a–c) bare solid-state Li_2S cell, (d–f) solid-state Li_2S cell with the solvate interlayer, (g–i) hybrid Li_2S cell with the solvSEM electrolyte, and (j–l) Li_2S cell with the liquid solvate electrolyte. The solvate electrolyte used is $(\text{MeCN})_2\text{-LiTFSI:TTE}$. The cells are cycled between 0.38 V and 3.38 V vs. Li-In (1 V and 4 V vs. Li/Li^+) at a current density of $C/10$. Galvanostatic measurements were performed at room temperature. Top panels show charge/discharge curves for cycles 1, 2, 5, and 10 and middle panels show cycles 25, 50, and 100. The corresponding differential capacity plot of the voltage profile is shown in the bottom panels.

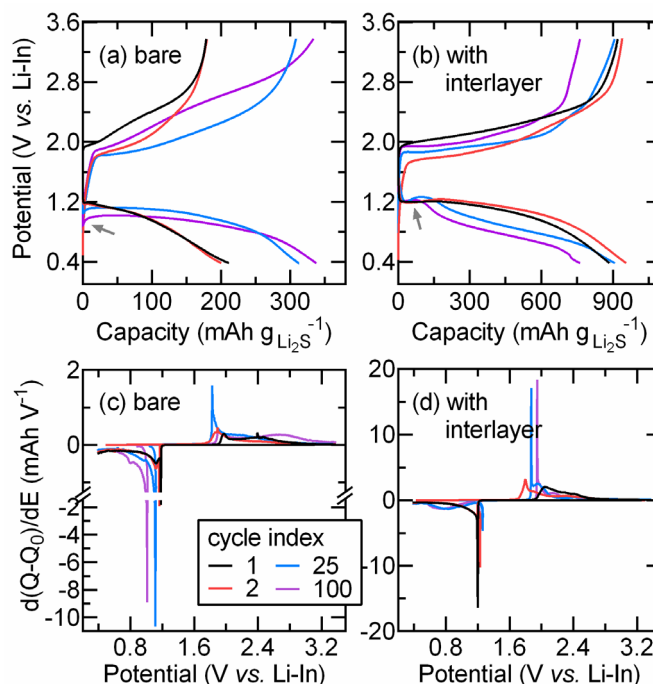


Figure 3.5 Galvanostatic cycling of the Li_2S composite cathode ($\text{Li}_2\text{S}:\text{C}:\text{SE} = 1:1:2$ wt%), Li-In alloy anode, and LPS solid electrolyte cycled with and without the presence of solvate interlayer. The cells were cycled at $C/10$. Charge and discharge curves of (a) the bare solid-state Li_2S cell and (b) the Li_2S cell with the solvate interlayer. Differential capacity curves of (c) the bare Li_2S cell and (d) the cell with the interlayer are also shown. All cells were cycled at room temperature.

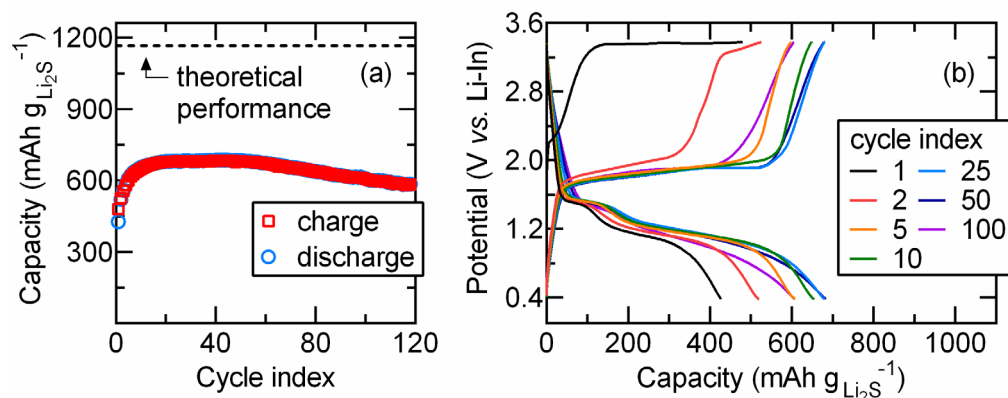


Figure 3.6 Galvanostatic battery cycling of liquid electrolyte-based Li_2S cell prepared with a Li-In alloy anode, $\text{Li}_2\text{S}/\text{C}/\text{PVDF}$ (45:45:10 wt%) cathode, and $(\text{MeCN})_2\text{-LiTFSI}:\text{TTE}$ solvate electrolyte. The cell was cycled at $C/10$. (a) specific capacity and (b) charge and discharge profiles at various cycle numbers.

3.3 Results and Discussion

3.3.1 Electrochemical Performance of Solid-State Li₂S Cells

Solid-state Li₂S batteries prepared using Li₂S/C/SE composite cathode, Li₇P₃S₁₁ (LPS) solid electrolyte, and Li-In alloy anode were examined by galvanostatic cycling experiments. **Figure 3.5a** shows the charge and discharge profile and **Figure 3.5c** shows the differential capacity curve of the bare solid-state Li₂S cell. The first charge cycle exhibits a large overpotential, which is typically observed in Li₂S-based batteries.³⁶ This behavior likely originates from the large activation barrier required to extract Li⁺ from highly crystalline Li₂S.³⁶ The overpotential decreases and eventually disappears as cycling proceeds. The voltage curve of the bare solid-state Li₂S cell displays only one plateau, consistent with previous reports.^{8, 13-14, 37-}
³⁸ In contrast, a voltage curve for a Li–S cell utilizing a liquid electrolyte exhibits two distinct discharge plateaus, representing the conversion from S₈ to high-order lithium polysulfides and then to Li₂S respectively (**Figure 3.6**).^{37, 39} The Li–S electrochemistry in the absence of solvating molecules likely follows a direct conversion between Li₂S and S₈, since the formation of soluble lithium polysulfides are hindered. The possible formation of intermediate solid-state Li₂S_n species (n = 2, 4, 6, 8) is unlikely, as evidenced by the higher formation energy of these species compared to that of Li₂S suggesting that Li₂S is the only favored solid-state phase.⁴⁰

The discharge profile of the bare Li₂S cell exhibits a well-defined plateau followed by a sloping feature. The putative solid-state conversion appears as a sharp peak in the differential capacity curve (**Figure 3.5c**), corresponding to a biphasic transformation from S₈ to Li₂S. The discharge plateau occurs at 1.2 V vs. Li-In (1.82 V vs. Li/Li⁺) for initial cycles and decreases to 1.1 V and 1.0 V vs. Li-In at cycles 25 and 100, respectively. An increase in overpotential was observed as cycle number increases, likely due to development of poor ionic contact within the

composite resulting in large cell polarization. It is interesting to note that an initial dip is observed immediately before the first plateau (demarcated with an arrow), which is associated with the polarization required to overcome a nucleation barrier to form a new phase.⁴⁰

The voltage profile and its differential capacity of the solid-state Li₂S cell with the solvate interlayer is shown in **Figure 3.5b** and **Figure 3.5d**. The 1st and 2nd cycle voltage profile of the interlayer-modified cell resembles that of the bare cell (i.e., one plateau and a sloping profile at the end), except that much larger charge/discharge capacities are delivered with the presence of solvate interlayer. This suggests the oxidation/reduction of Li₂S follows the solid-state conversion pathway without forming polysulfide intermediates. Interestingly, the discharge profile at cycles 25 and 100 is different from what is seen at cycles 1 and 2. At higher cycle numbers the discharge profile exhibits an initial dip (demarcated with an arrow) following which is a sloping feature rather than the plateau seen initially. The change in voltage profile at higher cycle numbers suggests that the electrochemical processes have changed as a result of cycling in the presence of solvate interlayer. The solvate electrolyte in the interlayer likely allows the formation of soluble polysulfide intermediates. The polysulfide solvating capability of the solvate, however, is limited since most solvent molecules are coordinated to the Li⁺ center and the amount of free solvent that can solubilize polysulfides is minimal.⁴¹ Therefore, the sloping feature at cycles 25 and 100 suggests that S₈ reduction may proceed via quasi-solid-state reaction instead of a direct solid-state conversion.^{33-34, 41-42}

Figure 3.7a shows the cycling performance of the bare Li₂S cell cycled at C/10 where capacities are calculated based on the mass of Li₂S. A gradual increase in capacity is observed during the initial 15 cycles and the capacity stabilizes at around 330 mAh g⁻¹, corresponding to 28% active material utilization based on the theoretical capacity of 1167 mAh g⁻¹ for Li₂S (black

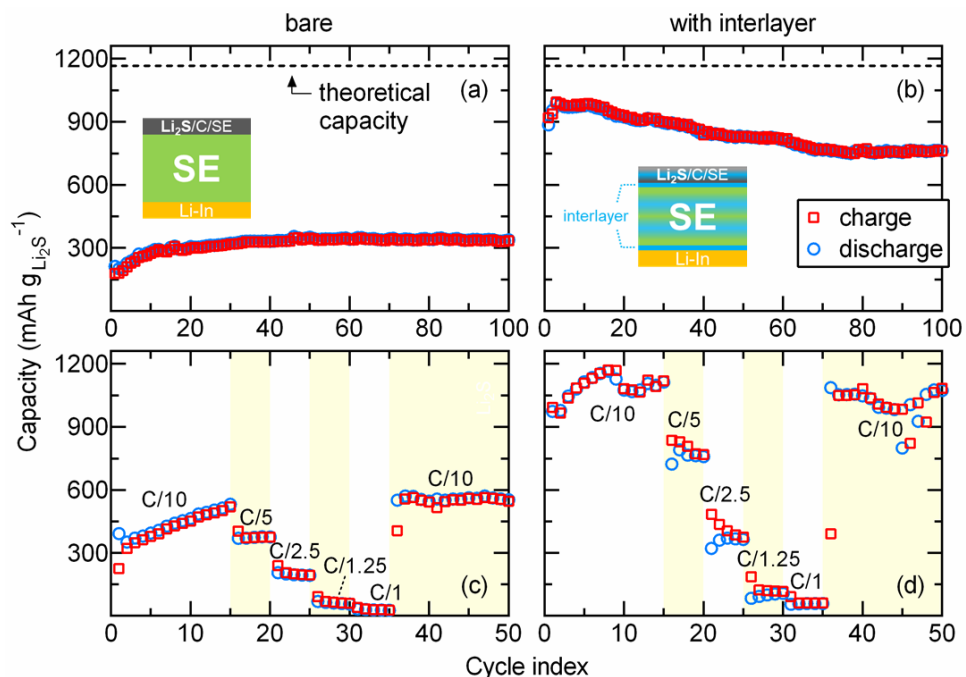


Figure 3.7 Electrochemical performance of the solid-state Li_2S batteries prepared with Li-In alloy anode, LPS solid electrolyte, and Li_2S composite cathode ($\text{Li}_2\text{S}:\text{C}:\text{SE} = 1:1:2$ wt%). (a) shows the long-term cycling of the bare Li_2S cell and (b) shows that of the interlayer-modified cell. The cells were cycled between 0.38 V and 3.38 V vs. Li-In (1 V and 4 V vs. Li/Li^+) at a current loading of C/10. C-rate dependent performance of (c) the bare Li_2S cell and (d) the cell with the solvate interlayer is shown. All cells were cycled at room temperature.

dashed line). This result indicates that 72% of Li_2S is electrochemically inactive even after extensive ball-milling to form a $\text{Li}_2\text{S}/\text{C}/\text{SE}$ composite. The low Li_2S utilization of the bare solid-state Li_2S cell is consistent with prior reports.¹³ As shown in a scanning electron microscopy (SEM) image and corresponding energy dispersive X-ray spectroscopy (EDS) mapping of the $\text{Li}_2\text{S}/\text{C}/\text{SE}$ composite (**Figure 3.3**), LPS particles are embedded throughout the entire composite but their distribution is not uniform, leaving areas with limited Li^+ ion conduction. We speculate that only those Li_2S particles in close proximity to the LPS solid electrolyte are electrochemically active with areas absent LPS exhibiting ionically insulated Li_2S particles. In addition, the SEM/EDS show that the solid–solid contact between Li_2S and LPS is incomplete (i.e., has a small contact area), thereby increasing Li^+ diffusion length and impeding charge-transfer at the interface (**Figure 3.2a** and **Figure 3.3**).

In order to form an intimate interfacial contact within the cathode and at the electrode interfaces, the solvate electrolyte was used as a wetting agent for the solid-state battery as shown in **Figure 3.2b**. **Figure 3.7b** shows the cycling performance of the solid-state Li_2S battery prepared with the solvate interlayer at both $\text{SE}|\text{cathode}$ and $\text{SE}|\text{anode}$ interfaces. The charge/discharge capacity increases for the first few cycles and reaches the maximum capacity of 990 mAh g^{-1} , corresponding to 85% active material utilization. The presence of a small amount of solvate at both the $\text{SE}|\text{cathode}$ and $\text{SE}|\text{anode}$ interfaces significantly improved the cycling performance compared to the bare solid-state cell without the solvate interlayer.

Despite the superior performance of the interlayer-modified cell, a slight decrease in capacity is observed between cycle 5 and cycle 70 and the capacity stabilizes at 760 mAh g^{-1} at cycle 100. When using solvate as a wetting agent, the presence of even small amounts of solvating molecules (i.e., free/uncoordinated MeCN in the solvate electrolyte) can lead to the

formation of intermediate polysulfides.^{33, 42} The generation of polysulfides could result in a well-known polysulfide shuttle effect, due to the crossover of polysulfides from cathode to anode.⁵ However, we note that Coulombic efficiency is 100% and is stable throughout 100 cycles, as was also found for the bare electrolyte (**Figure 3.8**), suggesting that the polysulfide shuttle is suppressed. Therefore, the hypothesis that the formation of polysulfides is the cause of capacity fading observed in **Figure 3.7b** is not likely.

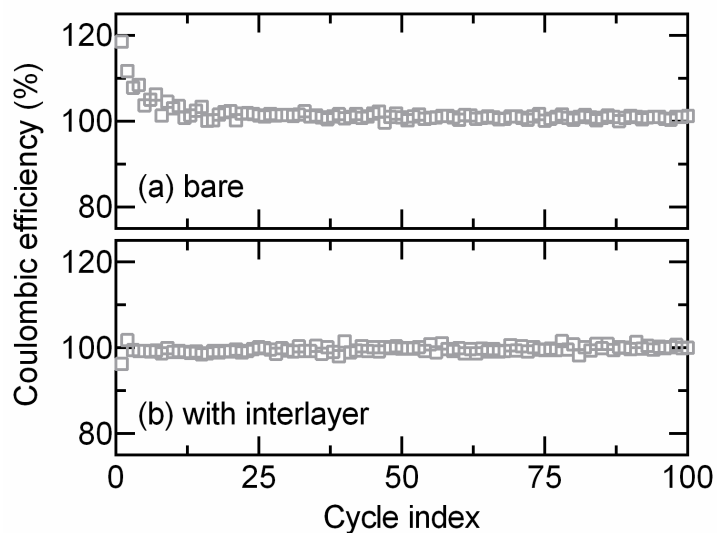


Figure 3.8 Coulombic efficiency of (a) the bare solid-state Li_2S cell, (b) the Li_2S cell with the solvate interlayer. Specific capacities are shown in **Figure 3.7a–b**. Coulombic efficiency is determined by $Q_{\text{discharge}}/Q_{\text{charge}} \times 100$.

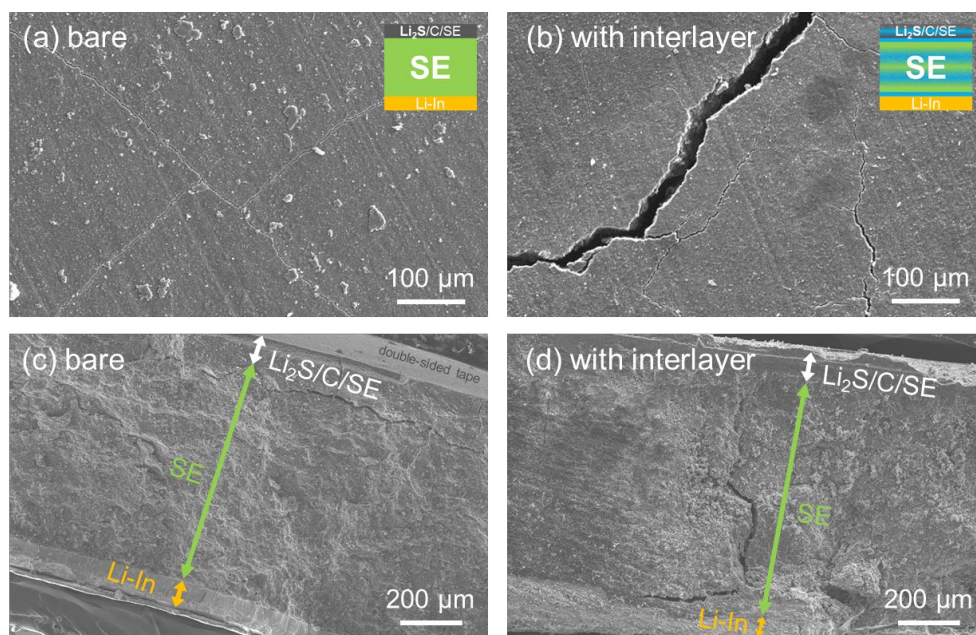


Figure 3.9 SEM surface and cross-section image of (a, c) the bare solid-state Li_2S cell and (b, d) the cell with the solvate interlayer measured after 10 cycles. (a–b) shows the surface of the Li_2S cathode and (c–d) shows the cross-section of the three-layer pellet where the formation of cracks and their propagation across the pellet is observed after 10 cycles.

A more plausible explanation for the capacity fade seen in the interlayer-protected solid electrolyte is related to huge volume change (79%) observed during delithiation and lithiation of Li_2S .¹⁶ Due to the rigid structure of SE, repeated volume contraction and expansion of the cathode results in large stress/strain at the interfaces, eventually leading to the formation of cracks. As shown in **Figure 3.9**, the formation of crack on the cathode surface and inside the SE is observed after cycling the pellet for 10 cycles for both the bare and the interlayer-modified solid-state cells. The fraction of electrochemically active Li_2S is bigger in the interlayer-modified cell which must mean that volume change experienced at the interface is larger. This larger volume change suggest that the magnitude of stress/strain experienced at the interface is greater with the incorporation of solvate interlayer. **Figure 3.9** clearly shows that the size of the crack on the cathode surface is larger when the solvate interlayer was employed. Additionally, crack propagation across the entire pellet is observed for the cell with solvate interlayer, whereas cracking was observed only near the cathode for the bare cell. The capacity fade seen in the interlayer-modified cell could be a consequence of this crack formation.

Figure 3.7c–d shows the C-rate dependent performance of the solid-state cell with and without the solvate interlayer. Increasing C-rate to C/5, C/2.5, C/1.25, and to C/1 results in a progressive capacity decrease for both the bare and interlayer cells. This capacity fading at higher C-rates fully recovers, however, when cells are cycled at C/10.

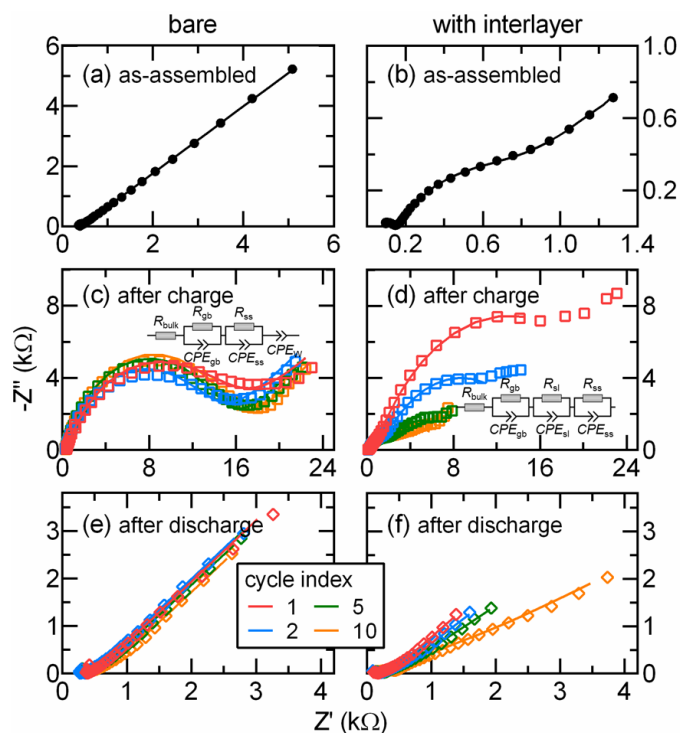


Figure 3.10 Nyquist plots of the bare solid-state Li_2S cell (left panels) and the Li_2S cell with the solvate interlayer (right panels) (a–b) before and (c–f) after cycling. Impedance spectra were collected intermittently after each charge and discharge cycle during galvanostatic cycling at $C/10$. The inset shows equivalent circuit used to model the system. The symbols represent the data and fit results are overlaid in a solid line. The resistance values from the fit are summarized in **Table 3.1** and **Table 3.2**.

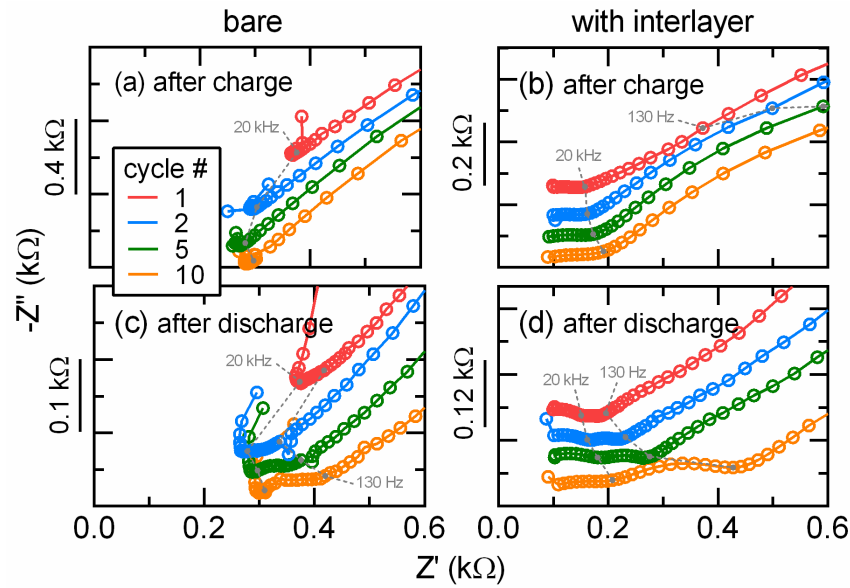


Figure 3.11 Nyquist plots of the bare solid-state Li_2S cell (left panels) and the Li_2S cell with the solvate interlayer (right panels). Impedance spectra were collected intermittently after each charge and discharge cycle during galvanostatic cycling at $C/10$. High frequency (low Z') region of **Figure 3.10** is shown. The spectra are stacked with an offset along the y-axis.

Table 3.1 Resistance values obtained by fitting the Nyquist plots shown in **Figure 3.10c, e** (bare Li_2S cell).

cycle #	bare, after charge			bare, after discharge		
	$R_{\text{bulk}} (\Omega)$	$R_{\text{gb}} (\Omega)$	$R_{\text{int}} (\Omega)$	$R_{\text{bulk}} (\Omega)$	$R_{\text{gb}} (\Omega)$	$R_{\text{int}} (\Omega)$
1	357	65	14728	368	61	69
2	287	67	13027	266	58	131
5	266	72	14260	279	91	173
10	283	80	15185	290	132	251

equivalent circuit

Table 3.2 Resistance values obtained by fitting the Nyquist plots shown in **Figure 3.10d, f** (interlayer-modified Li_2S cell).

cycle #	interlayer, after charge			interlayer, after discharge		
	$R_{\text{bulk}} (\Omega)$	$R_{\text{gb}} (\Omega)$	$R_{\text{int}} (\Omega)$	$R_{\text{bulk}} (\Omega)$	$R_{\text{gb}} (\Omega)$	$R_{\text{int}} (\Omega)$
1	77	93	25380	64	84	239
2	78	83	15830	62	96	273
5	75	97	8052	63	117	240
10	73	98	6951	70	140	547

equivalent circuit

R_{bulk} : bulk ohmic resistance

R_{gb} : grain boundary resistance of SE

R_{sl} : charge-transfer resistance of solid–liquid interface

R_{ss} : interfacial resistance of solid–solid interface (SE|cathode, SE|anode)

R_{int} is the sum of all interfacial resistances including the solid–liquid interface (R_{sl}) and solid–solid interface (R_{ss}).

3.3.2 Electrochemical Impedance Spectroscopy of Solid-State Li₂S Cells

The origin of the improved cell cyclability with the solvate interlayer incorporation was investigated using electrochemical impedance spectroscopy (EIS). **Figure 3.10a–b** shows the Nyquist plot obtained from the bare and interlayer-modified cell measured prior to galvanostatic cycling. The impedance spectra of the same cell were monitored after each charge and discharge cycle and are shown in **Figure 3.10c–f**. The magnified view of the high frequency region (low Z') is shown in **Figure 3.11**. The Nyquist plot can be fit with equivalent circuits for quantitative comparison of the resistance elements. The equivalent circuit previously utilized for solid-state battery systems was employed in our study, as presented in **Figure 3.10c**.^{43–45} A constant phase element (CPE) was used in place of a capacitor to model the non-ideal behavior of the electrode (e.g. roughness of particles). R_{bulk} is the bulk ohmic resistance including ionic resistance of both SE and electrodes. R_{gb} is the grain boundary resistance inherently existing in the SE. R_{ss} corresponds to the interfacial resistance of *solid–solid interfaces* including both SE|cathode and SE|anode interfaces. The cell with the solvate interlayer exhibits another semicircle in the high frequency region that must be analyzed. In this case, the circuit used in **Figure 3.10c** did not yield good fits. The inset to **Figure 3.10d** shows the equivalent circuit used to fit the interlayer-modified cell. Addition of a new circuit element invoking a new resistance (R_{sl}) and constant phase element (CPE_{sl}) yields much better correspondence to the data. R_{sl} likely originates from charge-transfer resistance at the *solid–liquid interfaces* including solvate|SE, solvate|anode, and solvate|cathode.⁴⁶ In addition, both the bare and interlayer-modified cell exhibit a tail at the low frequency region, which corresponds to the diffusion of Li^+ within the cathode.⁴⁷ This tail, however, is not well-defined in **Figure 3.10d** and therefore was not included in the fits. The tabulated values for the fits are shown in **Table 3.1–3.2**. The sum of all interfacial resistances

including solid–solid interface resistance (R_{ss}) and solid–liquid interface resistance (R_{sl}) is denoted R_{int} in the table.

We next discuss the general trend observed in solid-state Li_2S cell as it is sequentially charged and discharged. As shown in **Figure 3.10a–b**, the Nyquist plots of both as-assembled cells are dominated by straight lines and the cells exhibit relatively small resistances with or without the presence of the solvate interlayer. A mid to low frequency semicircle with $R = 346 \, \Omega$ is observed from the interlayer-modified cell which likely originates from electrode interfaces, since the Nyquist plot of the LPS|interlayer pellet measured between two blocking electrodes exhibits no such semicircle (**Figure 3.12**).

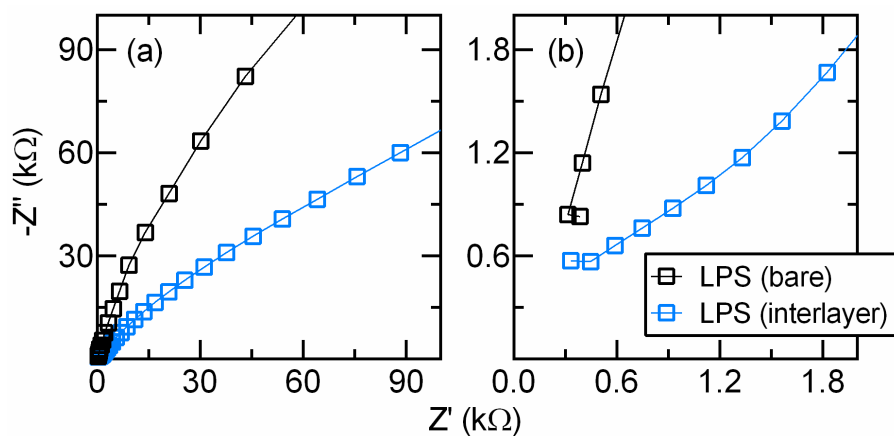


Figure 3.12 (a) Nyquist plots of LPS without and with solvate interlayer. The pellet was placed between two stainless-steel blocking electrodes. (b) shows the amplified view of the high frequency region.

After the initial charge of the solid-state Li_2S cell, the formation of a large semicircle corresponding to R_{int} is observed for both the bare and interlayer-modified cell (**Figure 3.10c–d**). The R_{int} is a combination of interfacial resistance between both SE|anode and SE|cathode but the interfacial processes at the anode and cathode are not distinguished here. Previous work suggests that the resistance from SE|anode and its change with increasing state-of-charge is negligible.^{43–44} Therefore, the dramatic increase in R_{int} can be attributed to the processes at the cathode and its interfaces. Most likely, the large interfacial resistance at the cathode originates from large volume change associated with the delithiation of Li_2S . Upon charging, the delithiation of Li_2S is accompanied by a significant volume contraction possibly causing mechanical contact loss within the composite cathode. The contact loss between active material and SE likely results in a longer Li^+ diffusion length, contributing to the increase in interfacial resistance at the cathode.

As shown in **Figure 3.10e–f** and **Table 3.1–3.2**, after discharging the large semicircle observed in the charged cell disappears and the cell impedance decreases back to the value similar to that of as-assembled cell. Similar trends are observed for both the bare and interlayer-modified cells. When S_8 reduces back to Li_2S , volume expansion occurs likely re-establishing the local contact between active material and SE. The dramatic decrease in cell resistance upon discharge is likely a consequence of decreased interfacial resistance at the cathode. It is worth noting that the magnitude of the impedance change upon charging and discharging is greater in Li_2S -based solid-state cells, compared to what is observed in solid-state batteries using LiCoO_2 ⁴³ or $\text{LiNi}_{0.8}\text{Co}_{0.1}\text{Mn}_{0.1}\text{O}_2$ ⁴⁸. This is likely due to the larger volume change of Li_2S (79%) upon delithiation compared to layered oxide materials (2 – 5%).

For the bare solid-state Li_2S cell without the solvate interlayer, the impedance change upon each charge and discharge cycle is almost reversible as the battery cycling proceeds. For

example, the radius of the semicircle shown in **Figure 3.10c** is relatively constant after each charge cycle of 1, 2, 5, and 10 and it decreases back to its original impedance value after discharge cycle. In contrast, the interlayer-modified solid-state cell exhibits a very different trend where the cell impedance after charging gradually decreases as cycle number increases from 1, 2, 5, and 10 (**Figure 3.10d**). The fit results shown in **Table 3.1** and **Table 3.2** agree well with this observation. The R_{int} of the bare cell after charge remains relatively constant as a function of cycle number, whereas R_{int} of the interlayer cell decreases significantly from 25380 Ω at 1st charge to 6951 Ω at 10th charge. This decrease in interfacial resistance may be related to the wetting of the cathode and SE layer by solvate electrolyte, where the extent of wetting is a function of cycle number.

3.3.3 Cross-Section SEM/EDS Analysis

To examine possible infiltration of solvate during battery cycling, we performed cross-section SEM/EDS analysis of the interlayer-modified pellet as shown in **Figure 3.13**. **Figure 3.13a** shows a cross-section SEM image of the as-assembled solid-state Li_2S pellet with the solvate interlayer measured without electrochemical cycling and **Figure 3.13d** shows the cross-sectional SEM of the interlayer-modified Li_2S pellet measured after 10 cycles. In order to monitor possible permeation of the solvate with time, the as-assembled cell was allowed to rest for 7 days without cycling prior to measurement. **Figure 3.13a** shows a cross-section featuring both the cathode layer (top) and the SE layer (bottom). Interestingly, the morphology of the cathode layer is similar to that of the SE layer in the as-assembled pellet. In contrast, after 10 cycles the morphology of the cathode layer is very different from what is seen in the SE layer (**Figure 3.13d**). The cathode layer is more densely packed than the SE layer and no obvious

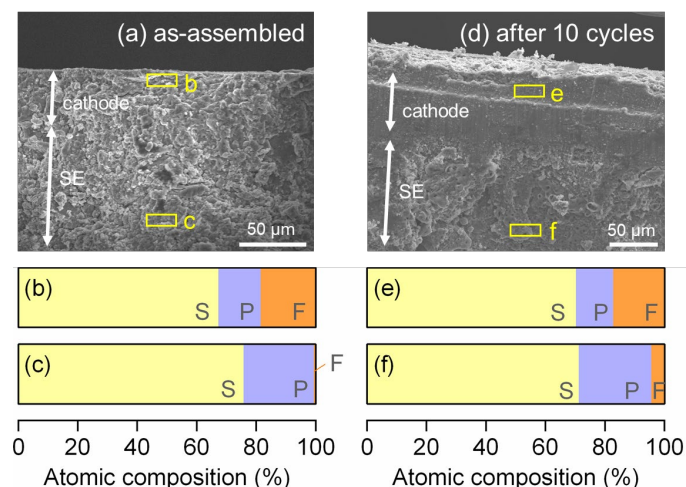


Figure 3.13 Cross-section SEM images of (a) as-assembled Li_2S pellet with the solvate interlayer and (d) the interlayer-modified Li_2S pellet after 10 cycles. The composite cathode is $\text{Li}_2\text{S}/\text{C}/\text{SE}$ (1:1:2 wt%). Yellow rectangle regions shown in (a) and (d) are used for EDS analysis and corresponding results are shown in (b–c) and (e–f). Regions (b) and (e) are closer to the surface of the cathode and regions (c) and (f) lie within the SE layer. The tabulated values for atomic compositions are shown in **Table 3.3**. The possible infiltration of the solvate across the pellet is confirmed by comparing relative F content (F atoms from LiTFSI and TTE) at different regions.

Table 3.3 Cross-section EDS compositional analysis of the as-assembled cell (regions b–c) and the cycled cell (regions e–f) shown in **Figure 3.13**.

region b (cathode)	with interlayer, as-assembled		region e (cathode)	with interlayer, cycled	
	atomic %	F/P ratio		atomic %	F/P ratio
S	67.1	-	S	70.1	-
P	14.3	1.30	P	12.5	1.39
F	18.6		F	17.4	
region c (SE)	atomic %	F/P ratio	region f (SE)	atomic %	F/P ratio
	atomic %	F/P ratio		atomic %	F/P ratio
S	75.7	-	S	71.1	-
P	23.6	0.03	P	24.4	0.18
F	0.7		F	4.5	

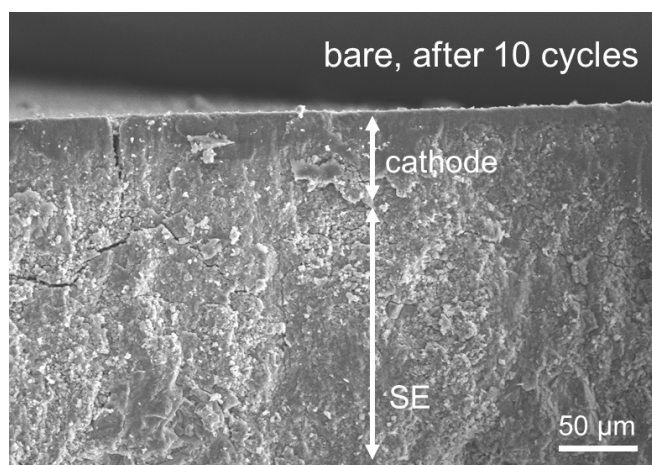


Figure 3.14 Cross-section SEM image of the bare solid-state Li_2S cell after 10 cycles. The composite cathode is $\text{Li}_2\text{S}/\text{C}/\text{SE}$ (1:1:2 wt%). After cycling the bare cell, no obvious morphological change is observed in the cathode layer.

pores are observed within it. This densified cathode layer after cycling in the presence of the solvate interlayer suggests that the use of solvate improves the wetting of the cathode by filling pores and void spaces within the cathode. The infiltration of solvate is likely achieved by cycling of the battery, since the cathode layer morphology of the as-assembled cell didn't show significant change. Additionally, the formation of dense cathode layer is not observed after cycling the bare solid-state cell (**Figure 3.14**). Therefore, the permeation of solvate is only achieved with battery cycling.

In addition to the increased wetting of the cathode, solvate can also penetrate across the SE, permeating into grain boundaries of SE. To examine this phenomena, EDS compositional analysis was performed on two different areas and is shown in **Figure 3.13b–c** for the as-assembled cell and **Figure 3.13e–f** for the cycled cell. Two different regions demarcated by yellow rectangles are analyzed where regions b, e are close to the cathode surface and regions c, f lie within the SE layer. The tabulated values for atomic compositions obtained from EDS are shown in **Table 3.3**. EDS results show the presence of substantial amount of S and P along with a small amount of F within the pellet. C, N, and O atoms are also detected by EDS but not here shown for clarity. To determine whether solvate permeates into the SE and to what extent, we monitor the concentration of F (F atoms from solvate; LiTFSI and TTE) relative to P (P atoms from LPS) across the pellet. The S concentration appears less diagnostic for solvate penetration, since S signal arises from LPS, Li_2S , and LiTFSI. For the as-assembled cell, the F/P atomic ratio is 1.30 in the cathode layer (region b) and 0.03 in the SE layer (region c), corresponding to the decreased F content in the SE (43-fold lower). The relative F content in the SE layer is significantly lower than what is detected in the cathode layer, indicating that the permeation of the solvate across the pellet is somewhat limited in the as-assembled cell. The cycled cell also

shows smaller F/P ratio within the SE layer (region f) than the cathode layer (region e), but the decrease is only 8-fold. This suggests that permeation of the solvate across the pellet is increased with battery cycling, even though full permeation of the solvate is not achieved. The infiltration of solvate into SE layer could be driven electrochemically by the movement of Li^+ ions. The exact Li^+ ion transport mechanism could be studied by performing ^7Li NMR experiments, which is the focus of future work.

Results using a solvate interlayer suggest that solvate penetration into the SE occurs with battery cycling. This solvate penetration into the cathode and the SE layer is associated with improved battery performance. We wondered whether *premixing* the solvate and the SE to form what we are calling a ‘solvSEM’ electrolyte might yield even better results in terms of battery cyclability and cell impedance.

3.3.4 Hybrid Li_2S Cell Using the SolvSEM Electrolyte

Figure 3.15 shows the electrochemical performance of the hybrid Li_2S battery prepared using the ‘solvSEM’ electrolyte. The solvSEM is a mixture of solvate electrolyte and SE as shown in the inset to **Figure 3.15c**. Since solvSEM is malleable enough to form good interfacial contact with both cathode and anode without applying high pressure, the cell preparation obviates the pellet pressing step which is typically required to prepare solid-state cells. Instead, solvSEM was spread onto a coin cell for electrochemical measurements.

Figure 3.15a shows the charge and discharge profile of the solid–liquid hybrid cell and **Figure 3.15b** show the corresponding differential capacity plot. To facilitate the comparison of electrochemical response in various electrolytes and cell configurations studied here, the voltage

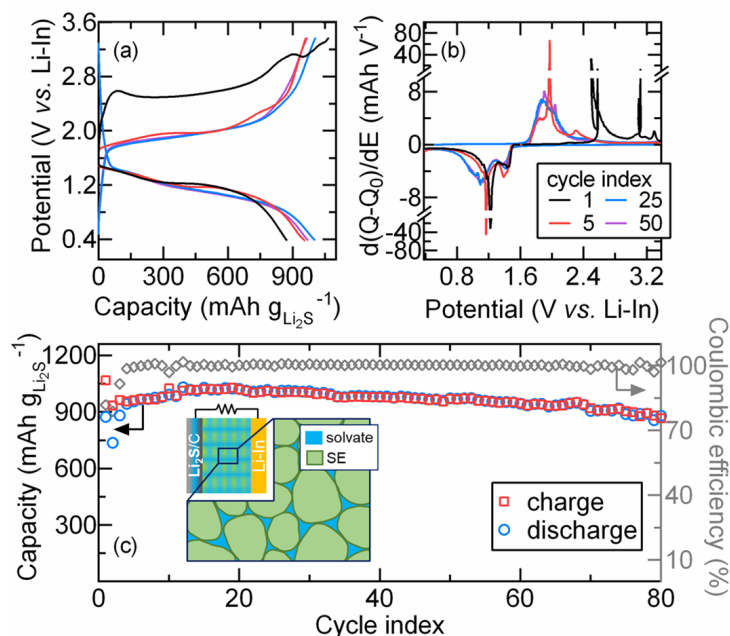


Figure 3.15 Electrochemical performance of the hybrid Li₂S batteries using the solvSEM electrolyte. The cell was prepared with Li-In alloy anode and Li₂S composite cathode (Li₂S:C = 1:1 wt%). (a) charge and discharge voltage profiles, (b) differential capacity curves, and (c) long-term cycling of the hybrid Li₂S cell. The cell was cycled between 0.38 V and 3.38 V vs. Li-In (1 V and 4 V vs. Li/Li⁺) at a current loading of C/10. Electrochemical measurement was performed at room temperature. The inset to (c) shows the schematic representation of the hybrid cell and the solvSEM electrolyte.

profile and the corresponding differential curve for each system are summarized and shown in **Figure 3.4**.

As shown in **Figure 3.15a–b**, the first charge cycle exhibits a large overpotential which disappears at higher cycle numbers. This initial large overpotential was also found in the solid-state Li_2S cell (**Figure 3.5**). The electrochemical response in the solvSEM electrolyte is closer to what is observed in the liquid electrolyte than that of the solid electrolyte (**Figure 3.4**). The Li_2S cell prepared with liquid electrolyte exhibits well-defined two plateaus at 1.5 V and 1.1 V vs. Li-In during discharge, whereas the bare solid-state cell exhibits only one plateau at around 1.2 V.

With the solvSEM electrolyte, two discharge plateaus are observed at 1.4 V and 1.2 V vs. Li-In but these plateaus are less clearly defined, displaying a mostly sloping profile relative to what is observed with the liquid electrolyte. This observation suggests that Li-S electrochemistry in the solvSEM electrolyte is a solution-mediated process involving polysulfide intermediates, but that the dissolution of polysulfides is somewhat limited. The shape of the voltage profile remains relatively stable even at higher cycle numbers. This stability is in contrast to the trend shown by the interlayer-modified solid-state cell, in which the shape of the voltage curve changed progressively as cycle number increases to exhibit a more sloping discharge curve at higher cycle numbers (**Figure 3.4** and **Figure 3.5**). Most likely, this difference between the interlayer-modified cell and the hybrid cell arises from the cell preparation method – the interlayer-added cell has to be cycled for the solvate permeation to occur whereas the solvSEM is premixed and doesn't require extensive cycling. In addition, the hybrid Li_2S cell with the solvSEM electrolyte displays smaller cell polarization between charge and discharge compared to the solid-state cell with the solvate interlayer. The origin of this smaller polarization could be

related to the reduced stress/strain at the solvSEM|cathode interface and favorable interfacial contact, which will be further discussed in more detail.

Figure 3.15c shows the cycling performance of the hybrid Li_2S cell using the solvSEM electrolyte. A slight increase in capacity is observed for the first 11 cycles reaching a discharge capacity of $1030 \text{ mAh g}_{\text{Li}_2\text{S}}^{-1}$ ($1480 \text{ mAh g}_{\text{S}_8}^{-1}$) at cycle 12, corresponding to 88% active material utilization. A slight decrease in capacity is observed upon extended cycling, but the hybrid cell still exhibited a good cyclability delivering $880 \text{ mAh g}_{\text{Li}_2\text{S}}^{-1}$ ($1264 \text{ mAh g}_{\text{S}_8}^{-1}$) at cycle 80. This excellent cycling performance is among close slightly worse than the best prior results for solid-state lithium-sulfur batteries.⁴⁹ The charge/discharge capacity and the capacity retention of the solvSEM-based Li_2S cell is superior to that of the interlayer-modified solid-state cell. It is worth noting that the $\text{Li}_2\text{S}/\text{C}$ composite (50 wt% Li_2S) was used in the hybrid cell instead of the $\text{Li}_2\text{S}/\text{C}/\text{SE}$ composite (25 wt% Li_2S), resulting in a higher active material loading in the hybrid system. In contrast, it was required to use the $\text{Li}_2\text{S}/\text{C}/\text{SE}$ composite to assemble the solid-state cells since the $\text{Li}_2\text{S}/\text{C}$ composite with no SE resulted in low active material utilization and rapid capacity fade. The solvSEM-incorporated cell exhibits superior cycling performance than the solid-state cells even at a higher Li_2S loading.

Figure 3.15c shows that the Coulombic efficiency is 100% and stable throughout the cycle, indicating that the polysulfide shuttle is suppressed despite the formation of polysulfides at the cathode. The SE component in the solvSEM could act as a blocking layer to prevent polysulfide diffusion to the anode.

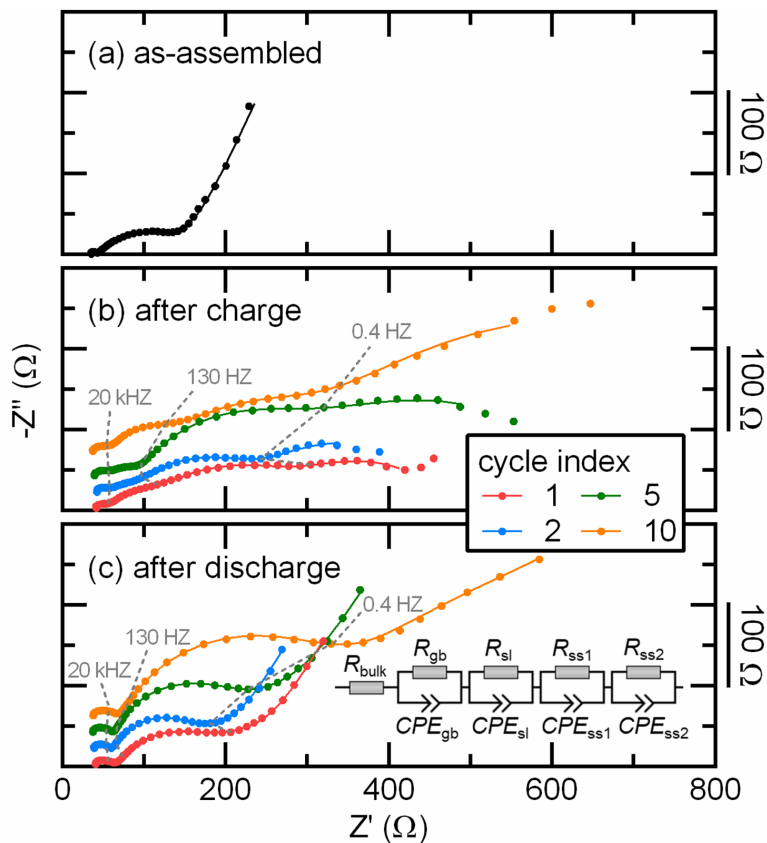


Figure 3.16 Nyquist plots of the hybrid Li_2S cell prepared using the solvSEM electrolyte, $\text{Li}_2\text{S}/\text{C}$ composite, and Li-In anode. (a) before cycling, (b) after charge cycle, and (c) after discharge cycle. Impedance spectra were collected intermittently after each charge and discharge cycle during galvanostatic cycling at C/10. Impedance spectra are stacked with an offset along the y-axis to facilitate the comparison. The inset shows equivalent circuit used to model the system. The symbols represent the data and each fit result is shown in a solid line. The resistances values for the fit can be found in **Table 3.4**.

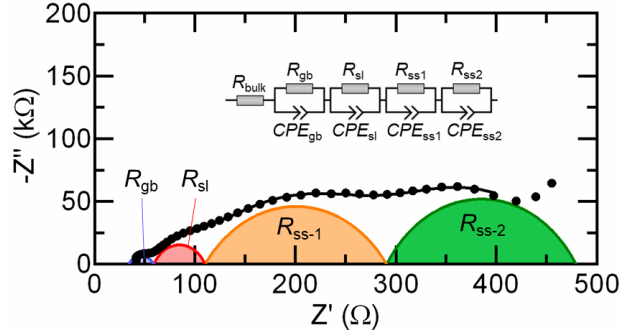


Figure 3.17 Exemplary fit of the Nyquist plot obtained from the hybrid Li₂S cell using the solvSEM electrolyte (after 1st charge). The symbols represent the data and the line indicates the fit of the data to the equivalent circuit.

Table 3.4 Resistance values obtained by fitting the Nyquist plots shown in **Figure 3.16** (Li₂S cell with the solvSEM electrolyte).

cycle #	solvSEM, after charge			solvSEM, after discharge		
	R_{bulk} (Ω)	R_{gb} (Ω)	R_{int} (Ω)	R_{bulk} (Ω)	R_{gb} (Ω)	R_{int} (Ω)
1	34	25	420	33	29	181
2	35	27	413	32	29	148
5	33	29	574	31	32	213
10	32	28	892	31	36	291

equivalent circuit						

R_{bulk} : bulk ohmic resistance

R_{gb} : grain boundary resistance of SE

R_{sl} : charge-transfer resistance of solid–liquid interface

$R_{\text{ss-1}}/R_{\text{ss-2}}$: interfacial resistance of solid–solid interface (SE|cathode, SE|anode)

R_{int} is the sum of all interfacial contributions including R_{sl} , $R_{\text{ss-1}}$, and $R_{\text{ss-2}}$.

To examine the origin of the superior battery cyclability of the hybrid Li_2S cell over solid-state Li_2S cells, we performed a series of EIS measurements on the solvSEM-incorporated hybrid Li_2S cell (**Figure 3.16**). The EIS results from the solid-state cells are shown in **Figure 3.10**. **Figure 3.16a** shows the Nyquist plot obtained from the as-assembled cell before cycling and the data shown in **Figure 3.16b–c** were measured intermittently after each charge and discharge cycle during galvanostatic cycling. The spectra were fit with an equivalent circuit model similar to that used for the interlayer-modified solid-state cell. The EIS obtained from the hybrid cell exhibits one additional semicircle relative to the interlayer-modified cell. The existence of four semicircles are clearly observed in **Figure 3.16b**. The additional semicircle is likely resolved due to the low overall cell resistance in the hybrid Li_2S cell. The four semicircles are associated with grain boundary resistance (R_{gb}), charge-transfer resistance across solid–liquid interfaces (R_{sl}), and interfacial resistance from each SE|cathode interface and SE|anode interface ($R_{\text{ss-1}}$ and $R_{\text{ss-2}}$). Exemplary fit is shown in **Figure 3.17**. The sum of all interfacial resistances involving R_{sl} , $R_{\text{ss-1}}$, and $R_{\text{ss-2}}$ is called R_{int} . The tabulated values for the fit are summarized in **Table 3.4**.

As shown in **Figure 3.16a**, the as-assembled cell exhibits a high frequency semicircle and another semicircle at mid to low frequency region, similar to what is observed in the interlayer-incorporated solid-state cell. The resistance values (R_{bulk} , R_{gb} , and R_{int}) obtained from the fitting are smaller than what is found in the interlayer-modified cell, indicating that premixing the solvate with the SE to prepare the solvSEM-based cell indeed results in smaller cell resistance. After the 1st charge cycle, the hybrid Li_2S cell exhibits higher resistance values compared to the as-assembled cell and R_{int} shows the most dramatic increase. The R_{int} increases from 131 Ω in the as-assembled to 420 Ω in the charged state, which in turn decreases back down to 181 Ω after 1st

discharge (**Figure 3.16** and **Table 3.4**). These impedance changes with cycling (i.e. increase in resistance with charge and decrease in resistance with discharge) is consistent with what is observed in the solid-state Li_2S cells as discussed in **Figure 3.10**. A slight decrease in R_{int} is observed at cycle 2, but upon subsequent cycles R_{int} gradually increases and reaches 892 Ω and 291 Ω after 10th charge and discharge, respectively.

Even though the cell resistance increases as a function of cycle number, it is worth noting that the resistance values are much smaller in the hybrid cell compared to the solid-state cell. To evaluate how the cell resistance evolves with cycling in three different systems studied in this paper, **Figure 3.18** summarizes resistance values obtained from each spectrum after charge and discharge cycles. As shown in **Figure 3.18a–d**, the R_{bulk} and R_{gb} of the cell using the solvSEM electrolyte is smaller compared to those observed in solid-state cells both with and without the solvate interlayer. The R_{bulk} and R_{gb} remains low throughout the cycle. It is reasonable to assume that the ionic conductivity of the solvSEM is higher than the bare SE, since the $(\text{MeCN})_2\text{-LiTFSI:TTE}$ solvate has slightly higher conductivity than that of LPS.^{33, 50} In addition, the grain boundary resistance is smaller in solvSEM, as solvates can flow into grain boundaries existing between LPS particles.

A more stark contrast between solid-state cells and the hybrid cell is seen in changes in interfacial resistances (**Figure 3.18e–f**). As shown in **Figure 3.18e**, after 1st charge cycle the solid-state cells exhibit very high R_{int} values, both of which are two orders of magnitude larger than that observed in hybrid cell using the solvSEM. As cycle number increases, the R_{int} of the solvate interlayer-added cell decreases due to the infiltration of solvate with cycling, reaching ca. 7000 Ω at cycle 10. With the presence of the solvate interlayer a significant decrease in interfacial resistance is achieved after 10 cycles, but the R_{int} value is still 8 times greater than that

obtained with solvSEM. The result indicates that the solvSEM forms intimate interfacial contact at electrolyte/electrode interfaces from initial cycles, thereby maintaining the favorable ionic contact even after the significant volume contraction of the cathode layer.

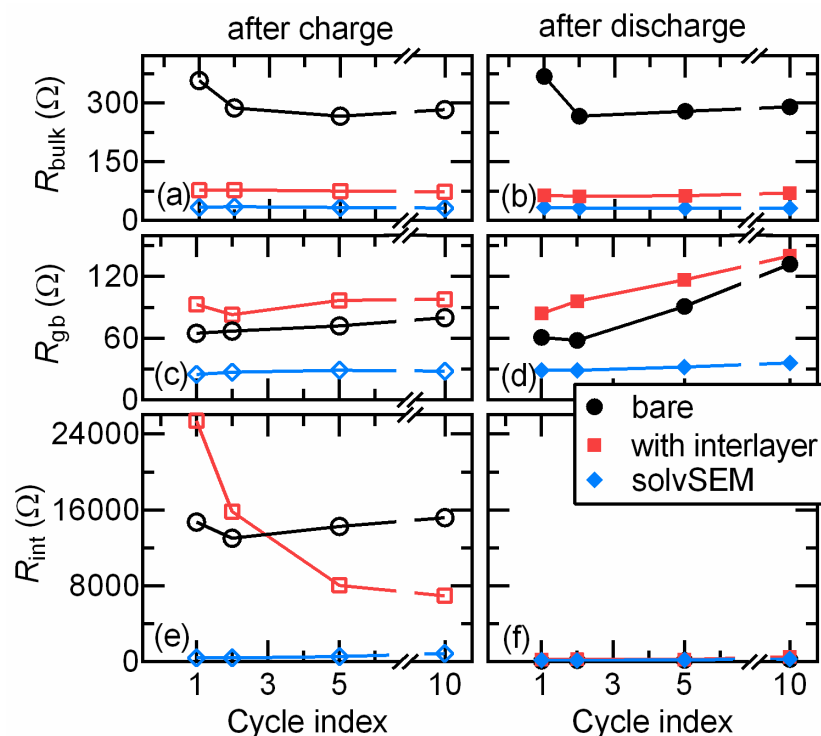


Figure 3.18 Evolution of cell resistances with cycle number in three different cell configurations (black circle: bare solid-state Li_2S cell, red square: interlayer-modified solid-state Li_2S cell, blue diamond: hybrid Li_2S cell with the solvSEM electrolyte). Resistance values were obtained by fitting the impedance spectra acquired after each charge (left panels) and discharge (right panels). The (a–b) bulk ohmic resistance, R_{bulk} , (c–d) grain boundary resistance, R_{gb} , and (e–f) interfacial resistance, R_{int} are shown.

3.3.5. Relating the Role of Solvate to Li–S Electrochemical Performance

This paper reports two different methods with which to combine solvate electrolytes with SE in Li–S batteries. In the first, the solvate was utilized as an interlayer between the electrodes and the SE. In the second, the solvate was mixed directly with the SE to yield a so-called ‘solvSEM’. Both solutions are superior to SE-alone solid-state batteries. The presence of both the solvate and the SE also is superior to liquid electrolyte alone.

We first address the beneficial effects of the solvate interlayer in the solid-state battery. There are advantages at both the positive and negative electrode sides of the battery. With respect to the anode, the solvate interlayer improves the stability of SE against Li metal, enabling long term cycling of a Li metal anode.³² In addition, the solvate itself is considerably more stable relative to low concentration electrolytes, exhibiting good compatibility with sulfide SEs.²⁶

With respect to the cathode, there are additional advantages. First, the solvate interlayer enhances the wetting of the cathode by infiltration of solvate into pores and void space within the composite cathode, establishing favorable ionic contact between SE and active material (**Figure 3.2b**). Consequently, Li^+ ion transport and charge transfer at the interface is more facile, leading to higher active material utilization. Second, even after significant volume contraction in the cathode upon delithiation of Li_2S , favorable ionic contact is maintained in the presence of solvate interlayer, which could be the origin of decreased interfacial resistance for the Li_2S cell with solvate interlayer. Additionally, the bulk resistance of the cell could also decrease as solvate infiltrates into SE and electrodes, forming more favorable Li^+ conduction pathway within the solid electrolyte and electrode materials. The penetration of solvate across the SE and the cathode is likely achieved by cycling of the battery. By using solvate as the interlayer, stress/strain at the interface could be mitigated to some degree but the formation of large crack at

the surface of the cathode and inside the SE is observed after battery cycling. In addition, the solvate permeation across the SE is achieved to some extent but full permeation of the solvate is limited.

In order to further enhance the battery cycling capability, we employed a strategy of premixing the solvate and SE to form a solvSEM electrolyte. The solvSEM electrolyte doesn't require high pressure pellet pressing to establish good interfacial contact between cell components, and thus exhibits facile processability. Due to improved wetting and interfacial contact of the cathode, higher active material loading is achieved without compromising battery cyclability. Since electrolyte/electrode interfaces are not rigid as in conventional solid-state batteries, the electrolyte layer can accommodate a volume change accompanied by the delithiation and lithiation of active material, eliminating the possibility of crack formation and resulting contact loss. Therefore, the interfacial resistance caused by the large stress/strain at the interface almost disappears, leading to high capacity and long cycle life.

The solvSEM electrolyte combines the benefits of solid electrolyte and liquid electrolyte in that solid electrolyte acts as a blocking layer for polysulfide diffusion while solvate electrolyte enhances the interfacial contact and wetting of the cathode.

3.4 Conclusion

In summary, we show that the presence of a solvate interlayer in the solid-state Li_2S cells yields lowered cell impedance and improved cyclability relative to cells that do not have this interlayer. The origin of these beneficial features is likely the improved contact between the electrolyte and the active materials, along with the ability to accommodate stress/strain from volume expansion and contraction during cycling. Additionally, direct mixing of the solvate with

the SE to make a hybrid ‘solvSEM’ electrolyte yields even better performance and cyclability. We provide a design rule to efficiently modify the electrolyte/electrode interface, while demonstrating a simple and scalable approach to achieve high-performance solid-state batteries.

3.5 References

- (1) Janek, J.; Zeier, W. G. *Nat. Energy* **2016**, 8, 426-434.
- (2) Gao, Z.; Sun, H.; Fu, L.; Ye, F.; Zhang, Y.; Luo, W.; Huang, Y. *Adv. Mater.* **2018**, 30, 1705702.
- (3) Manthiram, A.; Fu, Y.; Chung, S.-H.; Zu, C.; Su, Y.-S. *Chem. Rev.* **2014**, 114, 11751-11787.
- (4) Bruce, P. G.; Freunberger, S. A.; Hardwick, L. J.; Tarascon, J.-M. *Nat. Mater.* **2012**, 11, 19-29.
- (5) Manthiram, A.; Yu, X.; Wang, S. *Nat. Rev. Mater.* **2017**, 2, 16103.
- (6) Yin, Y.-X.; Xin, S.; Guo, Y.-G.; Wan, L.-J. *Angew. Chem. Int. Ed.* **2013**, 52, 13186-13200.
- (7) Nagao, M.; Hayashi, A.; Tatsumisago, M. *Electrochim. Acta* **2011**, 56, 6055-6059.
- (8) Nagao, M.; Hayashi, A.; Tatsumisago, M. *J. Mater. Chem.* **2012**, 22, 10015.
- (9) Kinoshita, S.; Okuda, K.; Machida, N.; Naito, M.; Sigematsu, T. *Solid State Ionics* **2014**, 256, 97-102.
- (10) Nagao, M.; Hayashi, A.; Tatsumisago, M. *Energy Technol.* **2013**, 1, 186-192.
- (11) Kobayashi, T.; Imade, Y.; Shishihara, D.; Homma, K.; Nagao, M.; Watanabe, R.; Yokoi, T.; Yamada, A.; Kanno, R.; Tatsumi, T. *J. Power Sources* **2008**, 182, 621-625.

- (12) Nagao, M.; Imade, Y.; Narisawa, H.; Kobayashi, T.; Watanabe, R.; Yokoi, T.; Tatsumi, T.; Kanno, R. *J. Power Sources* **2013**, *222*, 237-242.
- (13) Lin, Z.; Liu, Z.; Dudney, N. J.; Liang, C. *ACS Nano* **2013**, *7*, 2829-2833.
- (14) Han, F.; Yue, J.; Fan, X.; Gao, T.; Luo, C.; Ma, Z.; Suo, L.; Wang, C. *Nano Lett.* **2016**, *16*, 4521-4527.
- (15) Eom, M.; Son, S.; Park, C.; Noh, S.; Nichols, W. T.; Shin, D. *Electrochim. Acta* **2017**, *230*, 279-284.
- (16) Sun, Y.-Z.; Huang, J.-Q.; Zhao, C.-Z.; Zhang, Q. *Sci. China Chem.* **2017**, *60*, 1508-1526.
- (17) Wu, H.-L.; Huff, L. A.; Esbenshade, J. L.; Gewirth, A. A. *ACS Appl. Mater. Interfaces* **2015**, *7*, 20820-20828.
- (18) Wang, C.; Sun, Q.; Liu, Y.; Zhao, Y.; Li, X.; Lin, X.; Banis, M. N.; Li, M.; Li, W.; Adair, K. R.; Wang, D.; Liang, J.; Li, R.; Zhang, L.; Yang, R.; Lu, S.; Sun, X. *Nano Energy* **2018**, *48*, 35-43.
- (19) Asl, N. M.; Keith, J.; Lim, C.; Zhu, L.; Kim, Y. *Electrochim. Acta* **2012**, *79*, 8-16.
- (20) Zheng, B.; Zhu, J.; Wang, H.; Feng, M.; Umeshbabu, E.; Li, Y.; Wu, Q.-H.; Yang, Y. *ACS Appl. Mater. Interfaces* **2018**, *10*, 25473-25482.
- (21) Zhang, Z.; Zhang, Q.; Shi, J.; Chu, Y. S.; Yu, X.; Xu, K.; Ge, M.; Yan, H.; Li, W.; Gu, L.; Hu, Y.-S.; Li, H.; Yang, X.-Q.; Chen, L.; Huang, X. *Adv. Energy Mater.* **2017**, *7*, 1601196.
- (22) Wang, Z.; Tan, R.; Wang, H.; Yang, L.; Hu, J.; Chen, H.; Pan, F. *Adv. Mater.* **2018**, *30*, 1704436.
- (23) Choi, H.; Kim, H. W.; Ki, J.-K.; Lim, Y. J.; Kim, Y.; Ahn, J.-H. *Nano Res.* **2017**, *10*, 3092-3102.

- (24) Yamada, Y.; Yamada, A. *J. Electrochem. Soc.* **2015**, *162*, A2406-A2423.
- (25) Yamada, Y.; Furukawa, K.; Sodeyama, K.; Kikuchi, K.; Yaegashi, M.; Tateyama, Y.; Yamada, A. *J. Am. Chem. Soc.* **2014**, *136*, 5039-5046.
- (26) Oh, D. Y.; Nam, Y. J.; Park, K. H.; Jung, S. H.; Cho, S.-J.; Kim, Y. K.; Lee, Y.-G.; Lee, S.-Y.; Jung, Y. S. *Adv. Energy Mater.* **2015**, *5*, 1500865.
- (27) Cheng, L.; Curtiss, L. A.; Zavadil, K. R.; Gewirth, A. A.; Shao, Y.; Gallagher, K. G. *ACS Energy Lett.* **2016**, *1*, 503-509.
- (28) Ueno, K.; Yoshida, K.; Tsuchiya, M.; Tachikawa, N.; Dokko, K.; Watanabe, M. *J. Phys. Chem. B* **2012**, *116*, 11323-11331.
- (29) Dokko, K.; Tachikawa, N.; Yamauchi, K.; Tsuchiya, M.; Yamazaki, A.; Takashima, E.; Park, J.-W.; Ueno, K.; Seki, S.; Serizawa, N.; Watanabe, M. *J. Electrochem. Soc.* **2013**, *160*, A1304-A1310.
- (30) Suo, L.; Borodin, O.; Gao, T.; Olguin, M.; Ho, J.; Fan, X.; Luo, C.; Wang, C.; Xu, K. *Science* **2015**, *350*, 938-943.
- (31) Suo, L.; Hu, Y.-S.; Li, H.; Armand, M.; Chen, L. *Nat. Commun.* **2013**, *4*, 1481.
- (32) Philip, M. A.; Sullivan, P. T.; Zhang, R.; Wooley, G. A.; Kohn, S. A.; Gewirth, A. A. *ACS Appl. Mater. Interfaces* **2018**, *11*, 2014-2021.
- (33) Shin, M.; Wu, H.-L.; Narayanan, B.; See, K. A.; Assary, R. S.; Zhu, L.; Haasch, R. T.; Zhang, S.; Zhang, Z.; Curtiss, L. A.; Gewirth, A. A. *ACS Appl. Mater. Interfaces* **2017**, *9*, 39357-39370.
- (34) Cuisinier, M.; Cabelguen, P. E.; Adams, B. D.; Garsuch, A.; Balasubramanian, M.; Nazar, L. F. *Energy Environ. Sci.* **2014**, *7*, 2697-2705.
- (35) Nagao, M.; Hayashi, A.; Tatsumisago, M. *Electrochemistry* **2012**, *80*, 734-736.

- (36) Wu, F.; Kim, H.; Magasinski, A.; Lee, J. T.; Lin, H.-T.; Yushin, G. *Adv. Energy Mater.* **2014**, *4*, 1400196.
- (37) Xu, R.-c.; Xia, X.-h.; Li, S.-h.; Zhang, S.-z.; Wang, X.-l.; Tu, J.-p. *J. Mater. Chem. A* **2017**, *5*, 6310-6317.
- (38) Hakari, T.; Hayashi, A.; Tatsumisago, M. *Adv. Sustainable Syst.* **2017**, *1*, 1700017.
- (39) Wu, M.; Cui, Y.; Fu, Y. *ACS Appl. Mater. Interfaces* **2015**, *7*, 21479-21486.
- (40) See, K. A.; Leskes, M.; Griffin, J. M.; Britto, S.; Matthews, P. D.; Emly, A.; Van der Ven, A.; Wright, D. S.; Morris, A. J.; Grey, C. P.; Seshadri, R. *J. Am. Chem. Soc.* **2014**, *136*, 16368-16377.
- (41) Lee, C.-W.; Pang, Q.; Ha, S.; Cheng, L.; Han, S.-D.; Zavadil, K. R.; Gallagher, K. G.; Nazar, L. F.; Balasubramanian, M. *ACS Cent. Sci.* **2017**, *3*, 605-613.
- (42) See, K. A.; Wu, H.-L.; Lau, K. C.; Shin, M.; Cheng, L.; Balasubramanian, M.; Gallagher, K. G.; Curtiss, L. A.; Gewirth, A. A. *ACS Appl. Mater. Interfaces* **2016**, *8*, 34360-34371.
- (43) Zhang, W.; Weber, D. A.; Weigand, H.; Arlt, T.; Manke, I.; Schröder, D.; Koerver, R.; Leichtweiss, T.; Hartmann, P.; Zeier, W. G.; Janek, J. *ACS Appl. Mater. Interfaces* **2017**, *9*, 17835-17845.
- (44) Oh, G.; Hirayama, M.; Kwon, O.; Suzuki, K.; Kanno, R. *Chem. Mater.* **2016**, *28*, 2634-2640.
- (45) Yao, X.; Huang, N.; Han, F.; Zhang, Q.; Wan, H.; Mwizerwa, J. P.; Wang, C.; Xu, X. *Adv. Energy Mater.* **2017**, *7*, 1602923.
- (46) Busche, M. R.; Drossel, T.; Leichtweiss, T.; Weber, D. A.; Falk, M.; Schneider, M.; Reich, M.-L.; Sommer, H.; Adelhelm, P.; Janek, J. *Nat. Chem.* **2016**, *8*, 426-434.

- (47) Deng, Z.; Zhang, Z.; Lai, Y.; Liu, J.; Li, J.; Liu, Y. *J. Electrochem. Soc.* **2013**, *160*, A553-A558.
- (48) Koerver, R.; Aygün, I.; Leichtweiß, T.; Dietrich, C.; Zhang, W.; Binder, J. O.; Hartmann, P.; Zeier, W. G.; Janek, J. *Chem. Mater.* **2017**, *29*, 5574-5582.
- (49) Umeshbabu, E.; Zheng, B.; Yang, Y. *Electrochem. Energ. Rev.* **2019**, *2*, 199-230.
- (50) Sang, L.; Bassett, K. L.; Castro, F. C.; Young, M. J.; Chen, L.; Haasch, R. T.; Elam, J. W.; Dravid, V. P.; Nuzzo, R. G.; Gewirth, A. A. *Chem. Mater.* **2018**, *30*, 8747-8756.

CHAPTER 4

Investigating the Effect of Water Treatment on the Structure of Li-Ion Battery Cathode Materials

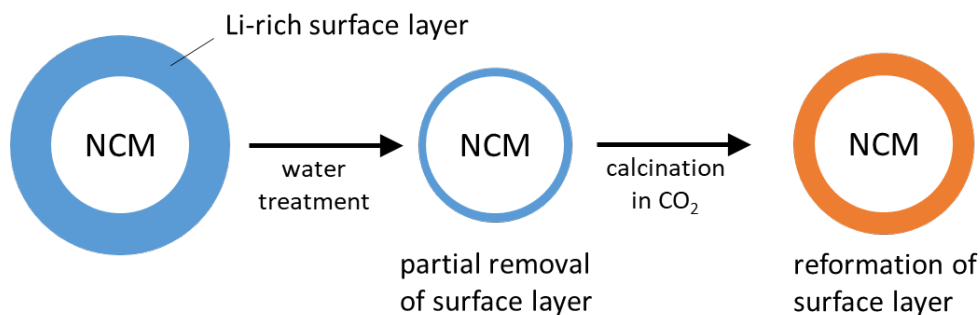


Figure 4.1 Scheme depicting the change in surface layer following water treatment and calcination process in lithium nickel cobalt manganese oxide materials.

4.1. Introduction

The development of the advanced Li-ion battery technologies is hindered by high manufacturing cost and low energy density electrode materials.¹⁻⁴ Transition metal oxide materials such as Ni-rich lithium nickel cobalt manganese oxide (NCM) are promising candidates for Li-ion battery cathodes due to their high capacity ($> 200 \text{ mAh g}^{-1}$) and low cost.²⁻⁴ Aqueous electrode processing of these NCM cathodes provides additional benefits such as lower manufacturing cost and less environmental and safety concerns compared to the traditional electrode fabrication process using N-methyl-2-pyrrolidone (NMP).⁵⁻⁶

This work was performed in collaboration with PPG Industries Automotive OEM Coatings team as part of the electrodeposition for low-cost, water-based electrode manufacturing project. The work was funded by PPG.

However, the stability of NCM materials in contact with water is adversely affected by the formation of surface species such as LiOH and Li_2CO_3 decreasing the battery cyclability.⁷ Additionally, the lithium leaching from the NCM powder with water exposure likely correlates with performance of the aqueous-based cathodes.⁸ There is increasing evidence that Ni-rich NCMs are more sensitive to atmosphere moisture during storage⁹⁻¹⁰, and therefore it is likely that the degree of Li leaching and the formation of surface species is correlated with the Ni content.

In order to understand the origin of this instability of NCM cathodes with water exposure and investigate how the change varies with Ni concentration, we systematically evaluate three different NCM powders with varying Ni content – $\text{LiNi}_{0.33}\text{Co}_{0.33}\text{Mn}_{0.33}\text{O}_2$ (NCM111), $\text{LiNi}_{0.5}\text{Co}_{0.2}\text{Mn}_{0.3}\text{O}_2$ (NCM523), and $\text{LiNi}_{0.8}\text{Co}_{0.1}\text{Mn}_{0.1}\text{O}_2$ (NCM811). The three cathode compositions are subject to Milli-Q water for varying time durations and recovered powder and resulting solution are characterized using a variety of spectroscopic techniques. The resulting solution. The solutions were analyzed using ^7Li NMR spectroscopy and inductively coupled plasma mass spectrometry (ICP-MS) to evaluate the extent of lithium and transition metal leaching following water immersion. The structural reconstruction at the cathode surface featuring a change in speciation was investigated using nuclear magnetic resonance (NMR) spectroscopy, X-ray photoelectron spectroscopy (XPS), and X-ray diffraction (XRD).

4.2 Experimental Methods

Solution ^7Li NMR: ^7Li NMR measurements were performed on a 600 MHz Varian instrument with a 5 mm autox DB probe with Z-gradient capability at the University of Illinois at Urbana–Champaign School of Chemical Sciences NMR laboratory. For lithium leaching experiments, an aliquot of NCM is placed in 5 mm NMR tube and D_2O is added at $t = 0$. An

external standard in the form of sealed, coaxial capillary containing 0.1 M LiNO₃ in acetone-d₆ was introduced. The ⁷Li resonances were further referenced to 1 M LiCl in D₂O (0 ppm). For quantitative analysis, the 90° pulse-width and T₁ relaxation delay were calibrated to allow full relaxation of the magnetization.

Solid-state ⁷Li NMR: Solid-state NMR measurements were performed at the University of Illinois at Urbana-Champaign School of Chemical Sciences (UIUC SCS) NMR Laboratory. Solid-state direct-polarization magic angle spinning (DPMAS) ⁷Li NMR measurements were performed on a 300 MHz Varian spectrometer, equipped with a 4mm Chemagnetics HX APEX probe. NMR experiments employed a 10 kHz spinning rate unless otherwise stated. The NMR spectral intensities were normalized by the sample packing amount and the number of scans to facilitate the comparison between each sample acquired under the same experimental condition. The ⁷Li spectra were referenced to 1 M LiCl in D₂O at 0 ppm.

ICP-MS Analysis: ICP-MS was carried out on a NexION 350D ICP-MS at the University of Illinois at Urbana-Champaign School of Chemical Sciences (UIUC SCS) Microanalysis Laboratory.

XPS Measurement: XPS was performed by using a Kratos AXIS Ultra spectrometer equipped with an Al K α (1486.6 eV) X-ray source. All binding energies were referenced to the C 1s peak at 284.8 eV. The XPS spectra were analyzed by subtracting the background using the Shirley method and fitting with a Voigt function (70% Gaussian-30% Lorentzian).

XRD Measurement: Powder XRD was performed on a Siemens/Bruker D-5000 equipped with Cu K α radiation. The Rietveld refinement was performed using Jade 9.0 software.

4.3 Results and Discussion

4.3.1 Solution ^7Li NMR

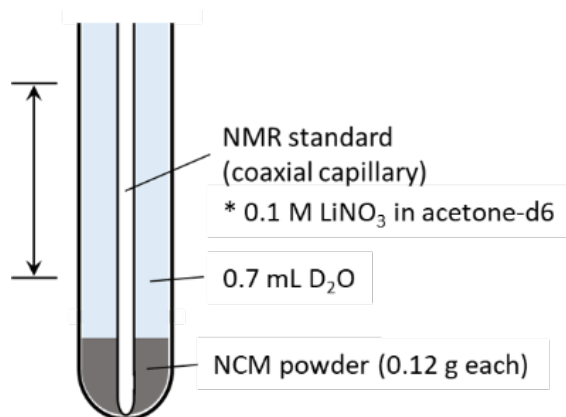


Figure 4.2 Schematic of the solution NMR setup designed for Li dissolution study.

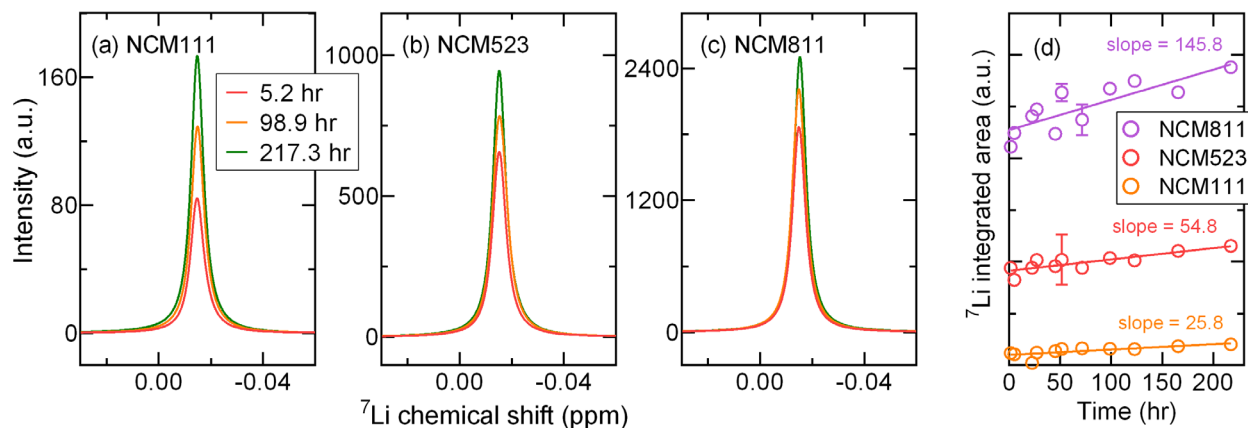


Figure 4.3 ^7Li NMR of the D_2O solution exposed to (a) NCM111, (b) NCM523, (c) NCM811 for the amount of time indicated. D_2O was added to each NCM powder at $t = 0$ and a series of ^7Li NMR measurements were performed. Water exposure time was varied from 5.2 hr to 217.3 hr. (d) ^7Li integrated area of each solution plotted as a function of time.

In order to evaluate the degree of Li leaching following immersion, we used ^7Li solution NMR to interrogate supernatant solutions following different times of immersion. We speculated that Li-rich surface layers might leach into solution after water exposure in which case the dissolved Li species will be manifested in ^7Li NMR measurements. In order to confirm the dissolution of Li-rich surface layers formed on NCM materials, NCMs of varying compositions are exposed to water for different lengths of time and the resulting solution was analyzed with ^7Li solution NMR (D_2O was used instead of H_2O for the sake of solution NMR measurements). **Figure 4.2** shows a schematic of the leaching experiment. An aliquot of NCM is placed in a NMR tube and D_2O is added at $t = 0$. An external standard in the form of sealed, coaxial capillary containing 0.1 M LiNO_3 in acetone- d_6 was introduced. The ^7Li resonances were referenced to 1 M LiCl in D_2O . **Figure 4.3a–c** shows the ^7Li NMR spectra of the resulting D_2O solution which was exposed to NCM111, NCM523, and NCM811 respectively for certain time durations. The water exposure time to NCMs was varied to monitor the dissolution trend as time increases. **Figure 4.3d** shows the ^7Li integrated area of the observed ^7Li resonance plotted as a function of time.

As shown in **Figure 4.3**, after 5.2 hr of water exposure to NCMs, one ^7Li peak is observed at $\delta = -0.015$ ppm for all three NCMs tested here. This ^7Li resonance corresponds to the Li^+ cation solvated by water molecules having small interaction with the counter anions such as OH^- and CO_3^{2-} . The exact assignment of this peak is challenging since the ^7Li chemical shift depends not only on the type of Li salt but also on the Li salt concentration (**Figure 4.4**). The observed chemical shift of the ^7Li peak is same for all three NCMs indicating that the solution species following dissolution are the same. In particular, water-soluble Li species such as LiOH , LiHCO_3 , and Li_2CO_3 dissolve into solution following water treatment. In turn, this observation

could suggest that the surface layer formed on the NCM oxides are similar regardless of Ni/Co/Mn compositions. The integrated area of the peak, however, varied significantly depending on the type of NCM. At $t = 5.2$ hr, the integrated area of the peak is much larger in D_2O solution exposed to NCM811 followed by NCM523 and NCM111 (**Figure 4.3d**). This could suggest that the Li-rich surface structure on high Ni-NCMs is thicker relative to the lower Ni NCMs and thus more susceptible to dissolution.

As the exposure time increases, the area of the 7Li peak grows as a function of time. **Figure 4.3d** shows the rate of increase in the 7Li peak area is more significant in Ni-rich NCMs. Linear regression was performed to estimate the relative rate of change for each NCM and the slope is in the order of NCM811 > NCM523 > NCM111.

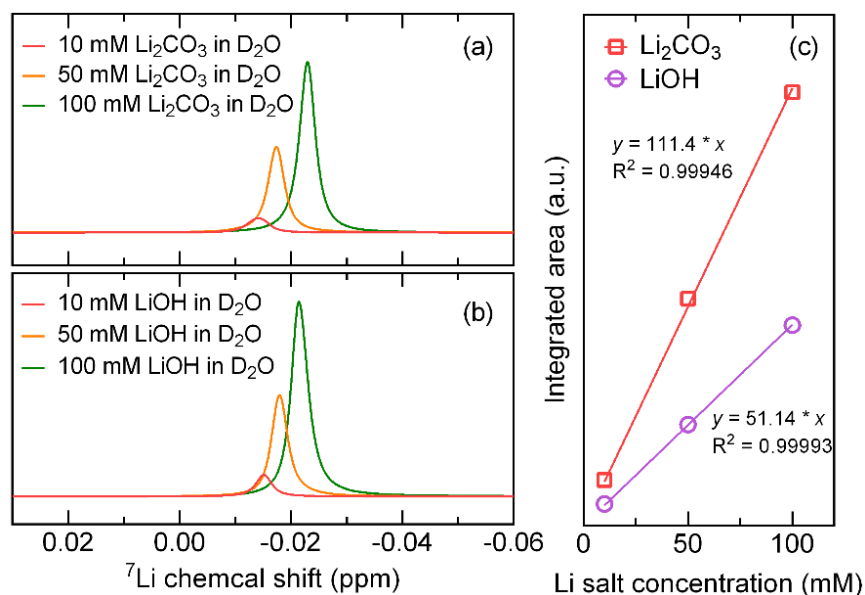


Figure 4.4 Concentration dependent 7Li chemical shift of (a) Li_2CO_3 and (b) $LiOH$ in D_2O solutions. (c) 7Li integrated area of the data shown in (a) and (b) plotted as a function of Li salt concentration.

4.3.2 ICP-MS Analysis

To further evaluate changes in NCM samples following water immersion we performed additional ICP-MS measurements on the supernatant solution. **Figure 4.5a** shows the Li concentration change in water following NCM exposure ~400 hr. The initial Li content is largest in NCM811 and after ~400 hr the Li concentration increases for all NCMs tested, where the rate of concentration change is most significant in NCM811. The Li dissolution trend shown in **Figure 4.5a** result agrees well with the ^7Li NMR data reported above. Concentrations of transition metal elements were also measured to evaluate possible leaching of Ni, Co, and Mn in the presence of water. Ni was not detected for all samples, possibly due to the detection limit of the instrument. Very small concentrations of Co and Mn were detected for all samples measured, but the quantity of material in solution was some four orders of magnitude smaller relative to the amount of Li. Consequently, metal dissolution is not correlated with Li dissolution. **Figure 4.5b** and **3c** show no trend in solution metal concentration as a function of time, again showing that Li and metal dissolution are not correlated. Therefore, it is likely that water treatment has minimal effect on transition metal leaching in NCM cathodes.

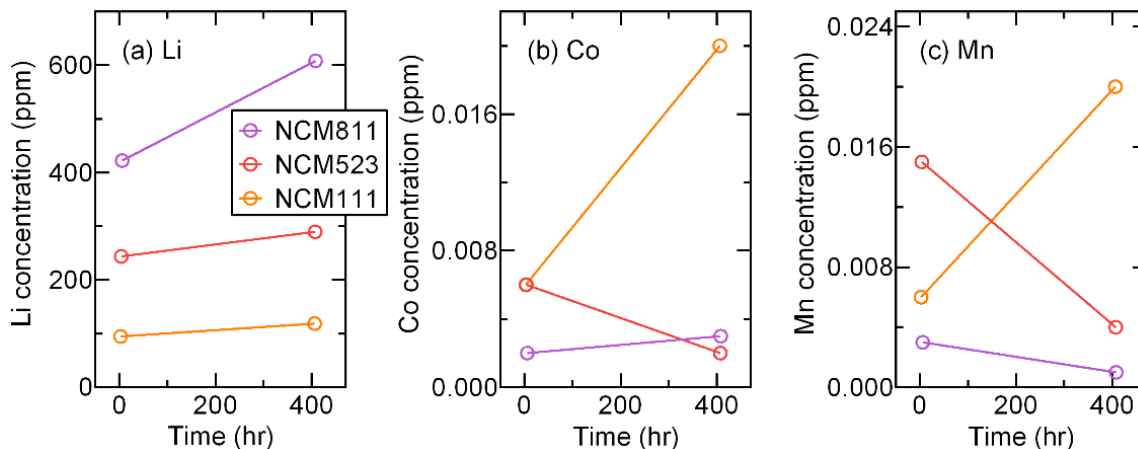


Figure 4.5 ICP-MS measurement of the D_2O solution exposed to NCM111, NCM523, and NCM811. (a) Li, (b) Co, and (c) Mn. Ni was not detected for all samples measured.

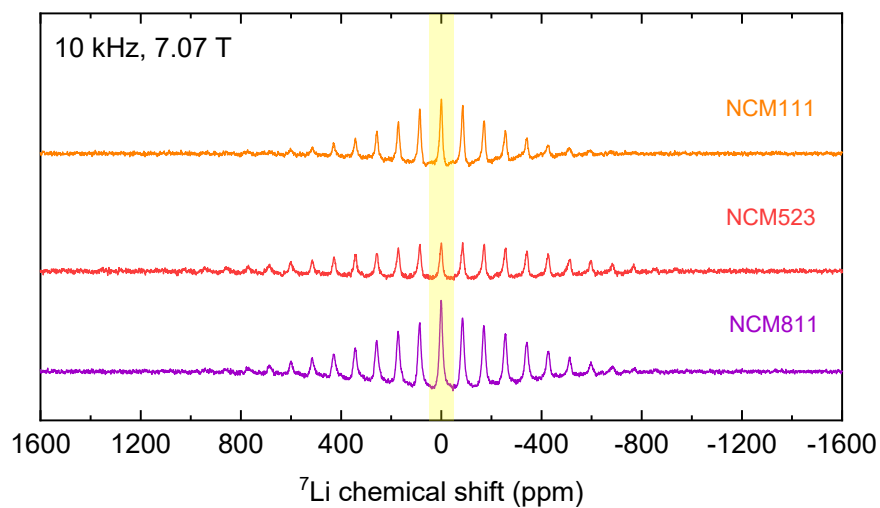


Figure 4.6 Solid-state MAS ^7Li NMR spectra of pristine NCM materials recorded at a magnetic field of 7.07 T with 10 kHz spinning speed.

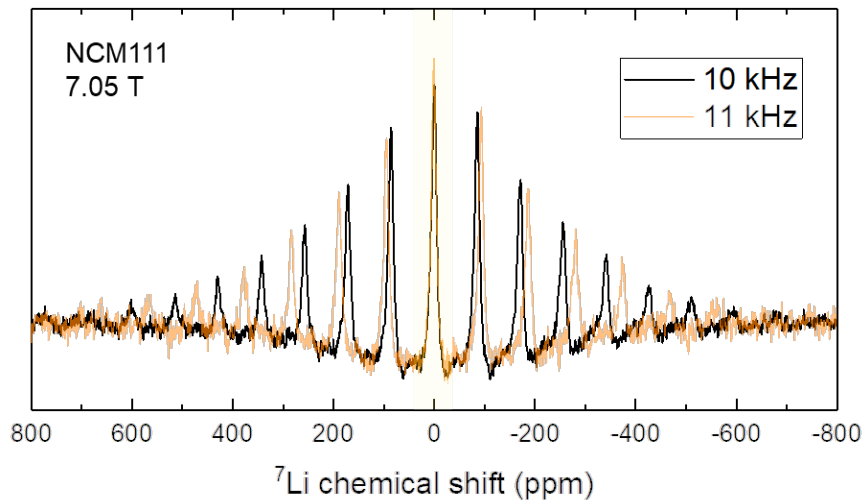


Figure 4.7 ^7Li solid-state MAS NMR spectrum of NCM111. Two different spinning speed (10 kHz and 11 kHz) was used to confirm the isotropic chemical shift.

4.3.3 Solid-State Magic Angle Spinning (MAS) ^7Li NMR

The above solution NMR and ICP-MS result show that significant Li leaching occurs upon water treatment. Solid-state magic angle spinning (MAS) ^7Li NMR experiments were performed to directly probe the local environment of Li in NCM materials. Three types of possible Li environments in NCM materials include: 1) Li in diamagnetic environment such as impurities from Li salt (0 ppm), 2) Li in Li layers (100 – 1100 ppm), 3) Li in transition metal layers (1100 – 1500 ppm).¹¹⁻¹² Li in Li layers give rise to a broad peak centered at ~500 ppm, which is a sum of different bonding environment of Li depending on the combination of transition metals in the Li^+ coordination sphere.¹¹⁻¹²

Figure 4.6 shows the solid-state MAS ^7Li NMR spectra of pristine NCM materials. The spectrum shows a strong ^7Li resonance centered at 0 ppm (yellow shaded region) which is typically associated with Li ions in a diamagnetic environment. Two different spinning speeds were used to confirm the presence of spinning side bands and that the ^7Li resonance at 0 ppm is the isotropic chemical shift (**Figure 4.7**). This peak at 0 ppm arises from Li salt impurities present on NCM oxides. The ^7Li spectra of NCM materials are dominated by this strong central resonance at 0 ppm, and the expected broad Li resonance originating from Li ions in Li layers is not observed. This absence is possibly due to the presence of strong side bands arising at relatively low spinning speed (10 kHz was used in this experiment). In addition, ^7Li is a quadrupolar nuclei in which the peak width of the resonance highly depends on the symmetry of the local environment. The local environment of Li ions in crystal lattice NCM is highly heterogeneous in nature giving rise to a very broad signal, which is not observed in the ^7Li spectra reported in **Figure 4.6**.

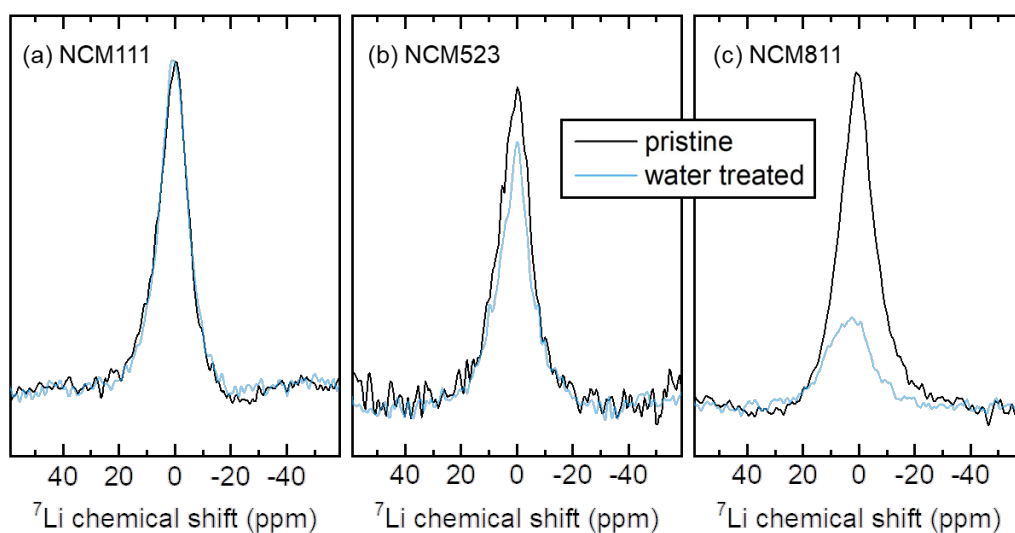


Figure 4.8 Solid-state MAS ^7Li NMR of pristine and water treated material for (a) NCM111, (b) NCM523, and (c) NCM811. Expanded region around isotropic chemical shift is shown. The spectra are normalized to the number of scans and sample packing amount for semi-quantitative analysis.

Figure 4.8 shows the MAS ^7Li NMR of pristine and water treated NCM samples. The isotropic chemical shift around 0 ppm is shown and all spectra are normalized and overlaid for comparison. The peak at 0 ppm arises from Li salt impurities such as LiOH and Li_2CO_3 on NCM oxides. As shown in **Figure 4.8a**, NMR peak intensity from NCM111 doesn't change following water treatment. More significant changes were observed in Ni-rich NCMs where NCM811 show significant decrease in peak intensity after water rinsing (**Figure 4.8b–c**). This decrease is attributed to the removal of a surface layer formed on NCM oxide surfaces with water treatment. The formation of a thicker surface film on NCM811 could lead to substantial removal of Li impurities with water treatment, leading to the signal decrease observed. This observation suggesting the presence of a thicker surface film on NCM811 is in agreement with the ^7Li solution NMR and ICP-MS data shown above.

4.3.4 XPS Analysis

In order to evaluate surface changes in NCM materials following water exposure, we performed XPS measurements on immersed samples. XPS is a surface sensitive technique that reveals chemical composition and electronic state of the surface structure. XPS analysis was performed on pristine and water treated NCMs of varying transition metal compositions. Two different sets of materials were interrogated: 1) samples from PPG and 2) samples prepared at UIUC. **Figure 4.9** shows the high resolution XPS O 1s spectra obtained from pristine NCM and water treated NCM materials (provided by PPG). The peak at 529 eV (pink) represents O^{2-} in the crystal lattice of NCM.¹³⁻¹⁴ Other higher binding energy peaks (green, orange, and blue) arise from surface impurities including LiOH, Li_2CO_3 , and LiHCO_3 .¹³⁻¹⁴ These surface layers are known to form on oxide surfaces in the presence of CO_2 and H_2O in air.¹⁴ (The pristine NCM523

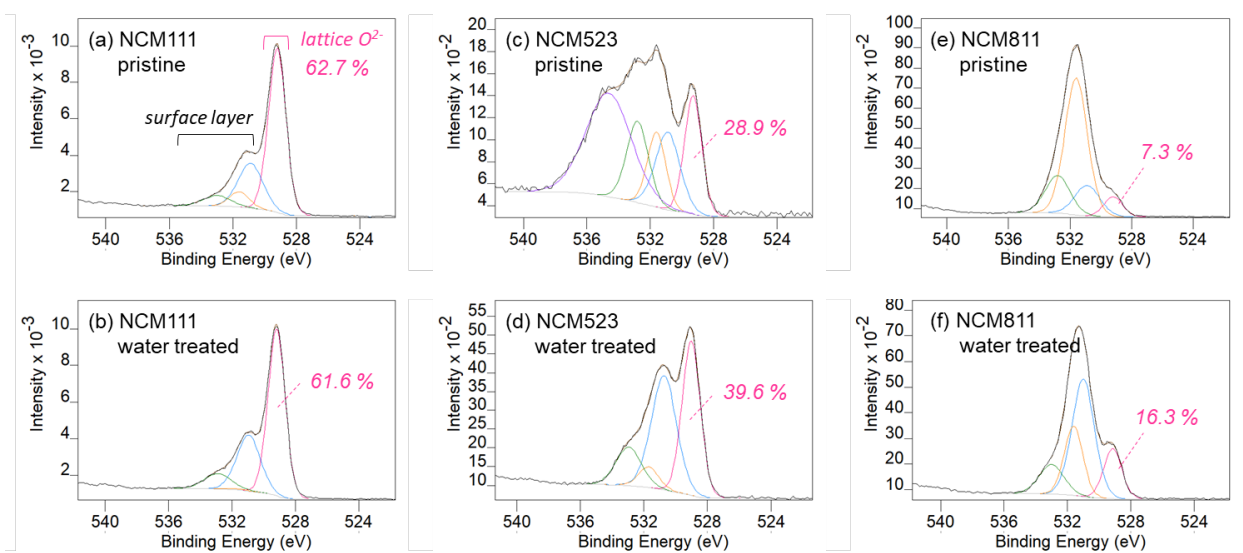


Figure 4.9 The O 1s XPS spectra of pristine NCM (first row – a,c,e) and water treated NCM (second row – b,d,f) are shown. (a–b) NCM111, (c–d) NCM523, (e–f) NCM811. The percentage area of the lattice O²⁻ peak (pink) compared to the surface layer peak (blue, orange, and green) is indicated. Both pristine and water-treated samples were provided by PPG.

material exhibits a O 1s peak at ca. 535 eV (purple) which is not found in the other two NCM materials. This peak is likely an artifact of this particular sample as other NCM523 materials did not exhibit this peak.) We note that the ratio of the intensity of the lattice O²⁻ peak to that of surface species is lower in NCM523 and NCM811 compared to that of NCM111 (**Figure 4.9a, c, e**). Considering that the analysis depth of XPS is typically ~5 nm, formation of a thick surface layer on the oxides will result in attenuation of the signal originating from lattice oxygen. Therefore, the observed decrease in the lattice O²⁻ ratio in NCM523 and NCM811 compared to NCM111 indicates the presence of a thicker surface layer in these samples. NCM811 exhibits the lowest lattice O²⁻ ratio suggesting that this high Ni-content NCM forms the thickest surface layer.

Figure 4.9a–b shows that after water treatment no significant differences are observed in pristine vs. water treated NCM111 sample. On the other hand, more pronounced changes in the O 1s spectra are observed upon water treatment for NCM523 and NCM811 materials. Water rinsing decreases the peak area of surface layer species compared to that of lattice oxygen species in both NCM523 and NCM811. This result suggests that water immersion removes the surface residues on NCM523 and NCM811, a result consistent with the leaching studies reported above. The result indicates that NCM523 and NCM811 are more sensitive to aqueous environment than NCM111 possibly due to the formation of thicker surface layer (e.g. LiOH, Li₂CO₃) that are partially soluble in water. The O 1s XPS results suggest that the surface of the NCM oxides are covered with Li-rich species such as LiOH, Li₂CO₃, and LiHCO₃, where the thickness of those layers vary depending on the compositions of Ni, Co, and Mn. Ni-rich NCMs likely form thicker surface layers on oxide surfaces. For the PPG-provided sample, we obtained high resolution Ni 2p, Co 2p, and Mn 2p spectra to gain information about the oxidation state

changes of transition metal elements with water treatment. In these samples, no obvious differences were observed in pristine vs. water treated XPS spectra of Ni 2p, Co 2p, and Mn 2p regions (**Figure 4.10 – Figure 4.12**).

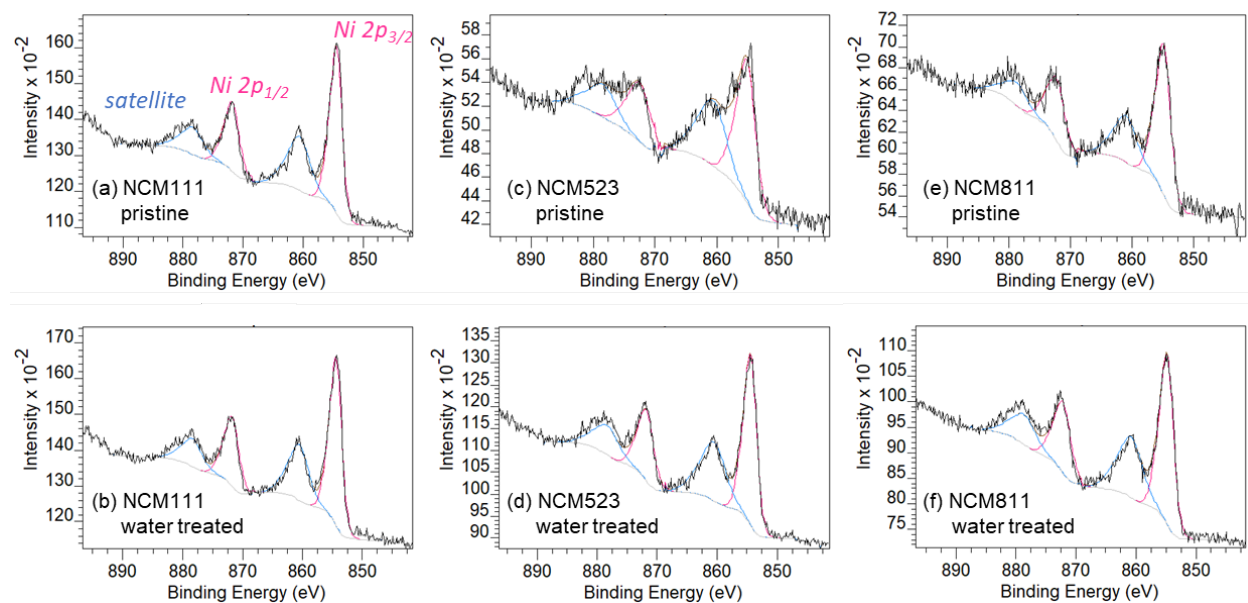


Figure 4.10 The Ni 2p XPS spectra of pristine NCM (first row – a,c,e) and water treated NCM (second row – b,d,f) are shown. (a–b) NCM111, (c–d) NCM523, (e–f) NCM811. Both pristine and water-treated samples were provided by PPG.

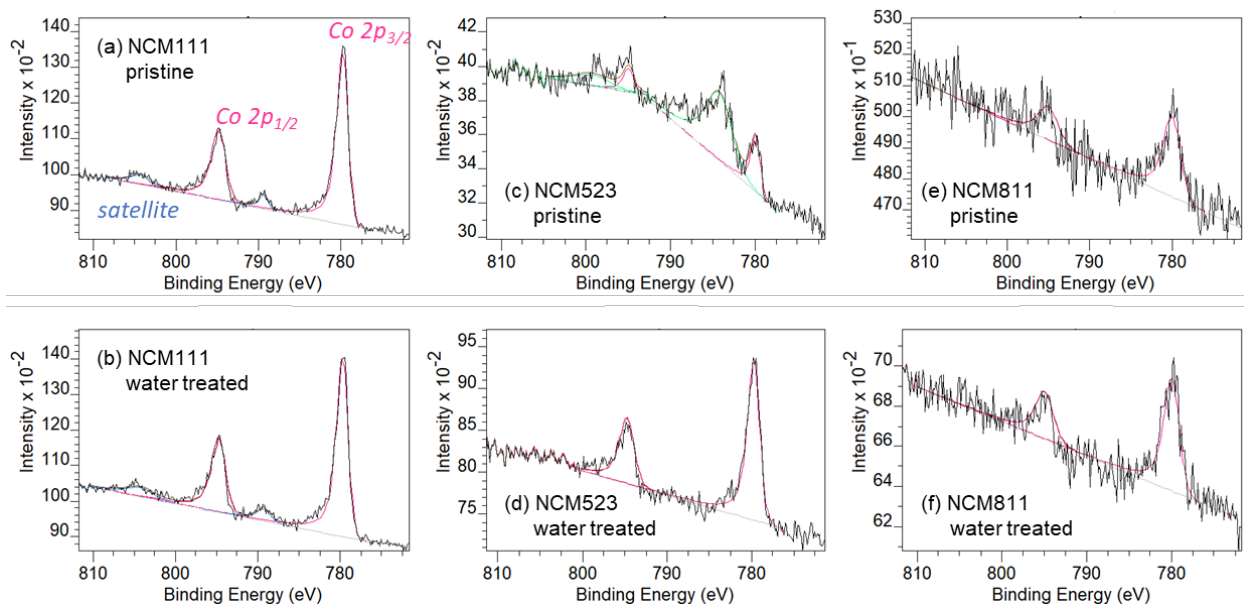


Figure 4.11 The Co 2p XPS spectra of pristine NCM (first row – a,c,e) and water treated NCM (second row – b,d,f) are shown. (a–b) NCM111, (c–d) NCM523, (e–f) NCM811. Both pristine and water-treated samples were provided by PPG.

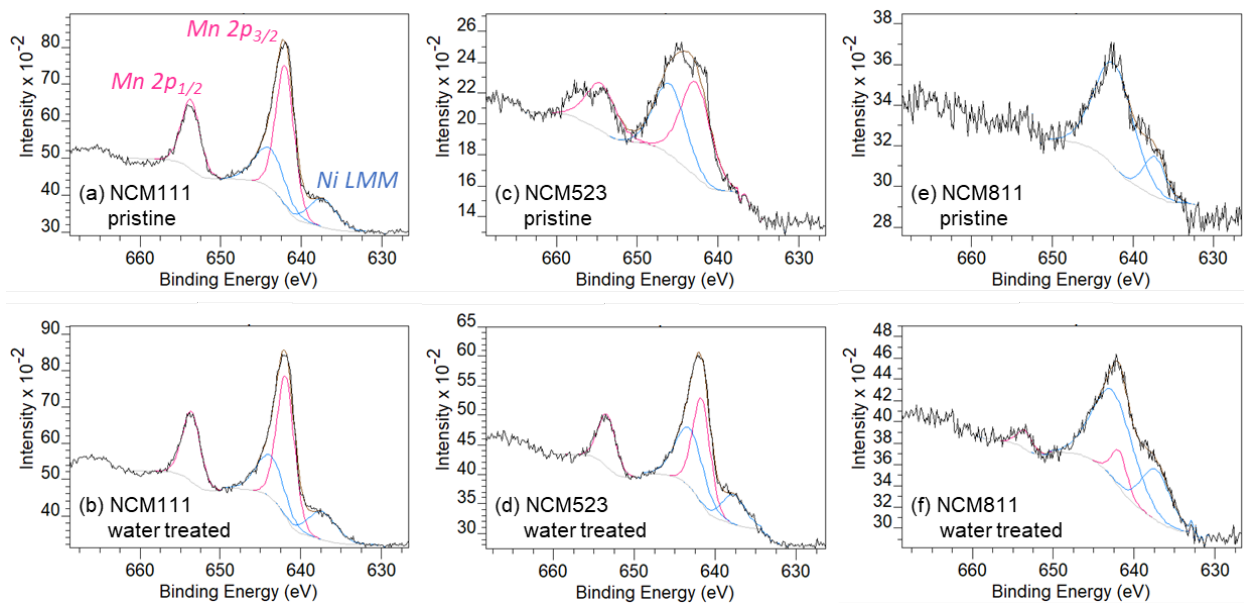


Figure 4.12 The Mn 2p XPS spectra of pristine NCM (first row – a,c,e) and water treated NCM (second row – b,d,f) are shown. (a–b) NCM111, (c–d) NCM523, (e–f) NCM811. Both pristine and water-treated samples were provided by PPG.

In order to probe possible electronic and structural changes with water exposure, we developed a protocol with which to maximize water interaction with NCM. In particular, the pristine NCM powders were ball-milled for 6 hr to decrease the particle size and increase the water contact area. Then we placed the water/NCM sample in a planetary mixer (thinky) for 20 min, repeated 3 times to avoid heating. The sample was then stirred with the solution maintained at 70 °C overnight, followed by centrifuging at 3200 rpm for 10 min. The resulting pellet was rinsed with excess water and dried under vacuum. Using this protocol, the amount of Li removed from NCM523 and NCM811 was 4.8 wt% and 16.6 wt%, respectively (Li content in the resulting solution was measured by ICP-MS).

Samples prepared using this procedure exhibited O 1s XPS similar to that reported above. XPS in the Co 2p and Mn 2p regions shows no change between the pristine and water treated samples (**Figure 4.13 – Figure 4.14**). **Figure 4.15** shows the Ni 2p region XPS for NCM523 and NCM811 as a function of water treatment. The figure shows the presence of bands associated with both Ni^{3+} and Ni^{2+} as expected for the pristine sample.¹⁵⁻¹⁶ Upon prolonged water treatment, **Figure 4.15c–d** shows that the magnitude of the Ni^{2+} signal decreases relative to the Ni^{3+} signal for NCM811. **Table 4.1** shows that the Ni^{2+} area ratio, obtained from fits to the XPS, remains mostly unchanged in NCM523 upon water exposure. This ratio, however, decreases substantially in the NCM811 material with water exposure. Because ICP-MS shows that little if any Ni is dissolved into the supernatant, the change in ratio must be associated with oxidation of the Ni centers at or near the surface of the NCM material. Substantial Li^+ leaching is associated with Ni oxidation.

One possible explanation for this behavior is cation mixing between Li^+ and Ni^{2+} .¹⁷⁻¹⁸ Previous literature proposed that Ni ions can easily occupy the lattice site of Li^+ due to their

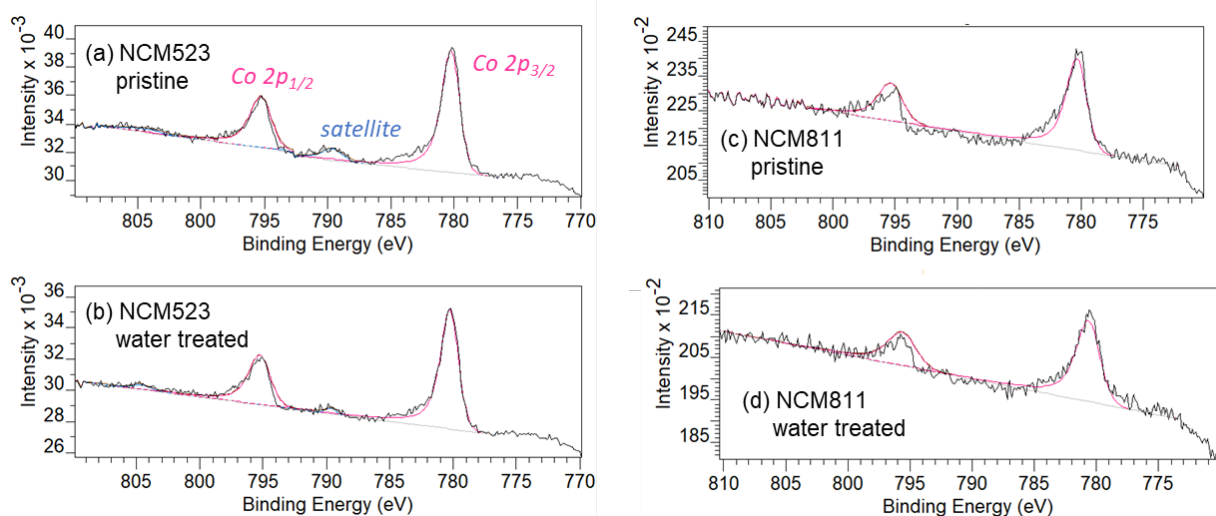


Figure 4.13 The Co 2p XPS spectra of pristine NCM (first row – a,c) and water treated NCM (second row – b,d) are shown. (a–b) NCM523, (c–d) NCM811. Water-treated samples were prepared at UIUC using the protocol described.

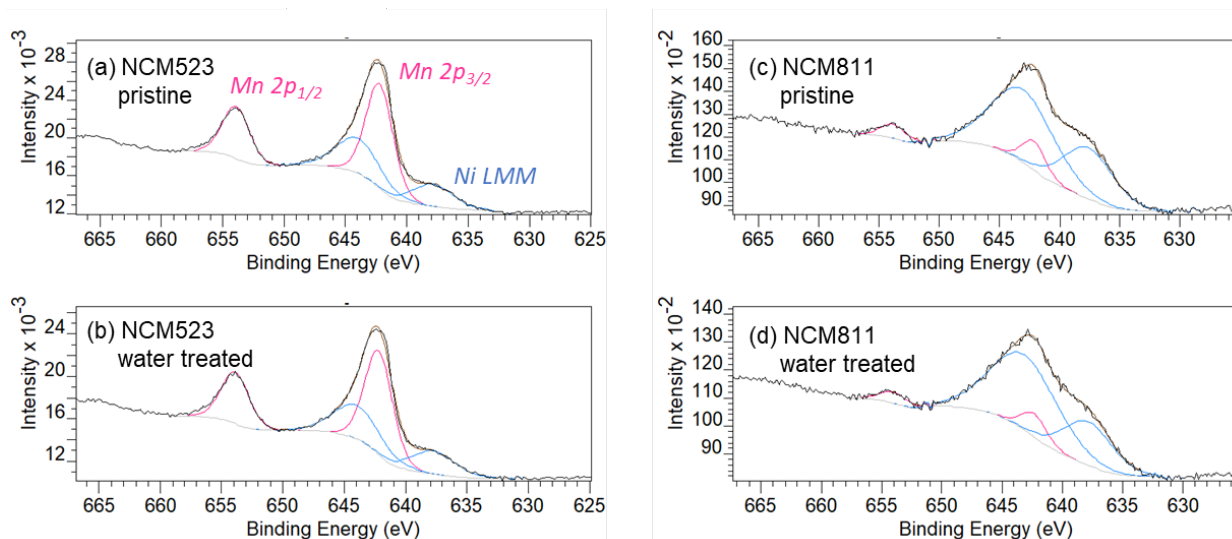


Figure 4.14 The Mn 2p XPS spectra of pristine NCM (first row – a,c) and water treated NCM (second row – b,d) are shown. (a–b) NCM523, (c–d) NCM811. Water-treated samples were prepared at UIUC using the protocol described.

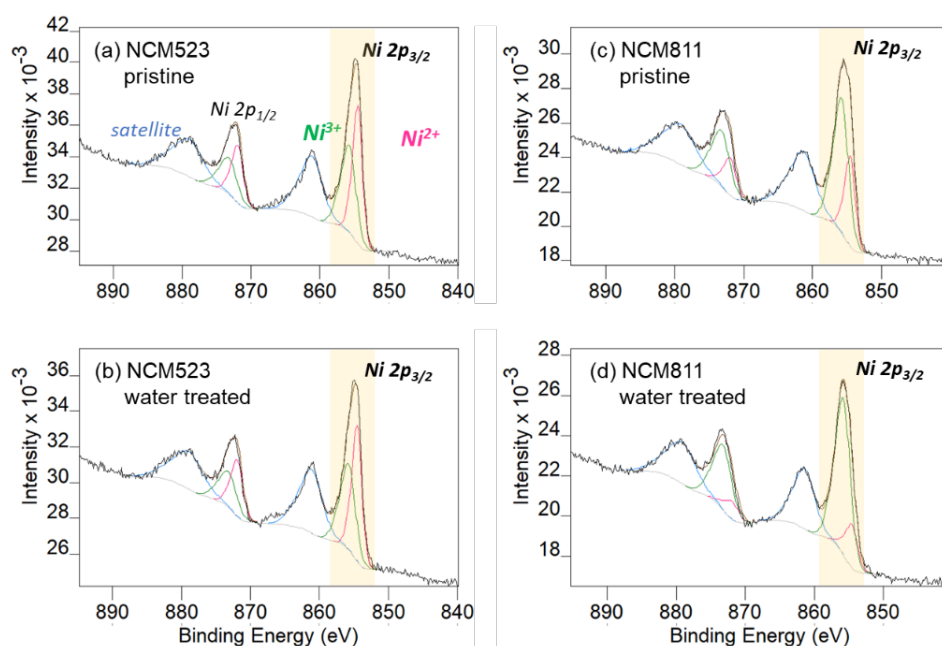


Figure 4.15 The Ni 2p XPS spectra of pristine NCM (first row – a,c) and water treated NCM (second row – b,d) are shown. (a–b) NCM523, (c–d) NCM811. Water-treated samples were prepared at UIUC using the protocol described.

Table 4.1 XPS fit result of the Ni 2p spectra shown in **Figure 4.15** and **Figure 4.18**. The Ni 2p_{3/2} region is deconvoluted.

Material	Ni ²⁺			Ni ³⁺			Ni ²⁺ ratio (%)
	B.E. (eV)	FWHM (eV)	peak area	B.E. (eV)	FWHM (eV)	peak area	
NCM523 – pristine	854.5	1.52	4851	855.8	2.30	4598	51.3
NCM523 – water treated	854.5	1.57	4314	855.8	2.32	4022	51.7
NCM811 – pristine	854.5	1.64	3133	855.8	2.35	6653	32.0
NCM811 – water treated	854.5	1.91	1503	855.8	2.40	6775	18.2
NCM811 – calcinated	854.5	2.00	5195	855.8	2.50	2928	64.0

similar ionic radius (Li^+ : 0.76 Å, Ni^{2+} : 0.69 Å), causing outward migration of Li^+ to the surface.¹⁷⁻¹⁸ The degree of cation mixing likely increases with Ni content, in which case the diffusion of Li^+ toward the surface also increases. This Li^+ can combine with H_2O and CO_2 in air to form LiOH or Li_2CO_3 , while those surface species might dissolve simultaneously in contact with water. The removal of Li^+ creates charge imbalance, which is countered by Ni oxidation. The formation and concurrent removal of Li residual layer in water results in continuous chemical delithiation of NCM oxides, evidenced by the continual increase in ^7Li peak area as a function of time.

4.3.5 XRD Analysis

^7Li NMR, XPS, and ICP-MS measurement show that water treatment has significant influence on the formation of Li impurities on NCM surfaces and further dissolution of the surface layer. The loss of significant Li, coupled with the oxidation state change in the Ni, might alter the structure of the NCM material. In order to investigate the structural changes of NCM following water treatment, XRD measurements were performed on pristine and water treated (following the protocol described above) NCM materials.

Figure 4.16 shows the XRD pattern of the pristine and water treated NCM materials. Shim *et al.* reported the development of NiO phase rock salt structure on the surface of Ni-rich NCM.¹⁹ However, the formation of any new phases was not observed for both NCM523 and NCM811, despite significant chemical delithiation after extensive water exposure as showing in the expanded regions in **Figure 4.17** (strong NiO peaks would be expected at $2\theta = 37.2$ and 43.3). After water treatment, the position of the diffraction peak remains the same in all cases but the relative intensity of the peak changes, implying changes in the lattice parameters. In order to

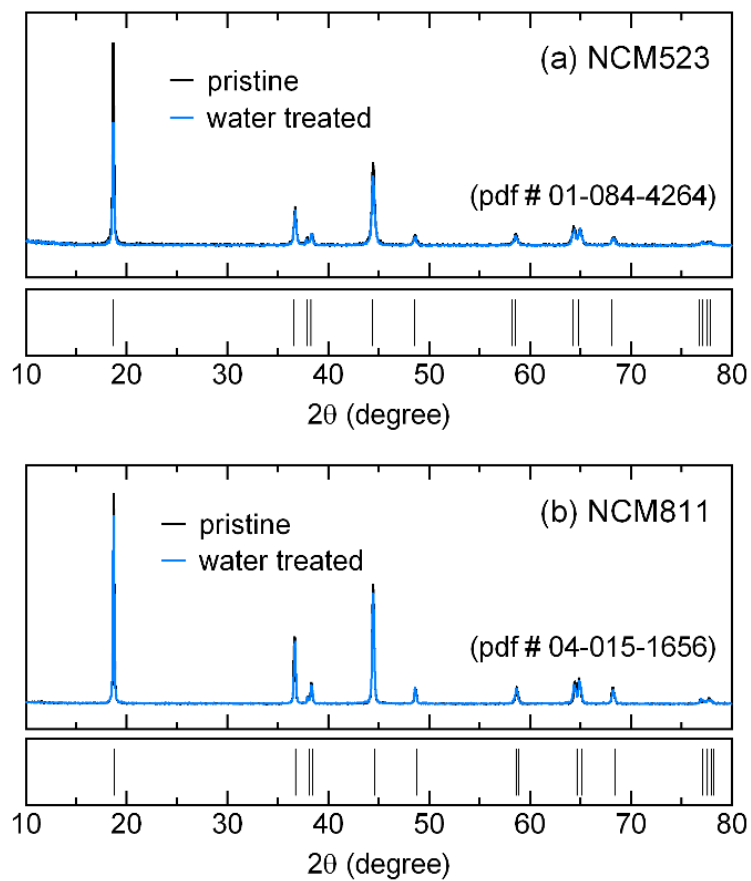


Figure 4.16 XRD pattern of the pristine and water treated NCM materials. (a) NCM523, (b) NCM811. Water treated NCM powders are recovered from solution and fully dried prior to measurements.

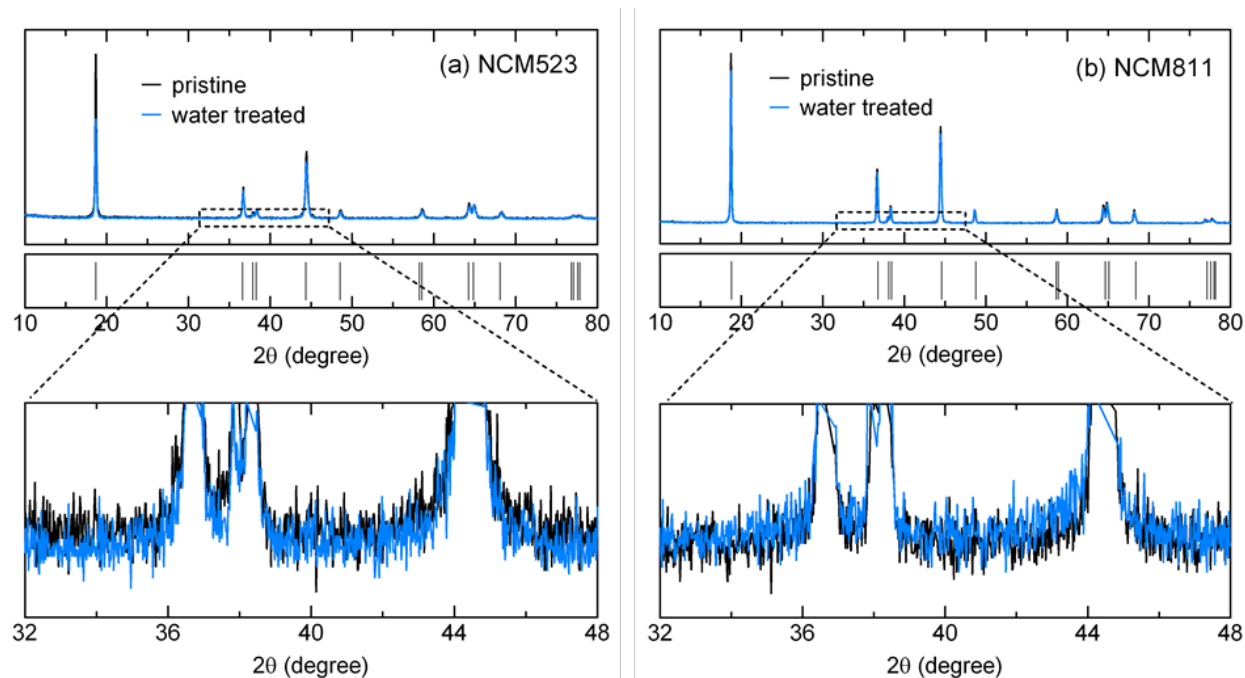


Figure 4.17 XRD pattern of the pristine and water treated NCM materials. (a) NCM523, (b) NCM811. Shown on the bottom is the expanded region between 32 and 48 degrees.

Table 4.2 Rietveld refinement result of pristine and water treated NCM materials.

Material	a (Å)	c (Å)	c/a
NCM523 – pristine	2.8696	14.2465	4.9646
NCM523 – water treated	2.8705	14.2514	4.9648
NCM811 – pristine	2.8724	14.2022	4.9443
NCM811 – water treated	2.8714	14.2262	4.9544

evaluate lattice parameter changes, we performed Rietveld refinement, as reported in **Table 4.2**. The table shows that while there is almost no change in the NCM523 following water immersion, the c/a ratio for NCM811 increases substantially following water treatment. The increased c/a ratio is consistent with a previous report where significant increase in lattice parameter c and decrease in lattice parameter a is observed upon electrochemical delithiation of NCM811.²⁰ The decrease in value a might indicate the removal of Li^+ from NCM crystal lattice and the subsequent charge compensation by the oxidation of the transition metal element (likely Ni). In addition, the increase in the c value corresponds to the increased repulsion between the transition metal – oxygen slabs.²⁰ Overall, more significant Li leaching occurs in Ni-rich NCM, leading to more pronounced structural changes.

4.3.6 Calcination Studies

Prior work showed that cathode washing is associated with a decrease in cell impedance along with decreased capacity and capacity retention.¹⁷ The results reported above show the effect of water washing on the NCM cathode is two-fold; 1) The removal of surface impurities such as LiOH and Li_2CO_3 and 2) Substantial removal of Li ions from NCM crystal lattice causing electronic and structural changes. One way to minimize substantial Li leaching following water treatment and recover the surface layer is to re-calcinate (post heat treatment in air) the NCM material.

Figure 4.18 shows high-resolution Ni 2p XPS spectra of the pristine, water treated, and calcinated NCM811 samples. NCM811 was chosen since Ni-rich NCM is more sensitive to water exposure. As discussed earlier, the relative area ratio of Ni^{2+} (pink) to Ni^{3+} (green) decreases upon water treatment. In order to confirm whether this oxidation state change is

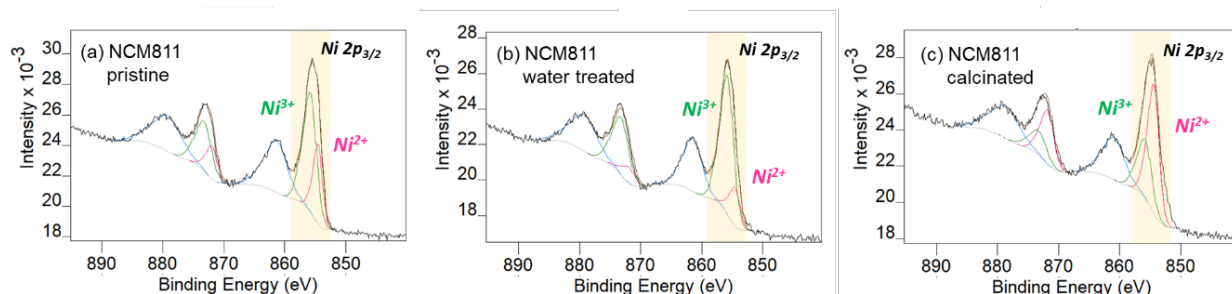


Figure 4.18 The Ni 2p XPS spectra of (a) pristine NCM811, (b) water treated NCM811, (c) calcinated NCM811 followed by water treatment. Water-treated samples were prepared at UIUC using the protocol described. Calcination was performed at 700 °C for 2 hr.

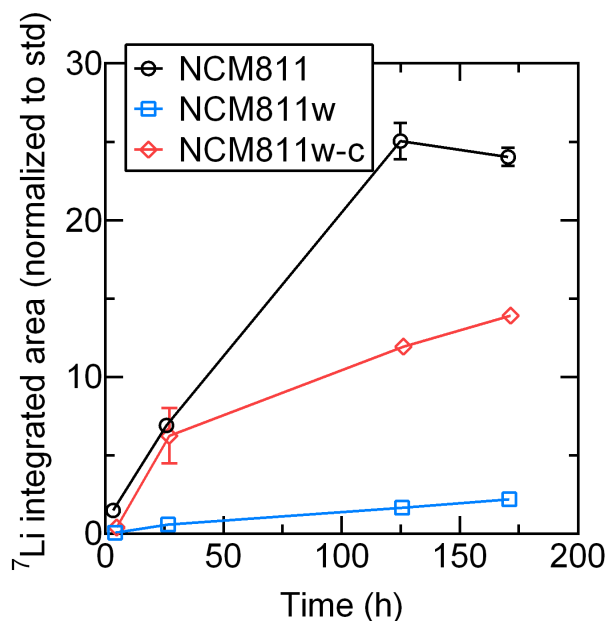


Figure 4.19 ⁷Li NMR of the D₂O solution exposed to pristine NCM811 (black), water treated NCM811 (blue), and water treated then calcinated NCM811 (red). Water exposure time was varied from 0 hr to 170 hr. ⁷Li integrated area of each solution is plotted as a function of exposure time.

reversible, we further calcinated the water treated NCM at 700 °C under air for 2 hr. **Figure 4.18c** and **Table 4.1** show that upon heat treatment the oxidation state of Ni recovers back to Ni^{2+} . The origin of the reduction of Ni^{3+} to Ni^{2+} upon heating in air is not clear, but measurements examining the effect of different calcination atmospheres (CO_2 , H_2) will be beneficial. The lithium leaching measurements using ^7Li NMR show that the calcinated sample exhibits less Li^+ leaching relative to the pristine NCM811 (**Figure 4.19**).

4.4 Conclusion

We investigated the effect of water treatment on the structure of the NCM materials with varying Ni, Co, and Mn compositions by interrogating these materials with a variety of spectroscopic techniques including NMR, XPS, and XRD. The surface structure and electronic state of elements of NCM cathode materials are characterized with XPS. Following water immersion, the Li-rich surface layers leach out into solution, as determined by ^7Li NMR and ICP-MS performed on supernatant solutions. Extensive exposure of NCM to water leads to chemical delithiation resulting in electronic and structural changes including Ni oxidation and an increase in the amount of near-surface lattice O^{2-} in NCM811 and NCM523. Calcination of the leached sample results in Ni reduction and a subsequent decrease in Li^+ leaching.

4.5 References

- (1) Nitta, N.; Wu, F.; Lee, J. T.; Yushin, G. *Mater. Today* **2015**, *18*, 252-264.
- (2) Schipper, F.; Erickson, E. M.; Erk, C.; Shin, J.-Y.; Chesneau, F. F.; Aurbach, D. J. *Electrochem. Soc.* **2016**, *164*, A6220-A6228.

- (3) Schmuch, R.; Wagner, R.; Hörpel, G.; Placke, T.; Winter, M. *Nat. Energy* **2018**, *3*, 267-278.
- (4) Myung, S.-T.; Maglia, F.; Park, K.-J.; Yoon, C. S.; Lamp, P.; Kim, S.-J.; Sun, Y.-K. *ACS Energy Lett.* **2016**, *2*, 196-223.
- (5) Li, J.; Daniel, C.; Wood, D. *J. Power Sources* **2011**, *196*, 2452-2460.
- (6) Wood, D. L.; Li, J.; Daniel, C. *J. Power Sources* **2015**, *275*, 234-242.
- (7) Zhang, X.; Jiang, W. J.; Zhu, X. P.; Mauger, A.; Qilu; Julien, C. M. *J. Power Sources* **2011**, *196*, 5102-5108.
- (8) Loeffler, N.; Kim, G.-T.; Mueller, F.; Diemant, T.; Kim, J.-K.; Behm, R. J.; Passerini, S. *ChemSusChem* **2016**, *9*, 1112-1117.
- (9) Jung, R.; Morasch, R.; Karayaylali, P.; Phillips, K.; Maglia, F.; Stinner, C.; Shao-Horn, Y.; Gasteiger, H. A. *J. Electrochem. Soc.* **2018**, *165*, A132-A141.
- (10) You, Y.; Celio, H.; Li, J.; Dolocan, A.; Manthiram, A. *Angew. Chem., Int. Ed.* **2018**, *57*, 6480-6485.
- (11) Stoyanova, R.; Ivanova, S.; Zhecheva, E.; Samoson, A.; Simova, S.; Tzvetkova, P.; Barra, A.-L. *Phys. Chem. Chem. Phys.* **2014**, *16*, 2499-2507.
- (12) Liu, H.; Bugnet, M.; Tessaro, M. Z.; Harris, K. J.; Dunham, M. J. R.; Jiang, M.; Goward, G. R.; Botton, G. A. *Phys. Chem. Chem. Phys.* **2016**, *18*, 29064-29075.
- (13) Andersson, A. M.; Abraham, D. P.; Haasch, R.; MacLaren, S.; Liu, J.; Amine, K. *J. Electrochem. Soc.* **2002**, *149*, A1358.
- (14) Shkrob, I. A.; Gilbert, J. A.; Phillips, P. J.; Klie, R.; Haasch, R. T.; Bareño, J.; Abraham, D. P. *J. Electrochem. Soc.* **2017**, *164*, A1489-A1498.
- (15) Fu, Z.; Hu, J.; Hu, W.; Yang, S.; Luo, Y. *Appl. Surf. Sci.* **2018**, *441*, 1048-1056.

- (16) Yang, J.; Xia, Y. *J. Electrochem. Soc.* **2016**, *163*, A2665-A2672.
- (17) Park, K.; Park, J.-H.; Hong, S.-G.; Choi, B.; Heo, S.; Seo, S.-W.; Min, K.; Park, J.-H. *Sci. Rep.* **2017**, *7*.
- (18) Jo, J. H.; Jo, C.-H.; Yashiro, H.; Kim, S.-J.; Myung, S.-T. *J. Power Sources* **2016**, *313*, 1-8.
- (19) Shim, J.-H.; Kim, C.-Y.; Cho, S.-W.; Missiul, A.; Kim, J.-K.; Ahn, Y. J.; Lee, S. *Electrochim. Acta* **2014**, *138*, 15-21.
- (20) Kondrakov, A. O.; Schmidt, A.; Xu, J.; Geßwein, H.; Mönig, R.; Hartmann, P.; Sommer, H.; Brezesinski, T.; Janek, J. *J. Phys. Chem. C* **2017**, *121*, 3286-3294.